The role of Ediacaran synkinematic anatectic rocks and the late-orogenic charnockitic rocks in the development of the hot Araçuaí belt

Carolina Cavalcante[1,2], Vinicius T. Meira[3], Nivea Magalhães[4], Maria Helena B. M. Hollanda[5], Eurídice Oliveira[5]

[1]Department of Geosciences, University of Tromsø – The Arctic University of Norway, Dramsveien 201, 9037 Tromsø, Norway

[2]Department of Geology, Federal University of Paraná, Av. Cel. Francisco Heráclito dos Santos, 100, Centro Politécnico, Curitiba, PR, 81531-980, Brazil

[3]Department of Geology and Natural Resources, State University of Campinas, R. Carlos Gomes, 250, Cidade Universitária, Campinas, SP, 13083-855, Brazil

[4]School of Earth and Environmental Sciences, University of St Andrews, Irvine Building, North Street, St Andrews, KY16 9AL, United Kingdom

[5]University of São Paulo, IGc, Rua do Lago 562, 05508-080 São Paulo, SP, Brazil

Abstract

The orogenic evolution of the hot Araçuaí belt is characterized by continuous magmatic activity, with magmas of different compositions recording a long-lived (~630 to ~530 Ma) tectono-thermal evolution in response to convergence between the Congo and São Francisco continents during the West Gondwana amalgamation. Geochemical data from the Carlos Chagas domain (CCD) and the Nova Venécia Complex (NVC), in the hinterland of this belt, show that these rocks contain high amounts of heat producing elements – HPEs – (Th, U, and K) and have a dominant peraluminous signature, suggesting that they result from partial melting of continental crust. The CCD is intruded by post-collisional charnockites that have a dominant shoshonitic signature, interpreted as representing magmas from an enriched mantle reservoir with a variable amount of crustal contamination. Detailed morphological investigations at the

macro- and micro-scales show that the CCD contains remnants of residuum material from metamorphic reactions associated with textures that attest to melt crystallization. This reinforces the interpretation that the CCD is locally derived, i.e., it represents an in-source subhorizontal rheologically weak layer of migmatites and parauthoctonous granites that formed during the orogenic thickening. The CCD likely triggered the formation of an orogenic plateau and a geological setting in which high temperature conditions could be sustained for tens of millions of years. In such a setting, continuous heat supply from radiogenic decay might have been the main heat source for the compositionally diverse magmatism during most of the orogenic evolution of the Araçuaí belt.

Keywords: Migmatite, hot Araçuaí belt, geochemical, radiogenic decay, Gondwana

1. Introduction

Migmatites and associated granites are widely considered as the main products of crustal differentiation, which occurs due to partial melting in the roots of orogenic belts coupled to efficient melt-migration leading to the formation of granitoid intrusive complexes (Douce and Johnston, 1991; Brown, 2001; Vanderhaeghe and Teyssier, 2001; Sawyer et al., 2011). Extracting geological information from migmatites is not straightforward, as they typically display morphological heterogeneities and complexities that can easily lead to misinterpretations (e.g., Pawley et al., 2015). Migmatitic rocks form a substantial part of many wide and mature hot orogens that have undergone pervasive partial melting, and correctly identifying and extracting information from migmatitic rocks and structures is therefore of paramount importance in such orogens (e.g., Kruckenberg et al., 2008; Vanderhaeghe, 2009). A particularly important aspect of migmatitic rocks in orogens relates to rheology. The formation of partially molten rocks during orogenesis imposes a drastic weakening of the crust

(Rosenberg and Handy, 2005), which strongly influences the way the deformation is distributed and, consequently, the tectono-thermal evolution of entire orogenic belts (e.g., Vanderharghe and Teyssier, 2001; Sawyer et al., 2011).

Migmatites provide a large amount of geological information that includes the record of melt movement within a partially molten material, and the record of syn-anatectic deformation in both ancient and modern orogens (e.g., Brown et al., 1995; Nelson et al., 1996; Brown, 2001; Gébelin et al., 2009; Searle et al., 2010; Prakash et at., 2018). In hot orogens, the weak partially molten orogenic crust is prone to deform by gravity/pressure driven flow (e.g., Royden et al., 1997; Clark and Royden, 2000; Beaumont et al., 2006). The result of such deformation is recorded as a large-scale horizontal crustal flow associated with shallow-dipping structures (Beaumont et al., 2004; Jamieson et al., 2010). The evolution of such hot orogens become increasingly complex over time, due to the evolution of low-viscosity flow and to the concomitant high-temperature metamorphism, which can last for a long time due to continued conductive heat transfer, internal radioactive heating, and low erosion rates associated with plateau formation (e.g., Rivers, 2009; Jamieson et al., 2010; Clark et al., 2011; Horton et al., 2016). Such a hot setting also promotes the formation of "granitoids" that are hot and dry enough to contain orthopyroxene, i.e., charnockite *sensu lato*. These rocks can have a range of geochemical characteristics and can be associated with different geotectonic contexts, but in all cases, they are thought to ultimately have formed under temperature conditions as high as 1000 °C (Frost and Frost, 2008). Many charnockites have been recognized as the result of deep crustal melting, including dry melting of crustal rocks during granulite metamorphism, while others can be linked to differentiated mantle melts (Frost and Frost, 2008; Zhao et al., 2017)

It is necessary to integrate a variety of approaches and techniques to understand the evolution of hot orogens, the role of their associated anatectic rocks, and the meaning and implications of late hot intrusions. Morphological aspects observed in the field provide the best

criteria for determining whether partial melting has occurred or not, for investigating whether the melt separated from the solid fraction or not, and for evaluating if there was enough melt migration to form a granitic body or if melt accumulated in situ and/or in-source, i.e., if melt remained within the migmatite area (e.g., Barbey et al., 1996; Sawyer, 1994, 1999). Whole rock geochemistry, when coupled with good field-based control, can shed light on the processes (melting, segregation, and crystallization) that occurred in the region where the rocks were partially melted (e.g., Sawyer, 1999; Jung et al., 1995, 1999; Harris et al., 2004; Maharani, et al., 2016; Wolfram et al., 2017). Isotope systems such as Sr, Nd, Lu-Hf, and oxygen, bring information about the source material that was melted, i.e., the nature of the parent rock from which the magma was formed by partial melting (e.g., Jung et al., 1999; Sun et al., 2019). Geochronological data can constrain the timing of partial melting (e.g., Meira et al., 2019b; Sun et al. 2019) and crystallization. Numerical modeling can predict the heat sources and the processes that can keep the crust hot for an extended period of time (e.g., Clark et al., 2011; Gorczyk et al., 2013; Gorczyk and Vogt, 2015; Horton et al., 2016). From microscopic observations we can identify textures related to melt crystallization and melt-solid reactions, mineral assemblages from which melt-forming reactions can be inferred and investigate whether the deformation occurred at magmatic or solid state (e.g., Sawyer, 2008; Cavalcante et al., 2013) and finally, utilizing thermobarometry we can constrain the P-T conditions during partial melting (e.g., Brown, 2002; Harris et al., 2004; Cavalcante et al., 2014; Clark et al., 2015).

Several studies conducted over the last three decades have produced a large body of structural, geochronological, geochemical and petrological data that provides important constraints on the tectonic setting and orogenic processes of the hot Araçuaí belt (e.g. Trompette et al., 1993; Vauchez et al., 1994, 2007, 2019; Trompette, 1997; Pedrosa-Soares et al., 2001; Martins et al., 2004; Alkmim et al., 2006; Petitgirard et al., 2009; Mondou et al., 2012;

Cavalcante et al., 2013, 2014, 2018; Richter et al., 2016; Melo et al., 2017a, b; Angelo et al., 2020). However, key questions, especially those related to the geodynamic implications of the formation of a large migmatitic-anatectic area with evidence of being partially molten for a long time period (e.g., Cavalcante et al., 2018; Vauchez et al., 2019), have not received due attention. Furthermore, the geological meaning of late-stage emplacement of charnockitic intrusions is still not well understood.

Here we present new geochemical data (major and trace elements) from the hinterland of the Araçuaí belt, more specifically from the Carlos Chagas domain (henceforth CCD), two intrusive charnockite bodies, and the migmatites from the Nova Venécia Complex (henceforth NVC), to critically assess what these rocks record and represent. We also revisit in detail the morphological aspects of the CCD in particular, and also the migmatites from the NVC, to deepen our understanding of the migmatitic rock types and their structure. Therefore, this contribution also focuses on the textural aspects of the CCD rocks, as they have been interpreted both as anatexites and metagranites. We aim to address the following questions: Are the CCD rocks a record of in-source crustal anatexis during orogenic thickening, or are they originally granitic bodies that were metamorphosed during the orogeny? Do the CCD rocks record more than one anatectic episode with different geochemical signatures? What is the nature of the magmatism? Do all of these rocks originate from crustal melting or do they rather represent a mantle-enriched reservoir? In order to address these questions, we evaluate the chemical signatures of these rocks, the amount of melt, melt distribution (morphology) and composition produced during anatexis, together with an assessment of relevant geochronological and geochemical information, in the context of the tectonic evolution of the hot Araçuaí belt during the Brasiliano/Pan-African event.

2. Geological setting

The hot Araçuaí belt and its continuation to the south, the Ribeira belt, are part of the Mantiqueira Province, which extends northwards from Uruguay along the Brazilian coast as far as the state of Bahia (Fig. 1). Together, they represent a ~1000 km long and 100-400 km wide continuous orogenic belt (e.g., Vauchez et al., 1994; Egydio-Silva et al., 2018) trending N-S and NE-SW, respectively. They formed during the West Gondwana amalgamation, throughout the course of the Neoproterozoic Brasiliano/Pan-African event (Almeida et al., 2000). The orogenic-scale deformation is characterized by a progressive change from dominant top-to-west thrusting onto the São Francisco craton in the hot Araçuaí belt, to dominant transpressive deformation involving shortening normal to the belt and strike-slip dextral shearing, in the Ribeira belt (e.g., Trompette, 1994; Oliveira et al., 2000; Egydio-Silva et al., 2005; Vauchez et al., 2007).

The Araçuaí-Ribeira belt together with its African counterpart, the West Congo belt, has been considered as a confined orogen towards the north (e.g., Pedrosa-Soares et al., 2001; Alkmim et al., 2006) due to its embayed shape. It is bordered by cratonic lithosphere to the east (Congo craton), north and west (São Francisco craton), and remained in that configuration until the Atlantic opening in the Cretaceous. The tectonic evolution of the Araçuaí-Ribeira belt has been associated with two contrasting models that involve: (1) long-lived arc development (from 630 to 585 Ma in the Araçuaí; Tedeschi et al., 2016 and references therein; from 860 to 570 Ma in the Ribeira; Tupinambá et al., 2012; Heilbron et al., 2013; Peixoto et al., 2017), with the consequent involvement of a wide ocean and multiple terrane collisions, and (2) intracontinental orogeny associated with widespread *in situ* and in-source partial melting and a protracted molten state (Trompette 1994, 1997; Cavalcante et al., 2018, 2019; Meira et al., 2015; 2019a, b; Fossen et al., 2020a, b; Konopásek et al., 2020). The confined nature of this orogen entails important space constrictions, which together with the >60 km orogenic crustal

thickness estimated for its north portion (Cavalcante et al., 2014), and the apparently short time interval

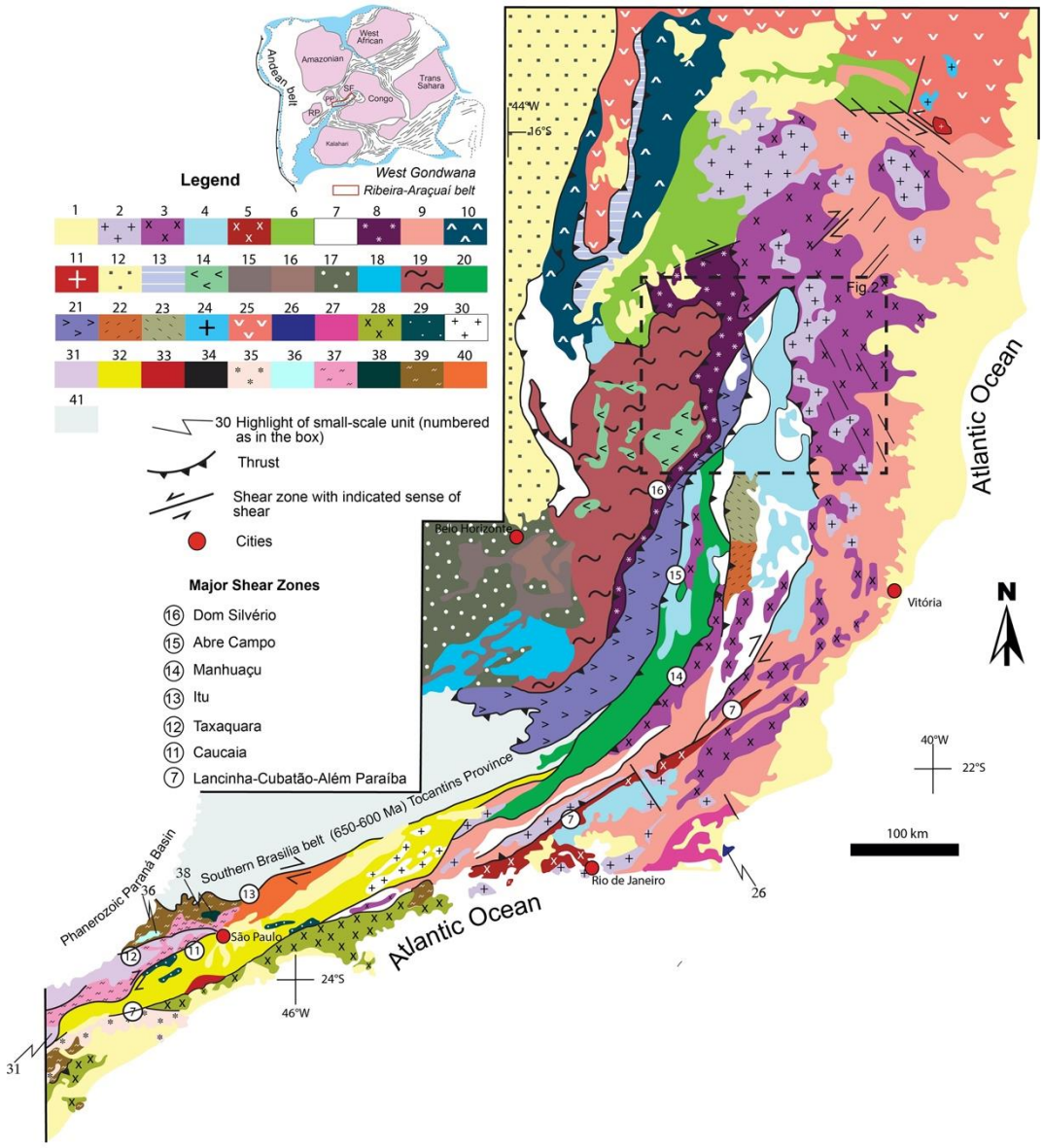

Figure 1: Geological map of the Mantiqueira province with schematic reconstruction of the West Gondwana. Lithological units relevant to this study: 2 = late orogenic magmatism including charnockitic rocks; 3 = Carlos Chagas domain; 4 and 7 = tonalite and granodiorite bodies (Galiléia, São Vitor, Rancho Alegre, Pedra do Sino and Derribadinha units); 8 and 21 =

mylonitic supracrustal rocks; 19 = Reworked Paleoproterozoic basement. For more information on the legend, see Silva et al. (2005).

between crustal stretching and onset of convergence in this orogenic system (Konopásek et al., 2017, 2018, 2020; Percival et al., 2021), puts into question the existence of any large-size ocean prior to orogeny in the northern portion, and restricts the size of the ocean to a maximum of 600 km south of the Ribeira belt (Konopásek et al., 2020), favoring a simpler model of intracontinental evolution for the whole Araçuaí-Ribeira belt.

The Araçuaí belt presents several characteristics of a hot orogenic system, such as: (1) large volumes of magma accumulated in middle to lower crustal levels (25-30 km depth) in its hinterland core (e.g. Cavalcante et al. 2013, 2014); (2) long-lasting high temperature metamorphic conditions (>700 to 800 °C) that allow partially molten rocks to exist for at least 30 My (Cavalcante et al. 2018); (3) high geothermal gradients (30-35 °C/km to a depth of ca. 25 km) and; (4) low cooling rates of 3-5 °C/My from 600 Ma over a period >100 My after zircon crystallization in the CCD, and over a period of at least 40 My in the Western and Central domains (Vauchez et al., 2019). As a consequence, the CCD cooled to temperatures of ~500 °C only at 510-500 Ma (Vauchez et al., 2019).

Temperature estimates from mylonites and anatexites suggest that deformation in the hot Araçuaí belt occurred under high temperature and low-pressure conditions, such as 730-780 ºC and 500-600 MPa in the westernmost portion of the belt, and ≥ 800 ºC and 600-700 MPa in its easternmost part (Petitgirard et al., 2009; Cavalcante et al., 2014; Richter et al., 2016; Melo et al., 2017a).

The Araçuaí belt can be broadly separated into three lithological domains (Fig. 2) that from west to east consist of: (1) high temperature paraderived mylonites with top-to-the west sense of movement, with injections of synkinematic leucogranitic veins at 577 ± 9 Ma (Western

domain; Petitgirard et al., 2009); (2) tonalite and granodiorite bodies (e.g., Galiléia, São Vitor, Rancho Alegre, Pedra do Sino, and Derribadinha units) crystallized between 618 ± 9 (Gonçalves et al., 2016) and 579 ± 4 Ma (Mondou et al., 2012; Central domain), and deformed mostly in the magmatic state, with metamorphism occurring between 555 ± 7 Ma and 589 ± 7 Ma (Gonçalves et al., 2016) and; (3) migmatites, anatectic, and porphyritic granites (CCD) that form an "anatectic sea", ~300 km long and 50-100 km wide as preserved today (Eastern domain; Cavalcante et al., 2013, 2014). From lithochemical data, Gradim et al. (2014) suggest that the CCD rocks are the result of partial melting of the NVC, involving progressive dehydration reactions and biotite breakdown. The CCD presents abundant evidence of metamorphic melting reactions and melt crystallization, with indications that metamorphism and associated melt production occurred at around 25 km depth, during a crustal thickening event that occurred no later than ca. 620 Ma (e.g., Cavalcante et al., 2014; 2018). The origin of the metamorphism and partial melting and consequently the geological meaning of such rocks are issues that have been intensely debated in the geoscience community (e.g., Cavalcante et al., 2019; Fossen et al., 2020a, b), as discussed in the following session. Metatexites and transitional metatexite-diatexite metamorphosed under granulitic conditions from the NVC occur southeast of the CCD and in its northern portion, and charnockite bodies are intrusive into the central portion of the CCD (Fig. 2).

2.1. The CCD: in-source migmatites or metamorphosed S-type granites?

The CCD rocks have been interpreted as migmatites associated with anatectic and porphyritic granites (Cavalcante et al. 2013, 2014, 2016, 2018), and as S-type granites that were metamorphosed twice under granulite facies conditions during two distinct metamorphic events (M1 and M2), with loss of melt (Melo et al. 2017a, b).

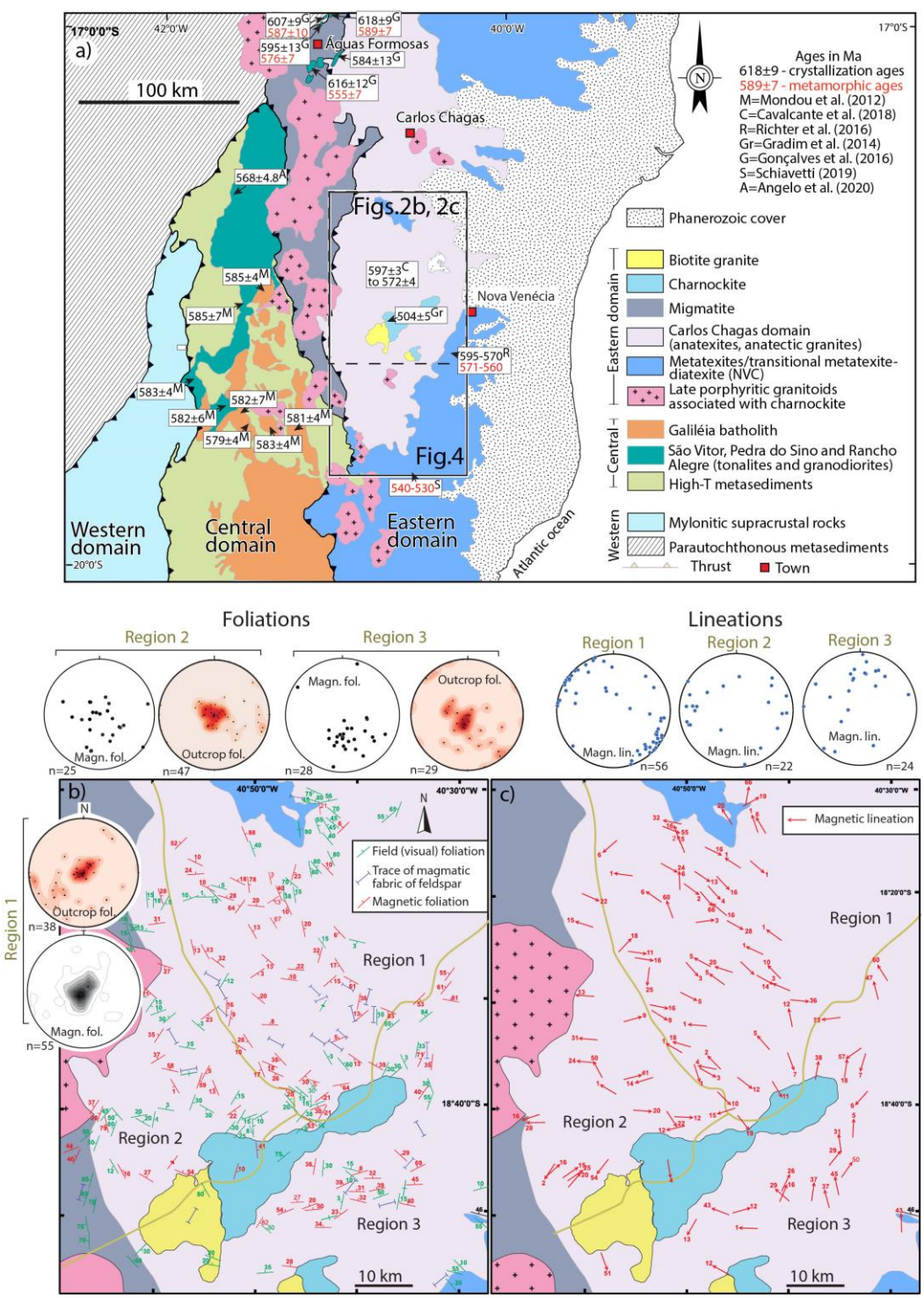

Figure 2: (a) Geological map of the Araçuaí belt (modified from Oliveira et al. 2000) and (b) and (c) Structural maps showing AMS (anisotropy of magnetic susceptibility) and field measurements across the CCD (modified from Cavalcante et al. 2013, 2016). Note the

predominant low-angle planar and linear fabrics, suggestive of inefficient vertical melt migration.

One of the main arguments of Melo et al. (2017a) to classify the CCD rocks as an S-type granite before being metamorphosed is the interpretation that monazites date the original crystallization event, based on the assumption that monazite only crystallizes from peraluminous magma. However, monazite can also be formed during prograde or retrograde metamorphism (Smith and Barreiro 1990, Rubatto et al. 2001; Wing et al. 2003; Kohn & Malloy 2004; Corrie & Kohn 2008; Kelsey et al. 2008), or even during diagenesis (e.g., Richard et al. 2015; François et al. 2017). The dates obtained by Melo et al. (2017a, b) are summarized in Figure 3 and Table 1 (supplementary material). The monazites dated by Melo et al. (2017b), which occur as inclusions in the core of what they consider a first generation garnets (Grt_1 in their table 3) and in the matrix (M), display ages of 617 ± 12 Ma and 612 ± 17 Ma, respectively, and were interpreted as inherited from the source of their Carlos Chagas granite. Based on these inherited ages, which overlap some of the U-Pb dates obtained from detrital zircon and monazites from the NVC (606-612 Ma; Richter et al., 2016), Melo et al. (2017b) suggest that their Rio Doce arc, corresponding to our Central domain (Fig. 2), represents material similar to the source of the CCD. U-Pb zircon dates ranging between 602 ± 12 Ma and 826 ± 15 Ma obtained by Melo et al. (2017a) were also interpreted as inherited ages, i.e., zircon grains extracted from the CCD source rocks. The inheritance character of these zircons (ca. 826-600 Ma), as well as the interpretation of magmatic (578 to 588 Ma) and metamorphic zircons (ca. 570-550 and 535-500 Ma), are based on cathodoluminescence images, because the wide variation in Th/U values does not allow for discrimination of zircons.

A second argument is based on the observation that the Carlos Chagas rocks studied by Melo et al. (2017a, b) did not contain orthopyroxene. However, we observed orthopyroxene in

two samples of the Carlos Chagas (see section 4.1) but given that these samples are close to the contact against a mafic granulitic body (metatexites), further investigations are required to better understand its presence in the Carlos Chagas mineral assemblage.

Considering that Melo et al. (2017b) define the Carlos Chagas rocks as an S-type granite, their inherited monazites could be detrital grains of metamorphic or igneous origin, embedded in the sedimentary source rocks which would later melt to generate the S-type Carlos Chagas granite, or they could be diagenetic grains formed during the diagenesis of the Carlos Chagas source rocks, or metamorphic grains formed as the Carlos Chagas source rocks reached metamorphic conditions. These monazites also display ages between 569 ± 14 Ma and 552 ±15 Ma, interpreted to date their first metamorphic peak (M1; Table 1), and between 535 ± 14 Ma and 516 ±14 Ma, interpreted as their second metamorphic event (M2) recorded in the Carlos Chagas rocks.

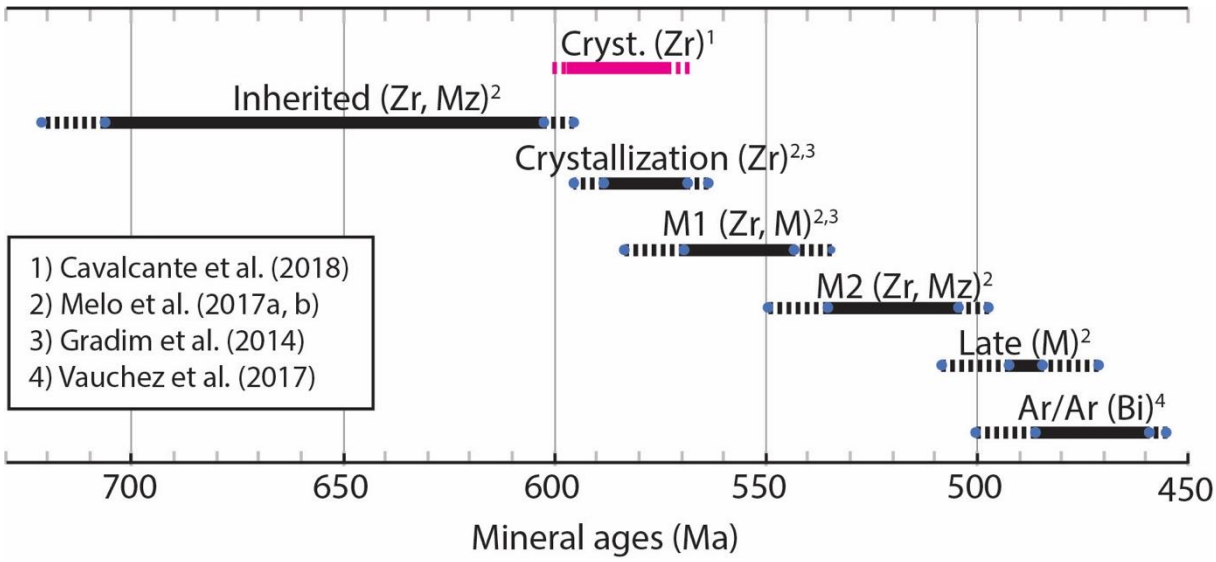

Figure 3. U-Pb in zircon (Zr) and monazite (M) and Ar-Ar biotite (Bi) ages obtained in the CCD, showing the overlap between crystallization and inherited ages, crystallization and M1 (metamorphism 1) ages, and M1 and M2 (metamorphism 2) ages, and between Late (later fluid-

299 rock interaction during gravitational collapse) and Ar-Ar biotite cooling. Compilation based on
300 Table 1.
301
302 Bearing in mind the large analytical uncertainties, some of the older ages obtained by
303 Melo et al. (2017b) and interpreted by them as inherited from the Carlos Chagas source and the
304 younger ages interpreted as M1 both overlap in time with the crystallization interval from 597
305 ± 3 to 572 ± 4.4 Ma (U-Pb in zircon), obtained by Cavalcante et al. (2018) for the CCD (Fig.
306 3). Based on strongly fractioned REE pattern and Th/U ratios < 0.1, Cavalcante et al. (2018)
307 postulated the simultaneous crystallization of zircon and monazite in the Carlos Chagas rocks
308 (e.g., Yakymchuk, et al., 2018). Furthermore, considering the analytical error reported, some
309 ages obtained in monazite and zircon from samples CC31 and CC37, interpreted by Melo et al.
310 (2017b) as M1 and crystallization, also overlap in time (Fig. 3; Table 1).
311 The crystallization interval obtained by Cavalcante et al. (2018) also encompasses the 577
312 ± 6 Ma and the 576 ± 3 Ma U-Pb ages obtained by Melo et al (2017b) and interpreted as their
313 best ages for the crystallization of the Carlos Chagas rocks, and the U-Pb zircon ages of 568 ±
314 5 Ma and 563 ± 13 Ma obtained by Gradim et al. (2014). Gradim et al. interpreted these as
315 magmatic and metamorphic ages, respectively, apparently discarding their clear overlap in
316 time. Gradim et al. (2014) also obtained a zircon age of 549 ± 28 Ma from an "ultramylonitic"
317 Carlos Chagas sample (their sample 472) that they suggest could be related to the "final
318 collisional processes for the Carlos Chagas batholith". Considering the large error uncertainty,
319 this age also overlaps with the ages interpreted as magmatic and metamorphic in that same
320 work. Furthermore, it seems that their "ultramylonitic" rock presented as their Figures 8K, 9F,
321 and 9G represents the leucosome portion of the Carlos Chagas migmatite, with peritectic garnet
322 and sillimanite. Intriguingly, there is no indication of any characteristic ultramylonite
323 microstructures, such as fine-grained recrystallized matrix with >90% of new grains with size

< 10 μm (e.g., Sibson, 1977; Vernon et al. 2004; Davis et al., 2012), in their figures. Regardless, the large analytical uncertainties for the ages obtained by Gradim et al. (2014) make any conclusive interpretation very difficult.

Young U-Pb dates ranging between 484 ± 13 Ma and 492 ± 16 Ma were also obtained from monazite by Melo et al. (2017b). These ages were interpreted as the result of later fluid-rock interaction during gravitational collapse of the Araçuaí belt. Interestingly, these younger ages fall into the 459 ± 4 Ma and 486 ± 4 Ma time interval defined by ^{40}Ar-^{39}Ar ages in biotite, interpreted as biotite cooling through its closure temperature at around 336–306 °C (Vauchez et al., 2019) (Fig. 3; Table 1). The oldest and youngest ^{40}Ar-^{39}Ar ages obtained by Vauchez et al. (2019) come from samples in the northernmost and southernmost part of the CCD, respectively. Such an age distribution is also observed in the U-Pb zircon crystallization ages obtained by Cavalcante et al. (2018).

The Carlos Chagas rocks present high SiO_2 (62 – 76 wt%; Cavalcante et al., 2014; Table 2 in the supplementary material), Al_2O_3 (13 – 16 wt%; Cavalcante et al., 2014) and Ni (0.8 – 9 ppm; Table 2) contents, and low Na_2O_3 (< 3 wt%; Cavalcante et al., 2014; Table 2), CaO (0.5 – 3.4 wt %; Cavalcante et al., 2014; Table 2), and Sr (18 – 197 ppm; Table 2) contents, a chemical composition that is similar to both a S-type granite as defined by Chappell (1984) and a metasedimentary-derived migmatitic rock as presented by, for example, Sawyer (1998). Furthermore, migmatites can have widely different protolith compositions (pelites to mafic rocks and beyond). Therefore, chemical composition does not seem to be the best criterion for deciding whether these rocks are metamorphosed granites or migmatites. In terms of field relations, the Carlos Chagas rocks do not exhibit evidence of being intrusive. Instead, the large amount of anatectic rocks with peritectic minerals, evidence of in-source partial melting structures and flow structures (see sections 3 and 4) suggest that melt and magma migration was not efficient enough to form a large granitic body emplaced in upper crustal levels. This is

also supported by detailed Anisotropy Magnetic Susceptibility (AMS) mapping, which has revealed a predominantly subhorizontal magmatic foliation and a structural continuity between domains with different magmatic flow directions (Cavalcante et al., 2013). This fabric suggests that deformation during crustal thickening was dominated by a vertical gravity force, caused by the weight of the orogenic upper crust on top of the CCD. This suggests that the magmatic fabric recorded in the CCD formed in a vertically confined tectonic setting that prevented efficient upward magma movements to form intrusions. Such a "trapped" setting therefore does not allow efficient melt migration out of its source region, i.e., out of the middle crust. We find no evidence in the literature supporting that Carlos Chagas rocks were first emplaced in upper crustal levels before 570 Ma, and subsequently buried and metamorphosed at 570-550 Ma, as suggested by Melo et al. (2017a, b). Efficient melt migration from the source to emplacement at upper crustal levels would likely produce vertical lineation and foliation, as observed for example in the Central tonalitic domain west of the CCD (Region 2 in Figure 6 of Mondou et al., 2012). Furthermore, efficient melt migration needed to form isolated granitic bodies at upper crustal levels is strongly controlled by tectonic settings, in which weak or permeable structures, such as shear zones, facilitate vertical magma flow (e.g., Solar et al., 1998; De Saint Blanquat et al., 2011; Cavalcante et al., 2016). Such structures attesting strain localization and dominant solid-state deformation at a large scale are not observed in the CCD. Instead, the observed fabrics suggest a rather homogeneous strain distribution (e.g., Cavalcante et al., 2013; 2016).

The Carlos Chagas migmatites and anatectic granites, including porphyritic granites with large tabular feldspar phenocrysts oriented along a well-defined magmatic foliation, display several characteristics of extensive *in situ* and in-source crustal partial melting of the Araçuaí middle crust, as demonstrated in detail in the next sections. This means that the melt/magma generated from partial melting of metasedimentary rocks remained in, or close to where it was

generated. We therefore reinforce that the Carlos Chagas rocks are of local derivation, product of *in situ* and in-source partial melting of the middle crust, i.e., a crustal layer of migmatites and parautochthonous granites, generated at depths of ca. 25 km in response to crustal orogenic thickening (e.g., Cavalcante et al., 2013, 2014), or generated even deeper at 26-29 km (e.g., Melo et al. 2017b). These hot rocks were likely partially molten between ~600 and 570 Ma at temperatures between 815 and > 700 ºC (Cavalcante et al., 2018), and crystallized during slow cooling (3-5 ºC/My; Vauchez et al., 2019).

2.2. The Nova Venécia Complex (NVC)

The migmatitic rocks from the NVC (also called Jequitinhonha, Paraíba do Sul, or migmatite-granulite-granite complex) have been interpreted as a back-arc sedimentary deposit (Noce et al., 2004; Gradim et al., 2014; Richter et al., 2016), with a maximum sedimentation age of 606 Ma (Richter et al., 2016). They were metamorphosed at upper amphibolite and granulite facies, with estimated peak conditions of 750-850 ºC and 530-750 MPa at ca. 571-560 Ma (Munhá et al., 2005; Richter et al., 2016). Recent work, however, suggests that peak metamorphism occurred at 540-530 Ma (Lu-Hf garnet dating in granulites) at ~850 °C and 575-610 MPa (Schiavetti, 2019), in agreement with a Sm-Nd three-points isochron age at 538 ± 38 Ma (garnet-whole rock-quartz/feldspar) obtained in a biotite-garnet-sillimanite-cordierite gneiss from the Eastern domain (Brueckner et al., 2000). U-Pb dating in detrital zircons produced ages of 590-641 Ma, 649-652 Ma, 733-810 Ma, 901 Ma and 2086-2124 Ma, indicating different sources of the NVC migmatites, such as the Rio Doce and Rio Negro arcs, Tonian rift-related magmatic rocks of the precursor basin, and the Paleoproterozoic basement (Noce et al., 2004; Gradim et al., 2014; Richter et al., 2016). The Rio Doce arc has been considered as the main detrital source for the NVC from ca. 650-610 Ma (Richter et al., 2016). U-Pb dating of a deformed and migmatized-foliated granite (called Ataléia suite in Gradim et

al., 2014) produced ages of 590 ± 7 Ma and 587 ± 9 Ma (samples 66A and 475 in Gradim et al., 2014), interpreted as crystallization ages of melts generated by melting of the NVC. An age of 571 ± 5 Ma was interpreted to date metamorphic recrystallization of these granitic rocks (sample 66A in Gradim et al., 2014).

2.3. The Charnockitic bodies

The occurrence of charnockitic bodies, part of the Padre Paraíso unit, has been attributed to a late (520-480 Ma) post-collisional event in the Araçuaí orogen (Pedrosa-Soares et al., 2011 and references therein). U-Pb dating in zircon produced an age of 504 ± 5 Ma, interpreted to date crystallization of the charnockite that intruded the central portion of the CCD (sample 470 in Gradim et al., 2014), while Melo et al. (2020) recorded a range of dates between 510-498 Ma for the Barra de São Francisco body.

Geochemical data (major and trace elements) from rocks related to this late event has attributed their origin to contrasting sources, involving mafic contributions of an enriched mantle, partial remelting of a metaluminous continental crust, dehydration melting from peraluminous crustal portions, differentiation, and host rock assimilation (e.g., Bayer et al., 1986; De Campos et al., 2004). Previous authors have considered this late-stage magmatism as a result of gravitational collapse of the orogen (Pedrosa-Soares et al., 2011), fueled by slab break-off and lithospheric delamination (Gradim et al., 2014).

However, considering the possibility that the Araçuaí belt may be an example of intracontinental orogeny (e.g., Cavalcante et al., 2019; Fossen et al., 2020a), and that the composition of these rocks implies that high-temperature conditions existed in the lower crust and the underlying mantle until ~500 Ma, the origin of this late magmatism is still unclear. Recent work has postulated that such magmatism could represent a limited reactivation of the

Araçuaí belt in response to the formation of the Congo-Cabo Frio belt, during final convergence between African and South American protocontinents (Vauchez et al., 2019).

3. Macroscale migmatitic structures

The general morphological aspects of the rocks from the CCD and migmatitic rocks from the NVC at macro- and microscales have been extensively described in several studies (e.g., Cavalcante et al., 2013, 2014, 2016; Gradim et al., 2014; Richter et al., 2016). Here we will focus on the migmatitic characteristics, following the first-, second-, and third-order classification of Sawyer (2008), and Yakymchuk (2021), and the definitions of the terms metatexis, diatexis and migmatite as established by Brown (1973), in order to properly access the morphological aspects of the migmatitic rocks, especially the CCD. Additionally, we describe the field aspects observed in the charnockitic bodies intrusive into the CCD.

Based on Sawyer (2008) classification, we consider metatexites as the lithological facies in which pre-anatectic structures occur and/or the amount of neosome (leucosome + melanosome) is low (< 20%), and diatexites and anatectic granites as the ones that lack such structures and contain a high percentage of neosome, schlieren features, vein-like leucosomes and flow structures attesting to pervasive partial melting (e.g., Sawyer, 1999). Also, diatexites and anatectic granites are considered as similar lithological facies, given that in the study area, diatexites often tend to grade into anatectic granites, without defining clear boundaries at the outcrop scale. Outcrops where we only observe an accumulation of leucosome rich in garnet are classified as diatexites, and those where we observe such an accumulation together with a clear magmatic planar fabric, we classify as diatexites/anatectic granite. Porphyritic granite is the term used for lithological facies with a high percentage (50 to 70%) of large tabular/euhedral feldspar grains that are moderately to strongly oriented, immersed in a garnet- and biotite-rich matrix. The distribution of these facies is illustrated in Figure 4.

Leucosome is defined as the light-colored part of the neosome, made up mostly of minerals crystallized from the anatectic melt, and melanosome as the part of the neosome rich in dark minerals, mostly peritectic. These dark minerals are interpretated as the solid, residual fraction left after some, or all, of the melt has been extracted. Therefore, often the melanosome is also the residuum, although, especially in the CCD rocks, melanosomes can also contain dark minerals, such as garnet and biotite, with evidence of being crystallized from the melt. For the CCD we observe a dominance of diatexites and anatectic granites spatially associated with metatexites and porphyritic granites, and a large variety of morphology in rocks with similar compositions. For the NVC we observe rocks with a large amount of neosome, with more melanosome than the CCD, and with paleosome represented mostly by lenses of calc-silicate rocks.

3.1. Field aspects of the Carlos Chagas anatexites and associated granites (CCD)

The CCD consists of peraluminous rocks, mostly diatexites/anatectic granites (90% leucocratic and 10% meso- to melanocratic diatexites), and metatexites and porphyritic granites. The diatexites/anatectic granites often present wide leucosomes (up to 10 cm) and abundant biotite schlieren (Fig. 5a). Leucosomes from both diatexites and metatexites are rich in garnet, feldspar and quartz, while melanosomes are rich in feldspar and biotite in the diatexites, and in garnet, feldspar and biotite in the metatexites.

The leucosomes form interconnected networks (net-structured diatexite) that are locally folded (fold-structured diatexite). They also form pools (Fig. 5b) in dilatant structural sites or shear bands at moderate angles to the foliation, which is defined by alternating leucosome and melanosome. Such structures suggest abundant (20-50%) melt accumulation (e.g., Guernina and Sawyer, 2003). The leucosomes often exhibit diffuse/gradational margins (Fig. 4, picture 1119), and contain accumulated garnets, especially in diatexites (Fig. 4, picture 1171), and

sharp, straight and feathery margins in metatexites, typically of *in situ* and in-source leucosomes. Melanosome portions often occur as scholle structures, mostly lenticular in shape. Both melanosome and leucosome often have large aligned tabular feldspar grains (up to 8 cm long) that together with quartz and biotite schlieren form a magmatic foliation (Figs. 5a, 5c).

Metatexites often exhibit stromatic structures with thin (1-3 cm) and thick (~10 cm) discontinuous layers of leucosomes alternating with residuum (melanosome) rich in biotite, pyroxene and ilmenite (Fig. 5d). We interpret this alternating aspect as remnants of gneissic layering.

Porphyritic granites exhibit aligned euhedral tabular feldspar grains that reach 10 cm in length embedded in a biotite and garnet-rich matrix, defining a magmatic flow fabric (Figs. 5e, 5f).

3.2. Field aspects of the migmatitic rocks from the NVC

Southeast of the CCD these rocks are metatexites and transitional metatexite-diatexite rocks, which have a larger proportion of melanosome in comparison to the Carlos Chagas migmatites (Figs. 6a-d). They have quartz-feldspar leucosome bands rich in garnet alternating with melanosome bands containing biotite, cordierite, K-feldspar, garnet and sillimanite, and calcsilicate rocks forming lenticular schollen paleosome (Fig. 6a). They often present stromatic migmatitic features formed by alternating layers consisting of melanosome/paleosome and leucosome (Figs. 6a, 6b, 6c). This planar fabric trends NNW-SSE, NNE-SSW, NE-SW and NW-SE with dips ranging from subhorizontal to subvertical (Fig. 4). The garnet-bearing leucosome displays sharp and straight margins (Fig. 4, picture 1076 and ES06). Close to the boundary with the CCD these rocks exhibit garnet-poor leucocratic bands rich in feldspar and quartz that progressively pass into more garnet-rich domains. These more leucocratic bands are laterally surrounded by narrow biotite-rich mafic selvedge (Fig. 6d).

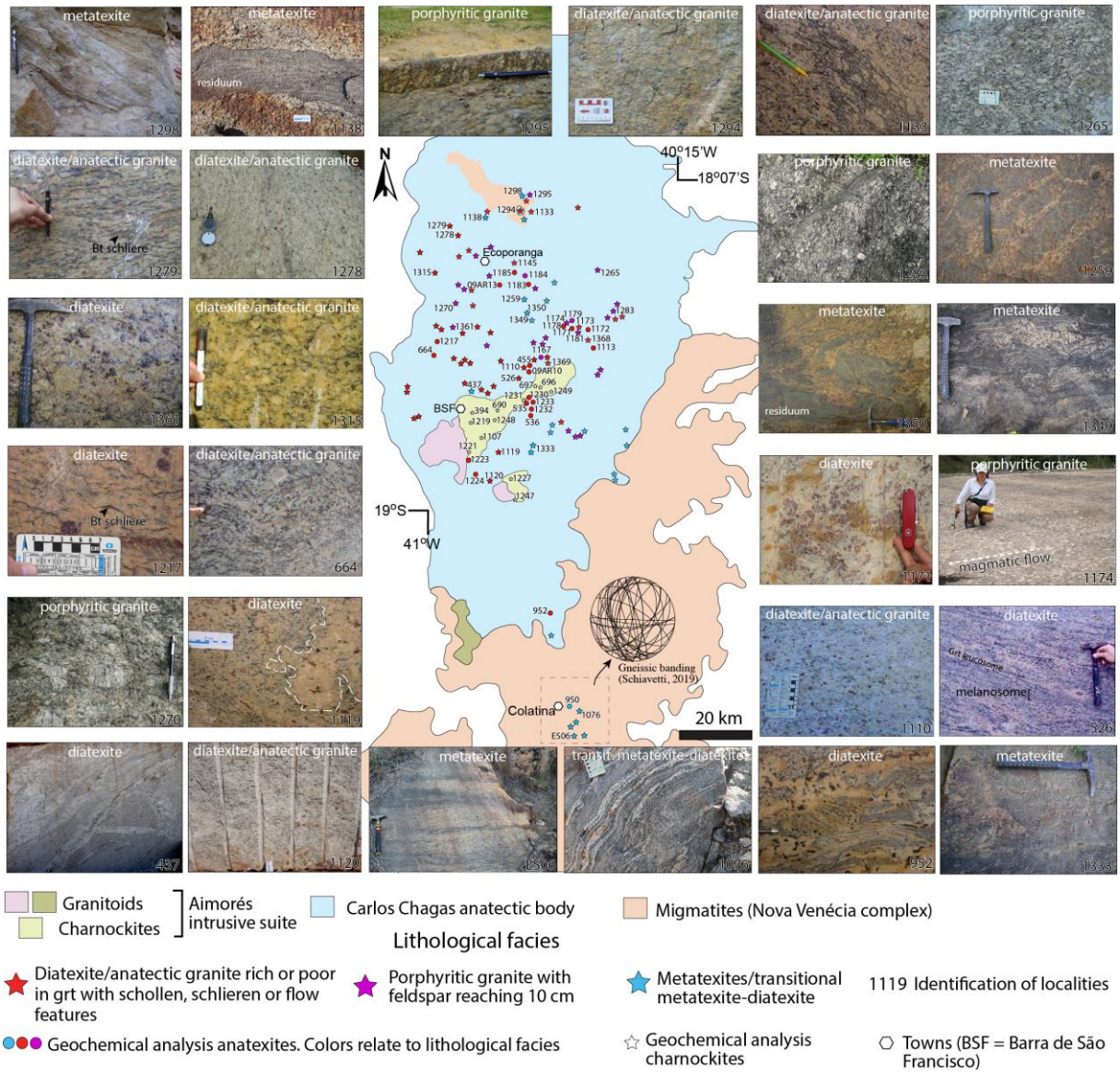

Figure 4: Distribution of the lithological facies of the CCD and the migmatitic rocks from the NVC, with representative pictures of outcrops. Pictures 1119 and 1171 display, respectively, a diffuse/gradational margin of leucosome (dashed line), and accumulated garnets in diatexite from the CCD. Pictures ES06 and 1076 show garnet-bearing leucosomes and melanosomes with sharp and straight margins in migmatites from the NVC. The occurrence of metatexites associated with diatexites and leucogranites in short distances between outcrops suggests in-

source partial melting of the middle crust and inefficient melt migration to form isolated granitic bodies. See text for discussion.

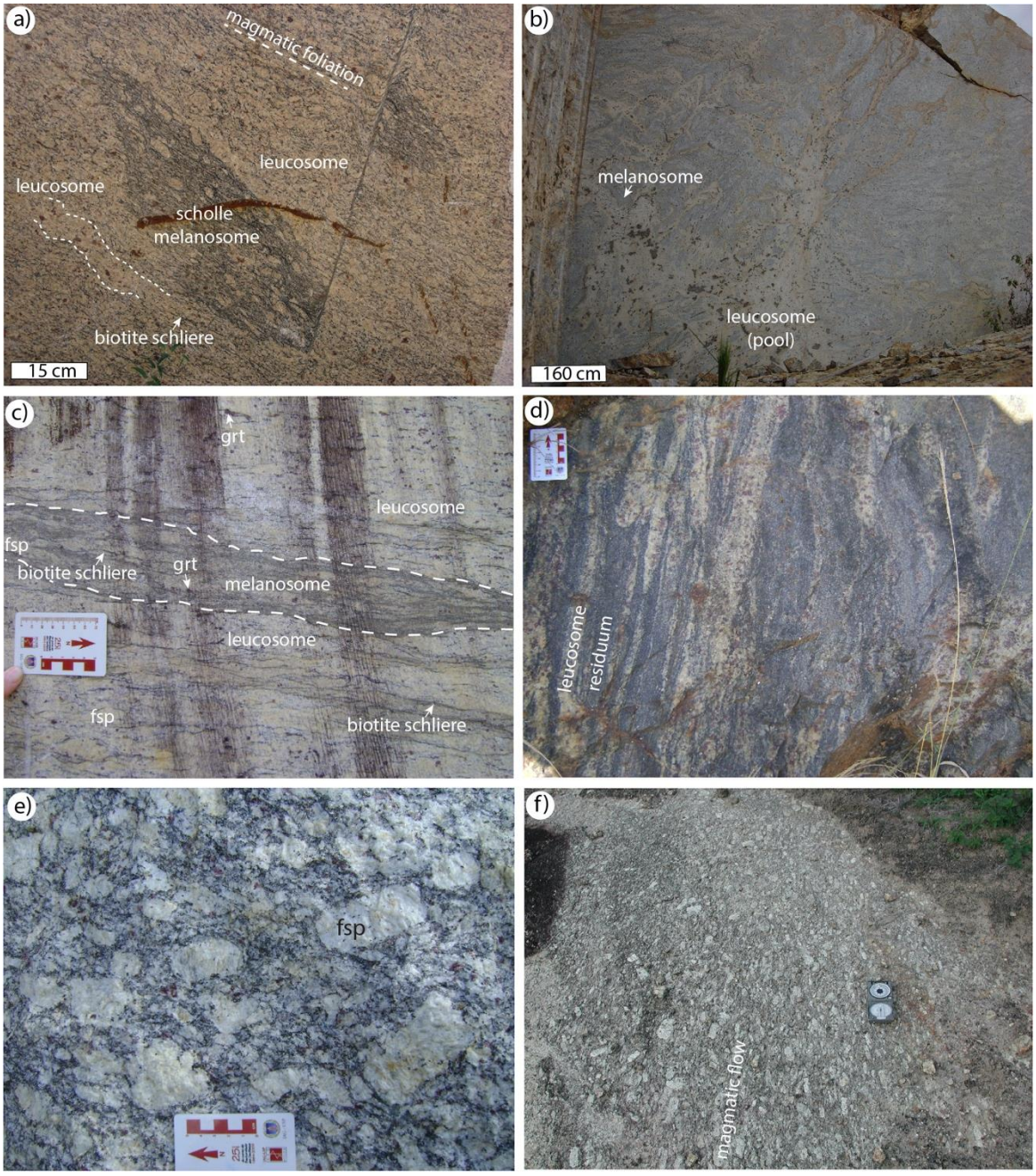

Figure 5: Field aspects of the CCD. (a) Diatexite/Anatectic granite with abundant biotite-rich schlieren and lenticular schollen structures, and with magmatic foliation characterized by preferred orientation of feldspar, quartz and biotite. Note the later normal fault displacing the

scholle melanosome. Dashed lines highlight a leucosome domain poor in biotite. This migmatite is entirely composed of neosome. (b) Fold-structured diatexite consiting entirely of neosome, with leucosome forming an in-source interconnected network, suggesting > 50% of partial melting, and "pools" of melt. (c) Diatexite with layers of leucosome rich in garnet and feldspar alternating with melanosome layers rich in garnet and biotite schlieren, forming a magmatic foliation. Dashed lines separate melanosome from leucosome portions. Grt=garnet and fsp=feldspar. (d) Metaxite with stromatic folded leucosome rich in garnet, feldspar and quartz alternating with residuum rich in biotite and pyroxene. (e) and (f) Porphyritic granites with large euhedral feldspar grains forming a magmatic flow fabric.

The metatexites from the NW-SE body in the northern portion of CCD can be of massive aspect (Fig. 6e; sample #1128 in Fig. 7), with small discrete patches of leucosomes with feathered margins (Fig. 3F in Cavalcante et al., 2014), suggesting local derivation (e.g., Pawley et al. 2013), or exhibiting a foliation characterized by alternating mafic and felsic layers oriented 170/80 SW (strike/dip; samples #1292 and #1293 in Fig. 7), locally folded (Fig. 6f).

3.3. Field aspects of the Charnockite and its associated granites

The charnockitic rocks form a main body of ~40 km length, oriented NE-SW in the central portion of the study area, and a smaller body of ~10 km length south of the main body (Figs. 2 and 4). They are dark green colored rocks, with phaneritic and porphyritic texture (Fig. 6g), containing large (up to 5cm) euhedral crystals of feldspar (orthoclase and andesine) that often show a preferred orientation. Centimetric to metric angular gneiss xenoliths (Fig. 6h) that display evidence of interaction with the magma (e.g., reaction rims) occur near the border of the charnockite bodies. These rocks show both abrupt and gradational contacts with a leucogranite (sample #697; Fig. 6i). When the contact is gradational, the transitional

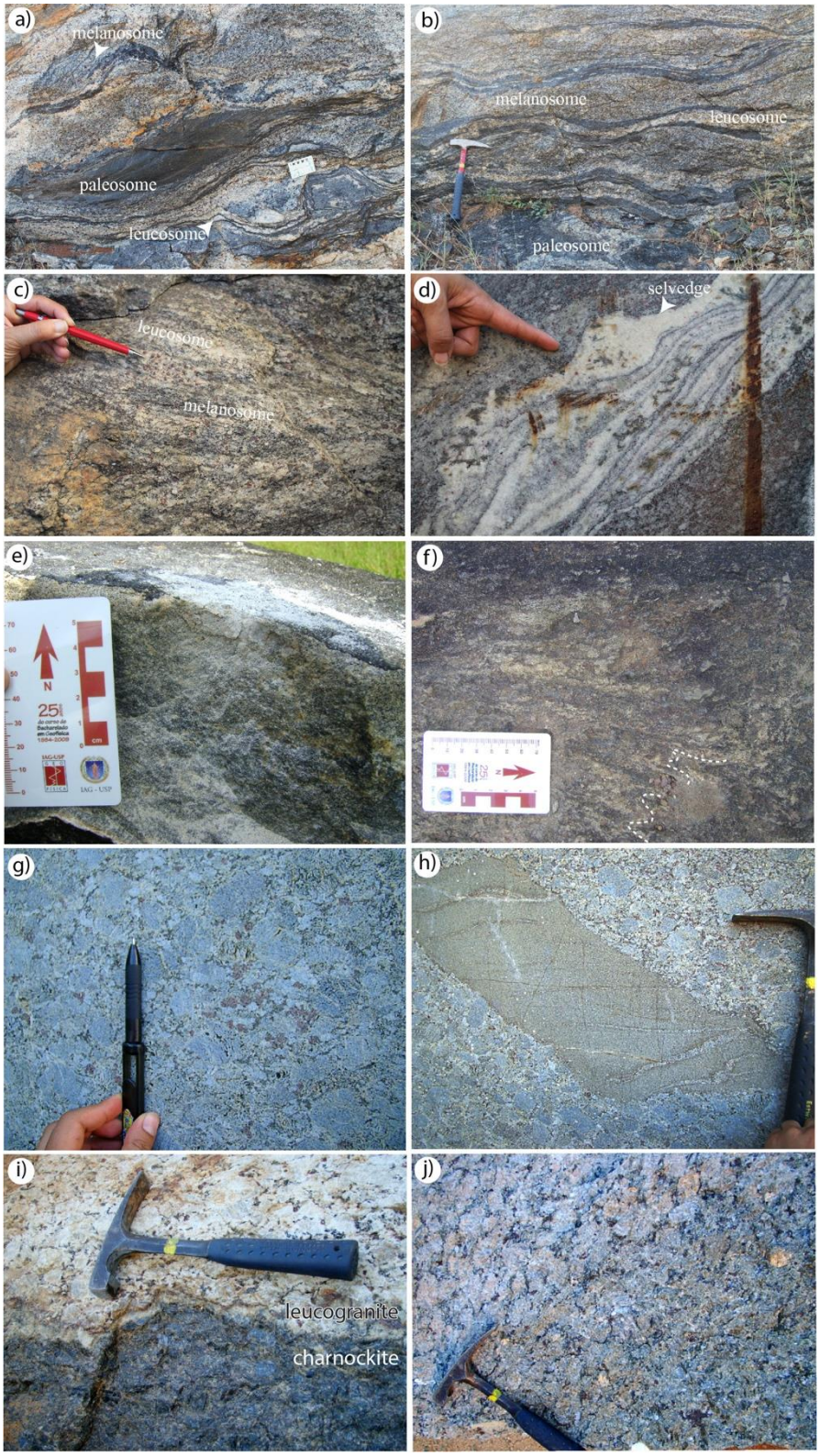
a)
melanosome
paleosome
leucosome
b)
melanosome
leucosome
paleosome
c)
leucosome
melanosome
d)
selvedge
e)
f)
g)
h)
i)
leucogranite
charnockite
j)

Figure 6 - Field aspects of the migmatitic rocks from the NVC (a-d = southeast of CCD; e and f = northern portion of CCD) and charnokite (g-j), which is intrusive in the CCD. (a), (b) and (c) The different parts of mafic transitional metatexite-diatexite displaying mafic paleosome with lenticular shape (a), stromatic banding with high proportion of melanosome and paleosome relative to leucosome, forming alternating layers (b), and leucosome with high concentration of garnet that progressively pass to melanosome (c). (d) Narrow biotite-rich mafic selvedge surrounding a leucocratic band of feldspar and quartz. (e) The massive aspect of the migmatitic granulites (metatexites) and (f) plagioclase-sillimanite rich layers folded (dashed lines). (g) Charnockite with porphyritic texture and feldspar phenocrystals up to 5 cm in size, in a matrix of quartz, feldspar, garnet and biotite. (h) Angular mafic xenolith with reaction rim in porphyritic charnockite. (i) Abrupt contact between charnockite and leucogranite. (j) Orange colored charnockite observed in a gradational contact with a leucogranite.

charnockitic facies is light orange in appearance and also does not have orthopyroxene (Fig. 6j); thus, these transitional Opx-free rocks are also considered as granites, along with the leucogranites. The geochemistry of these granites is also described in subsequent sections, but we note that their chemical composition is completely different from the CCD, and therefore, they should not be considered as a part of the CCD, as they have no genetic relationship.

4. Microscale structures of the anatectic domain

From 191 thin sections collected in 91 localities (Fig. 7), we will here describe and interpret the textural aspects of the rocks in the anatectic domain. The anatectic microscale aspects of the migmatitic rocks from the NVC are well documented by Gradim et al. (2014) and Richter et al. (2016), and it seems that there is a consensus that these rocks are migmatites and therefore display evidence of partial melting and melt crystallization.

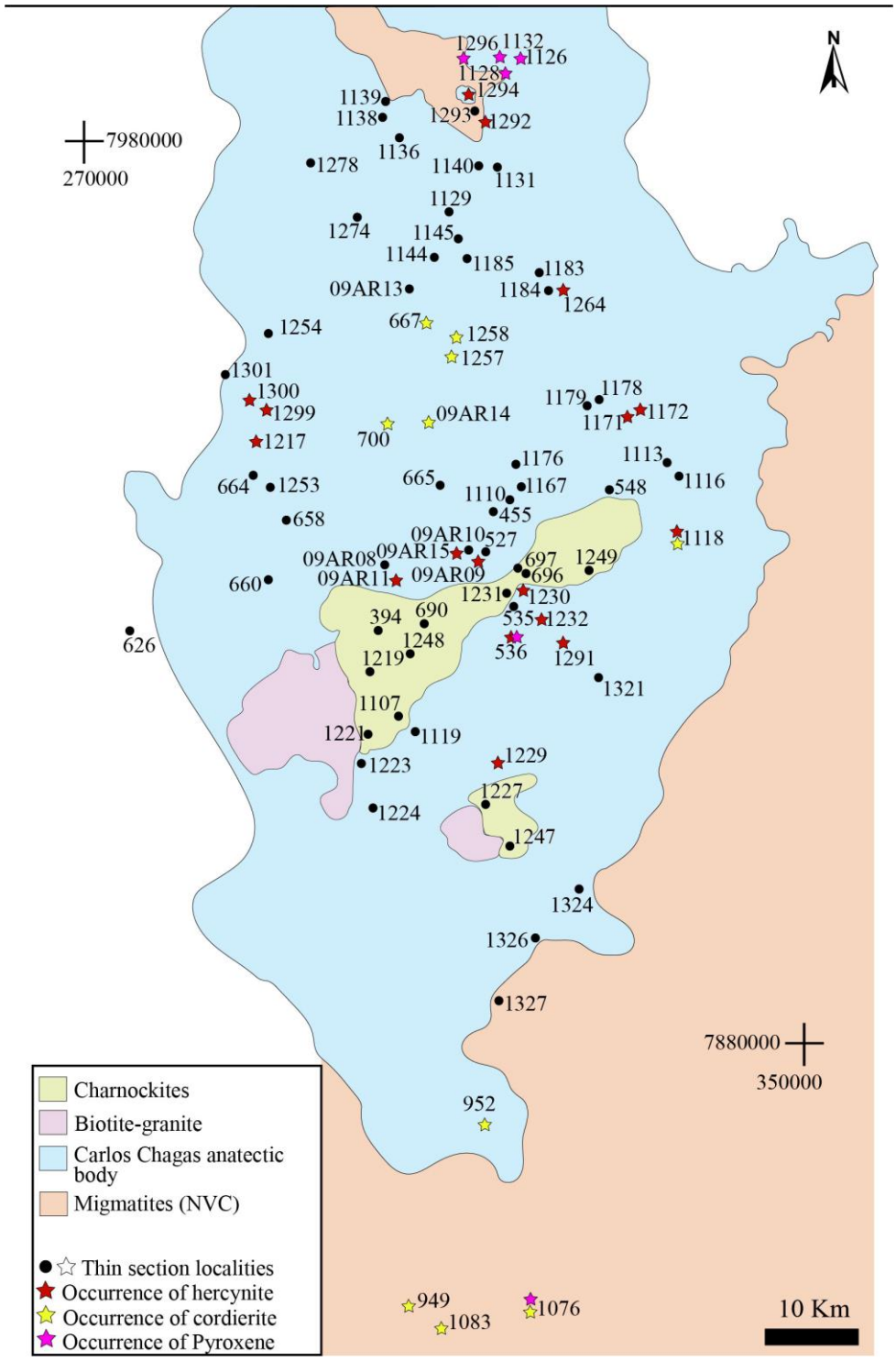

Figure 7: Simplified Geological map of the anatectic core of the Araçuaí belt displaying the location of thin sections used in this work and the occurrence of hercynite, cordierite and pyroxene.

Therefore, in this section we will focus on the microscale structures observed in the CCD, because these rocks have been described both as granite that were subsequently metamorphosed (Melo et al., 2017a, b) and as migmatites associated with granites (Cavalcante et al., 2013, 2014, 2016, 2018), and in the charnockites. Microstructure's description is in accordance with Vernon and Collins (1988), Vernon (2004, 2011) and Sawyer (2008). Abbreviations are according to Whitney and Evans (2010).

4.1. Carlos Chagas rocks

The textural aspects of the CCD are based on the observation of 141 thin sections from 71 localities (Fig. 7). All the CCD rock types present a main mineral assemblage composed of Afs + Qtz + Pl + Grt + Bt ± Sil. Hercynite occurs more frequently than cordierite (Fig. 7). Two samples from the north portion of CCD, close to the contact with granulitic rocks (NVC metatexites) have amphibole and pyroxene (#1126), and pyroxene (#1132). Accessory phases are zircon, ilmenite, monazite, apatite, rutile, and tourmaline.

Leucosomes from both metatexites and diatexites are very similar in composition, consisting mainly of garnet, quartz, and usually larger feldspar grains (up to 10 mm). The melanosome, however, have different compositions, being enriched in biotite, plagioclase and sillimanite in the metatexites, and in biotite in the diatexites, although the biotite generally occurs in smaller proportions in the diatexites than in the metatexites. The textures of migmatitic rocks represent, to a greater or lesser extent, modifications associated with partial melting, either by consuming or producing reactions, and related to melt crystallization, as described below.

Metatexites

Metatexites are abundant in Pl and contain variable amounts of Qtz + Crd + Sil + Bt + Afs + Ilm + Ms + Grt. Accessory phases are apatite, monazite, zircon, hercynite, and rutile. The metatexites have a few outstanding differences from the diatexites at the microscale that include smaller sizes of melanosome grains, pervasive solid-state deformation in plagioclase, and greater proportions of biotite and sillimanite (Figs. 8a, 8b).

Quartz is mostly interstitial and anhedral, and sometimes occupies embayments in garnet (Fig. 8a). It is generally free of intracrystalline deformation, and solid-state deformation is only locally observed by the presence of weak undulose extinction and a few large subgrains. Quartz-plagioclase intergrowth often forms myrmekites.

Plagioclase and K-feldspar often exhibit anhedral and subeuhedral shapes and occur in association with garnet, sillimanite, and biotite, especially in the melanosome. However, some euhedral K-feldspar grains with crystal faces against quartz grains, which we interpret to be crystallized from the melt (e.g., Vernon, 2011), also occur (Fig. 8b).

Biotite grains are brown and red colored, establish corroded boundaries with plagioclase, have strong preferred orientation, and sometimes occur as inclusions in garnet. The presence of deformation twins in plagioclase, which occurs in association with interstitial quartz with weak or without evidence of solid-state deformation (Fig. 8b), indicates that the deformed plagioclase is residual, therefore its solid-state deformation microstructure is pre-partial melting. Such a solid-state microstructure reinforces the classification of these rocks as metatexites.

Garnet is pseudomorphed and occurs in smaller quantities than in the diatexites, although neosome in metatexites are still garnet-rich. Cordierite often occurs in association with quartz, and its typical fractures that radiate from the borders to the interior of the grain have micas and pinitized yellowish-brown edges as alteration products.

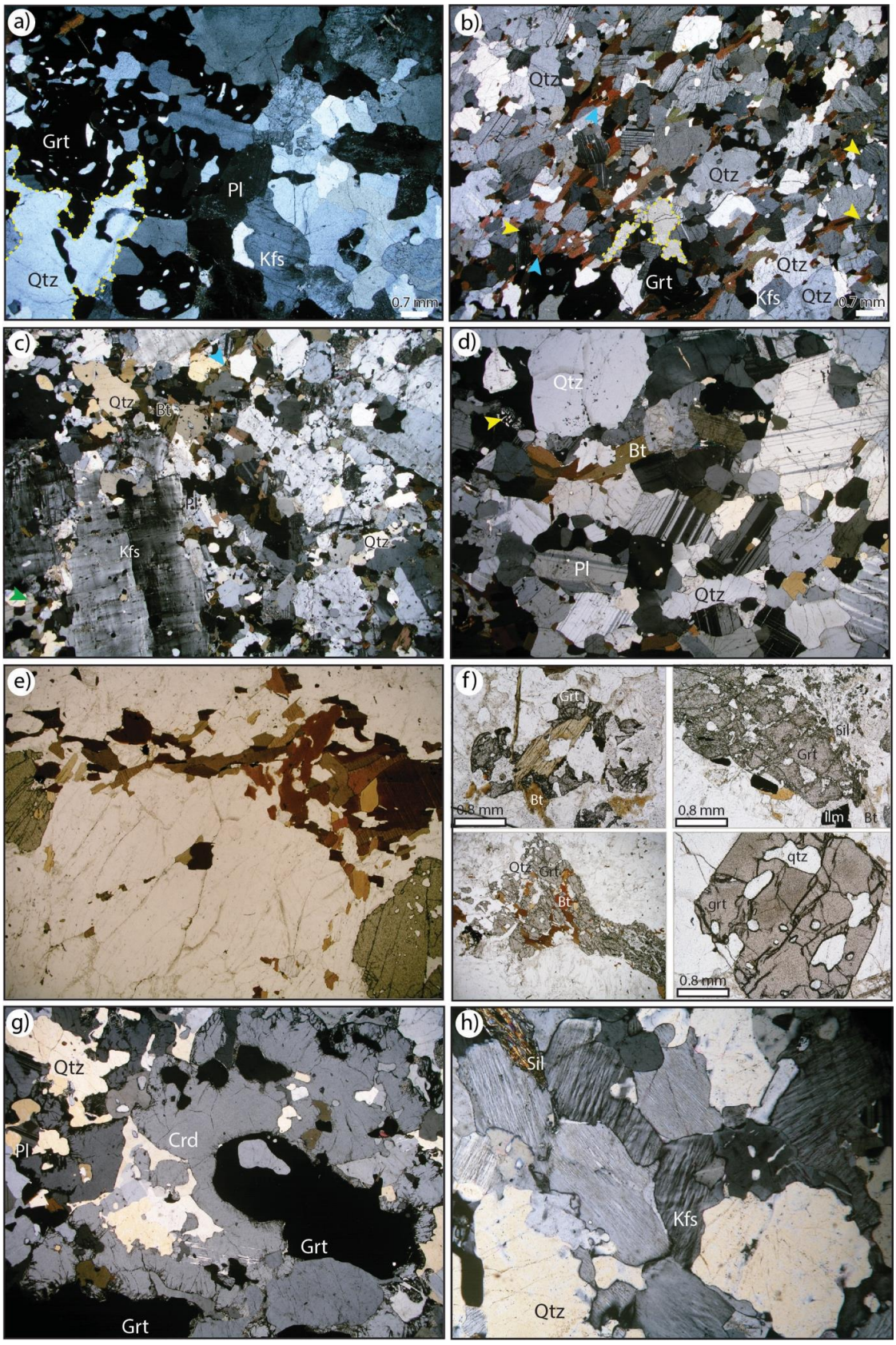
a)
Grt
Pl
Kfs
Qtz
0.7 mm
b)
Qtz
Qtz
Grt
Qtz
Kfs
Qtz
0.7 mm
c)
Qtz
Bt
Pl
Kfs
Qtz
d)
Qtz
Bt
Pl
Qtz
e)
f)
Grt
Bt
0.8 mm
Sil
Grt
0.8 mm
Ilm
Bt
Qtz
Grt
Bt
qtz
grt
0.8 mm
g)
Qtz
Pl
Crd
Grt
Grt
h)
Sil
Kfs
Qtz

Figure 8: Migmatitic textures in CCD. (a) The leucosome portion of the metatexite consisting mainly of garnet, quartz and feldspar; large quartz interstitial free of solid-state deformation occupying embayments in garnet (yellow dashed lines). (b) The melanosome part of metatexite rich in plagioclase and biotite that have corroded grain boundaries (blue arrows); K-feldspar with crystal faces against quartz grains, inferred to be crystallized from the melt; biotite displays strong preferred orientation; quartz interstitial filling spaces between feldspar (yellow dashed lines); deformation twins and undulose exinction in plagioclase (yellow arrows). (c) and (d) Typical microstructures found in the porphyritic granites. (c) Large euhedral and subhedral crystals of alkali-feldspar together with smaller crystals of plagioclase form an open framework in which the interstices are mostly filled by anhedral quartz, small irregularly shaped biotite (blue arrow) and plagioclase (green arrow). (d) plagioclase with simple twining form an open framework with interstitial space filled by large anhedral quartz and biotite, and small myrmekite intergrowth (yellow arrow). (e) Schliere diatexite. The disc-shaped schliere, which surrounds garnet grains, is formed mainly by reddish and dark brown biotite. (f) Garnet porphyroblasts partially replaced by biotite (upper left image), associated with sillimanite, biotite and ilmenite (upper right image), replaced by red biotite-quartz intergrowth (lower left image, which the long edge corresponds to 10.4 mm), and euhedral garnet with quartz bled-like inclusions, likely resulting from melt crystallization (lower right image). All these garnets are observed in diatexite leucosome. (g) Association of garnet and pseudomorphed cordierite in diatexite, with quartz filling the interstices. (h) Spindle-perthitic alkali-feldspar in leucosome of a diatexite, a typical crystallization texture of granitic melt. Long edge of the images (c), (d), (e), (g) and (h) corresponds to 10.4 mm.

Porphyritic granites

744 Porphyritic granites have an assemblage containing Afs + Qtz + Bt + Grt + Pl ± Sil.
745 Accessory phases are apatite, monazite, and hercynite. The main differences between the
746 porphyritic granites and the migmatites are the dominance of typical crystallization textures,
747 the widespread presence of greenish or light brown biotite indicating biotite crystallization from
748 the melt, the lack of biotite schlieren, the large tabular K-feldspar grains, and the dominance of
749 plagioclase without solid-state deformation in the porphyritic granites. Similar to the garnet
750 grains in the leucosomes, garnet in the porphyritic granite occurs both as pseudomorphed and
751 as euhedral grains. Irregularly shaped crystals of quartz, feldspar and biotite are common, as
752 well as euhedral and subhedral feldspar and biotite crystals (Fig. 8c). Plagioclase with simple
753 twining and K-feldspar crystals form a sort of open granular framework in which large anhedral
754 quartz crystals, irregularly shaped biotite and small anhedral plagioclase fill the interstices (Fig.
755 8d). Vermicular intergrowth (myrmekite) of quartz and sodic plagioclase also occur in the
756 interstitial spaces, indicating melt crystallization (e.g., Ashworth and McLellan, 1985). These
757 textures are suggestive of crystallization from melt (e.g., Sawyer 2008), however some
758 association of sillimanite, garnet, and dark reddish biotite forming pseudomorphed
759 agglomerates, suggests that porphyritic granites still have remnants of partial melting residuum
760 (supplementary material).
761
762 *Diatexites/Anatectic granites*
763 The diatexite assemblage consists of abundant Grt + Kfs + Pl + Qtz, and minor Bt + Crd +
764 Sil. Accessory phases are ilmenite, tourmaline, monazite, zircon, rutile and spinel (hercynite).
765 A common feature observed in the diatexites is the schlieren texture, which principally consists
766 of biotite, mostly red-colored, with minor amounts of ilmenite and sillimanite needles. The
767 biotite-rich schlieren together with quartz and feldspar define the magmatic foliation, in which
768 grains are predominantly strain free. These are thin (up to 1.6 mm wide) or disc-shaped

schlieren in which large (~ 1.8 mm long) subhedral biotite crystals with corroded terminations are arranged in an imbricate or tiled pattern (Fig. 8e). Schlieren also have biotite grains with a strong shape-preferred orientation (Figs. 5c in Cavalcante et al., 2013, 2016). Biotite also occurs as randomly oriented flakes. Agglomerates of biotite-alkali feldspar intergrowth often fringe alkali feldspar with well-developed crystal faces in the leucosome. Such faceted alkali feldspar grains are likely the result of melt crystallization (e.g., Vernon and Collins, 1988; Holness et al., 2011).

Garnet grains both in the leucosome and melanosome are mostly porphyroblasts pseudomorphed by biotite and sillimanite (Fig. 8f), and by symplectitic intergrowth of biotite-quartz. Such features are interpreted as a result of incongruent melting reactions, likely involving the breakdown of biotite and sillimanite (e.g., Spear et al., 1999; Waters 2001; Kriegsman and Álvarez-Valero 2010) and melt production between 12-34% during peak metamorphism (e.g., Melo et al., 2017b). Such a percentage of melt production allow for magma flow (crystals suspended in melt) and diatexite formation (e.g., Guernina and Sawyer, 2003). At higher temperature conditions, reactions involving the breakdown of garnet-bearing assemblage may also have occurred to generate spinel (e.g., Douce and Johnston 1991). The garnet-bearing neosomes (melanosome+leucosome) are therefore interpreted as *in situ* melts, with these garnet grains representing peritectic phases. Locally, garnet displays well developed crystal faces, which we interpret to be crystallized from the anatectic melt to form granatiferous leucosomes (Fig. 8f, lower right image). Garnet occasionally contains ilmenite, sillimanite, biotite, spinel and large (up to 1 mm) quartz inclusions, which often form a graphic texture. Anhedral and subhedral garnet occurs in association with large irregularly shaped cordierite grains (Fig. 8g).

Cordierite grains are dominantly anhedral and exhibit yellow-greenish color at their rims. They often occur associated with garnet, biotite and interstitial quartz (supplementary material).

Quartz often exhibits anhedral shapes as occurs as an interstitial phase and occupying embayment in garnet, feldspar and cordierite (Fig. 8g). It has biotite and feldspar inclusions, and often occurs in association with biotite, forming a quartz-biotite intergrowth.

K-feldspar in diatexites often exhibits euhedral shapes and spindle-perthitic exsolution, suggesting that it crystallized from the anatectic melt to form the leucosomes (Fig. 8h). They are large (> 2 to ≥ 10 mm) crystals that commonly present Carlsbad twinning and quartz inclusions.

4.2. Migmatitic rocks from NVC

From eight thin sections from eight localities (Fig. 7) we briefly highlight some textural aspects of the metatexites from the NW-SE body in the northern portion of the CCD (samples #1128, #1292, #1293 and #1296) and the metatexites and transitional metatexite-diatexite southeast of the CCD (samples #949, #1083, #1076 and #1327).

Metatexites from the NW-SE body are mafic rocks composed of Pl + Px (Opx and/or Cpx) + Kfs + Qtz ± Bt ± Sil ± Mag ± Ilm. They have small amounts of interstitial quartz and K-feldspar that show a faint undulose extinction or are free of intracrystalline deformation (Fig. 9a, 9b), interpreted as the former melt. Pyroxene is often pseudomorphed by plagioclase-biotite intergrowth (Fig. 9a). They often occur in association with dark brown sub-anhedral biotite and ilmenite. Trails of sillimanite-biotite are also observed. Plagioclase has sizes ranging from 400 to 1200 μm and is pervasively deformed in the solid-state, as attested by the frequent presence of deformation twins (Figs. 9b, 9c). Myrmekite occurs along feldspar boundaries. Small-bladed biotite defines the foliation at grain-scale in migmatitic granulites (Fig. 9d). Furthermore, biotite-sillimanite aggregates form undulating bands or “pool” of agglomerates that often surrounds feldspar grains (Fig. 9b).

The metatexites and transitional metatexite-diatexite are composed of Kfs + Pl + Qtz + Grt + Bt + Crd + Sil + Ilm ± Opx. Accessory phases are zircon, hercynite, monazite and apatite. Accessory phases are zircon, apatite and monazite. They are coarse-grained rocks with minerals reaching up to 2000 μm in size (Figs. 9e, 9f). Quartz occurs as film along biotite boundaries or as large interstitial grains mainly free of intracrystalline deformation (Fig. 9e), attesting to deformation in the presence of melt. Biotite is brown and red, sub- to euhedral, occurs as inclusion in garnets, forming schlieren in which grains are imbricated, or occurs as isolated grains with strong preferred orientation (Figs. 9e, 9f). They have high content of TiO_2 (see table 3 in Cavalcante et al., 2014), indicating that they likely represent residual biotite, i.e., derived from the residual rocks (e.g., Sawyer, 1998). Sillimanite often occurs in association with cordierite and garnet. Cordierite locally occurs as elongated grains parallel to biotite with preferred orientation (Fig. 9e). Garnet is anhedral, often partially replaced by sillimanite or biotite, and with quartz inclusions. Plagioclase shows limited occurrence of deformation twins. K-feldspar are large grains free of intracrystalline deformation, with mostly subhedral shapes.

4.3. Charnockites and their associated granites

We here describe textural aspects observed in the charnockitic rocks of the Eastern domain and its associated granites, based on 42 thin sections collected in 12 different localities (Fig. 7).

Charnockites

The main mineral assemblage observed in the charnockitic rocks is Afs + Pl + Qtz + Bt + Opx + Ilm ± Grt ± Amp. Accessory phases are zircon, apatite, pyrite, monazite, and allanite. They can be separated into two groups, based on their petrography: charnockite with garnet (the small body and the west portion of the main NE-SW body) and charnockite without garnet (the east portion of the main NE-SW body).

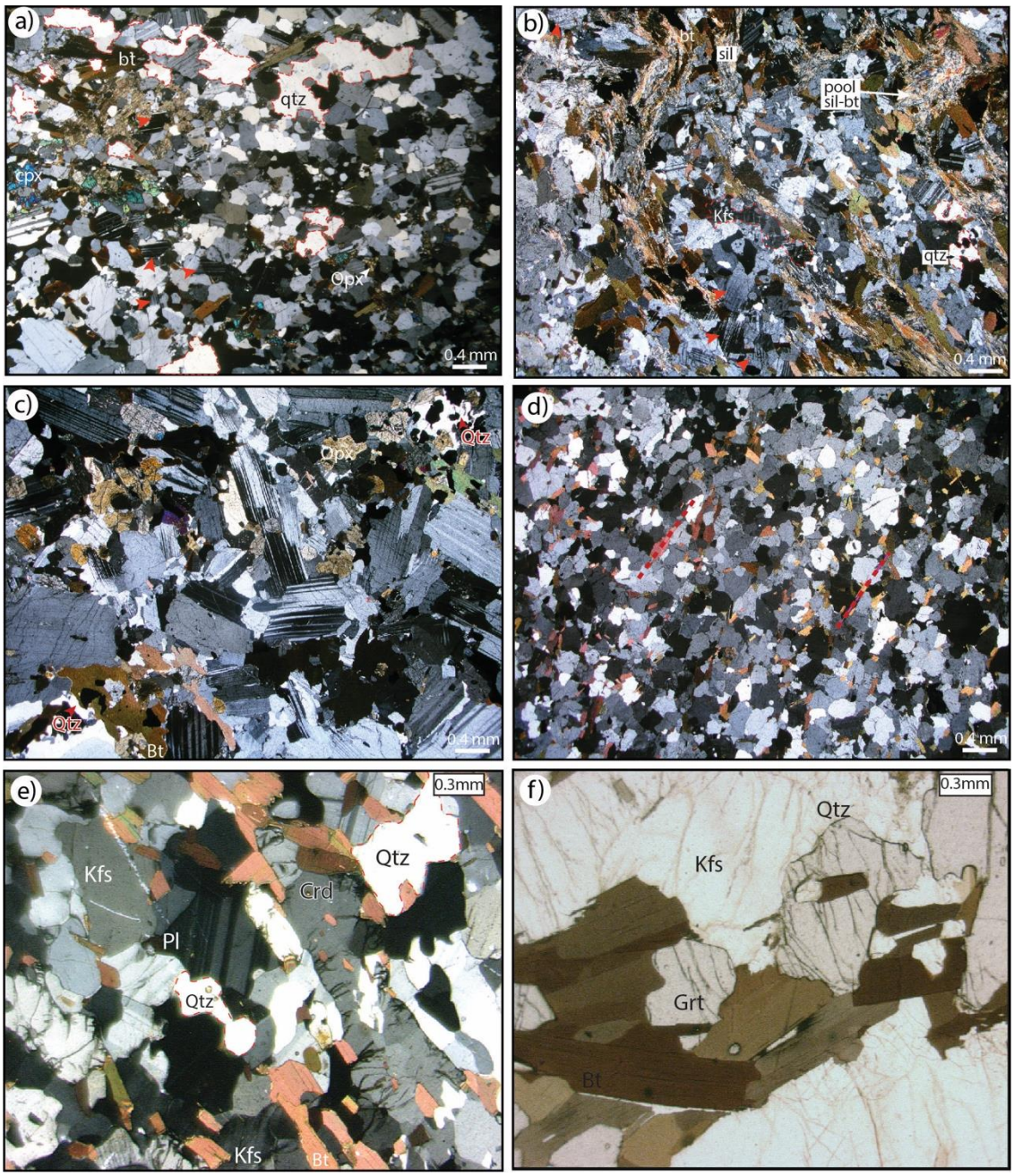

Figure 9: Microscopic aspects of metatexites from the northern portion of CCD (a, b, c, and d) and metatexites southeast of CCD (e and f). (a) Plagioclase with deformation twins (red arrows), small amounts of interstitial quartz (red dashed lines) and pseudomorphed pyroxene. (b) Widespread presence of deformation twins in plagioclase (red arrows), the association of biotite and sillimanite forming an undulating foliation and "pool" of agglomerates, and path of

leucosome formed by interstitial K-feldspar and quartz (dashed red lines). (c) Path of leucosome (interstitial qtz highlighted by red arrow) interpreted as the former melt and widespread deformation twins in plagioclase. (d) Small-bladed biotite with preferred orientation (red dashed lines). (e) Biotite with strong preferred orientation, cordierite elongated parallel to biotite orientation, and interstitial quartz filling spaces between feldspar and between feldspar and biotite (red dashed lines). (f) Irregularly shaped garnets partially replaced by biotite schlieren.

Quartz forms xenomorphic grains that have undulose extinction and subgrain boundaries to some extent (Fig. 10a). Alkali feldspar occurs as both centimetric idiomorphic phenocrystals and as subidiomorphic to xenomorphic in the matrix. Larger grains in the matrix exhibit perthitic exsolution (Fig. 10b). Plagioclase (andesine) occurs as idiomorphic phenocrystals (up to 7 cm) and as a medium to coarse-grained (up to 1 cm) constituent of the matrix. Plagioclase grains often display deformation twins (Figs. 10c, 10d). Antiperthite and myrmekite along grain borders are common features (Fig. 10a). Alteration products are carbonate and sericite for plagioclase and alkali feldspar, respectively.

Orthopyroxene is only found in the matrix forming subidiomorphic to xenomorphic grains with sizes ranging from 1 to 10 mm. It occurs in association with biotite and amphibole or as inclusions in garnet (Fig. 10e) and is often pervasively fractured.

Two different types of biotite are observed, distinguished by means of pleochroism: (i) biotite with green to light yellow pleochroism, rare occurrence. It forms small grains associated with orthopyroxene or as an inclusion in garnet (Fig. 10e); (ii) a biotite with beige to dark brown pleochroism, being more abundant and present in both the main NE-SW body and the small body. This type of biotite also shows kink bands.

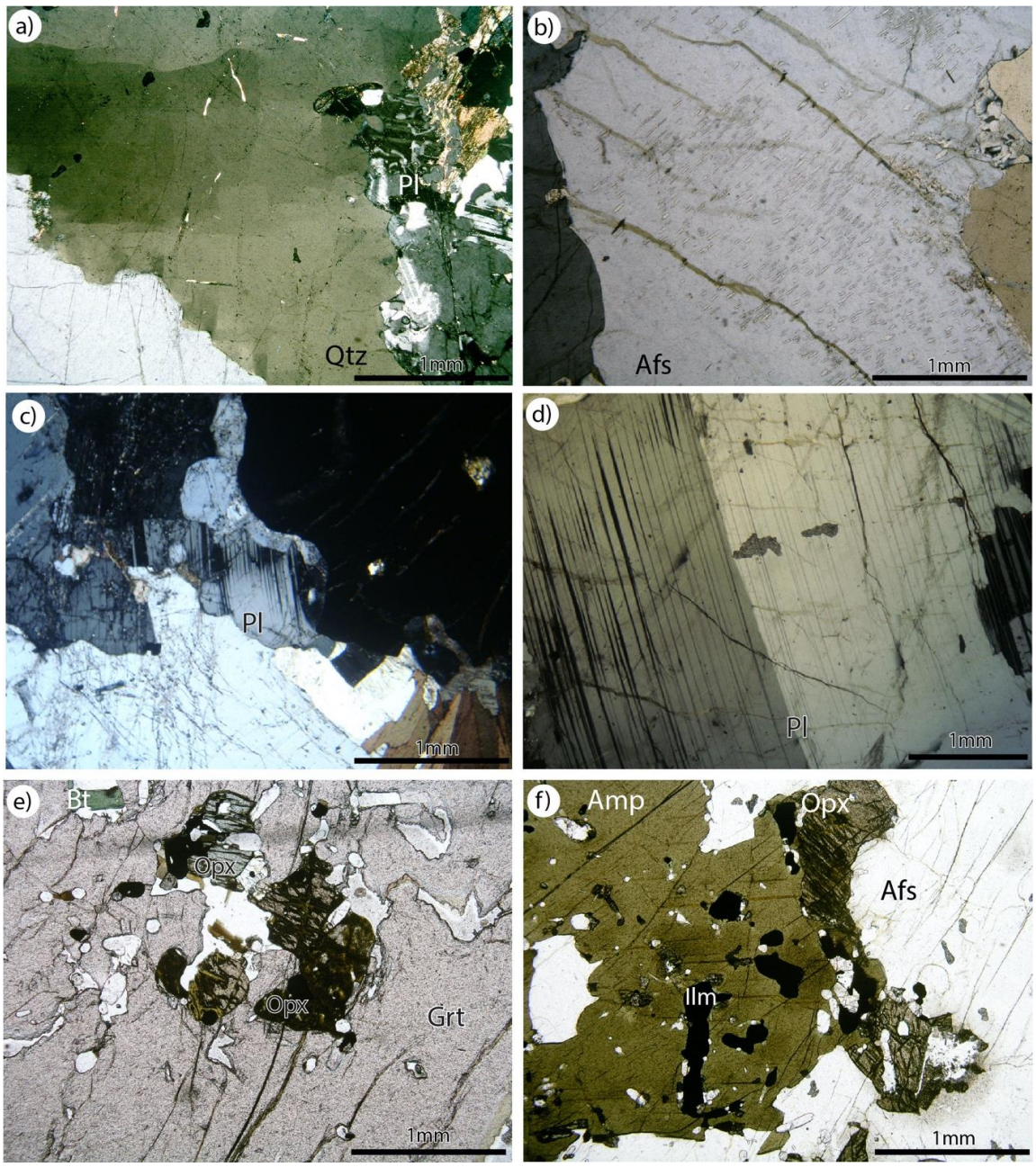

Figure 10: Microscopic aspects of the charnockites. (a) Xenomorphic quartz grain with undulose extinction and chessboard subgrain boundaries, and myrmekite. (b) Perthitic alkali feldspar. (c) and (d) deformation twins in plagioclase. (e) Inclusions of orthopyroxene and biotite in garnet. (f) Relationship between amphibole, ilmenite, and orthopyroxene.

Amphibole (hornblende) is present only in the west portion of the main NE-SW body. It forms xenomorphic grains with sizes ranging from 3 to 8 mm, with olive green to yellowish green pleochroism (Fig. 10f). Generally, this mineral occurs in association with orthopyroxene and ilmenite, with straight to slightly sinuous contacts.

Garnet grains have sizes ranging from 0.5 to 4 cm and idiomorphic to xenomorphic shapes. It is fractured, with little alteration material in its fractures. Inclusions are frequent, among them are apatite, both green and brown biotite crystals, quartz, ilmenite, alkali feldspar, plagioclase, zircon and orthopyroxene (Fig. 10e).

Associated granites

The petrographic analysis also included samples of the granites that are in contact with the Grt-bearing charnockitic rocks (samples #697 and #1231; Fig. 7). Despite the change in color and the lack of orthopyroxene in its mineralogical assemblage, these granites are similar to the charnockites both in terms of mineralogy and texture. The mineralogy of these granites is Qtz +Afs + Pl + Grt + Bt. Accessory minerals are ilmenite, apatite, zircon, monazite, and pyrite. Sericite and carbonate are present as alteration minerals.

Quartz forms coarse xenomorphic grains with undulose extinction, and sub-grain domains being formed locally. Alkali feldspar can be idiomorphic or phenocryst; when present in the matrix it is subidiomorphic and medium to coarse grained. Larger grains display perthitic exsolution. Plagioclase is the mineral that is most altered in these granites and was determined optically to be an oligoclase (An_{25}). It is only present in the rock matrix as subidiomorphic grains of medium to coarse size, and it is common to observe straight contacts of this mineral with other minerals in the matrix. Antiperthites are not present.

The garnet is subidiomorphic to xenomorphic, very fractured, and the grain size can reach up to 7 mm. It has a diverse range of inclusions, such as quartz, apatite, biotite, and ilmenite.

Biotite is the only mineral that differs optically depending on whether the granite is from an abrupt or a gradational contact; in the granite from the abrupt contact, it has yellow to dark brown pleochroism and is present as grains of medium to coarse size, idiomorphic to xenomorphic, generally associated with garnet. In the gray-orange granite (transitional contact), biotite has greenish colors, with edges of yellow to light brown pleochroism and inclusions of allanite.

5. Bulk-rock geochemical data

From the rock units described in detail above, 39 samples were selected for geochemical studies, including 23 samples from CCD (migmatitic rocks), one sample from the NVC and 15 samples from intrusive late charnockites and their associated granites (see Fig. 4 for sample locations; Tables 2 and 3 in the supplementary material).

We collected approximately 10-15 kg for each sample to ensure the representativeness of the bulk rock chemistry of these very coarse-grained rocks. Any stains from markers were polished and all surfaces where any evidence of rock alteration observed were eliminated with a saw. The samples were crushed to a fraction <300 mesh. Approximately 20 grams of homogenized powder were sent to ACME Analytical Laboratories (Vancouver, Canada) for major and trace element analysis. Major elements were measured by total fusion of approximately 200 mg of sample with lithium metaborate / tetraborate, dissolved with diluted nitric acid, and measured by emission spectrometry (ICP-ES). The LOI (loss on ignition) was calculated as the difference between the weight of the sample before and after heating to 1000 ^{o}C. For trace element determination, 200 mg of sample was totally fused with lithium metaborate / tetraborate and dissolved with nitric acid, and then measured by inductively coupled plasma mass spectrometry (ICP-MS).

The geochemical data were treated with IGPETOOLS software developed by F. Bea (downloadable from www.ugr.es/~fbea) using STATA^{TM} programming language.

968

969 ***5.1. Bulk-rock geochemical data from the migmatitic rocks (CCD and NVC)***

970 Representative samples from the CCD selected for geochemical analysis (Table 2) include
971 one residuum-rich diatexite (sample #535A), three porphyritic granites (samples #1167, #1179,
972 #1184), and nineteen diatexites/anatectic granites (samples #09AR10, #09AR13, #455A,
973 #535B, #536, #664, #952, #1113, #1171, #1172, #1178, #1183, #1185, #1217, #1223, #1224,
974 #1230, #1232, #1233). One sample of metatexite (#950) from the NVC was also analyzed. Data
975 compilation available on Gradim et al. (2014) was also used to compound our geochemical
976 analysis. The compiled data were grouped into residuum-rich metatexite (crd granulites of
977 Gradim et al., 2014); undifferentiated metatexite, including the migmatitic paragneisses from
978 the NVC; Ataléia Granite; "G3" granite; and undifferentiated Carlos Chagas (CC) granite, in
979 order to compare the database from Gradim et al. (2014) with the data presented in this study,
980 allowing the overall discussion regarding their petrogenetic processes.

981 All analyzed samples are peraluminous (ASI index varying from 1.03 to 1.33) and the SiO_2
982 content varies from 61.75 to 76.62 wt.% (Fig. 11a). The residuum-rich diatexite has the lowest
983 silica content (61.75 wt.%), followed by the porphyritic granites (66.2-69.73 wt.%). Diatexites
984 and anatectic granites range in silica content from 69.73 to 76.62 wt.% (Fig. 11a, Table 2). A
985 large range of ASI values are shown by metatexites, varying from slightly metaluminous to
986 highly peraluminous (up to 4.39) (Fig. 11a).

987 The binary plot of FeO_t+MgO versus SiO_2 shows a well-defined negative correlation
988 between residuum and anatectic melts, with residuum-rich migmatites being concentrated
989 towards the high FeO_t+MgO and low SiO_2 values, granites and diatexites showing lower
990 FeO_t+MgO and higher SiO_2 contents, and metatexitic samples in an intermediate position (Fig.
991 11b). Samples from porphyritic granites (this study) and Ataléia and "G3" granites show an

almost orthogonal deviation from the residuum-anatectic melt trend, towards plagioclase compositions (residual Pl-An35 and melt-product Pl-An25) (Fig. 11b).

Other major element binary plots highlight the control of residual and melt-product phases on the chemical variability of both metatexites and diatexites/anatectic granites (Figs. 11c-f). Residuum phases, such as biotite, garnet, cordierite and plagioclase (An35), strongly control the bulk composition of residuum-rich and undifferentiated metatexites, porphyritic granites, and Ataléia and "G3" granites (Figs. 11c, f). The influence of melt-product phases on the composition of diatexites/anatectic granites, including biotite, K-feldspar, plagioclase (An25) and quartz, is shown in the Figures 11c-f, mostly controlled by the proportions of K-feldspar, plagioclase and quartz. The porphyritic granite samples and Ataléia and "G3" granites tend to K-feldspar and plagioclase (An25) compositions in comparison to the diatexites/anatectic granites (Figs. 11d, e).

FeO_t+MgO was used as a differentiation index based on the relationship with SiO_2 contents (Fig. 11a) and different trace elements were plotted as a function of this index (Fig. 12). These plots show consistent positive correlation of this differentiation index with Ba, Sr, Zr, P_2O_5, LREEt and HREEt, and Th (Figs. 12a, b, d-g, i), and negative correlation with Rb and U (Figs. 12c, h) for porphyritic granites and diatexites/anatectic granites. A positive correlation between Ba and Sr (Figs. 12a, b) can be associated with fractionation of biotite and plagioclase, respectively, in more differentiated anatectic magmas, while the Rb poorly constrained negative correlation (Fig. 12c) suggests K-feldspar accumulation in more differentiated magmas. The samples from porphyritic granites follow the general differentiation trends delineated by the diatexites/anatectic granites in these plots, but two of three samples are out of the trend in the Rb plot, showing high Rb values (>250 ppm).

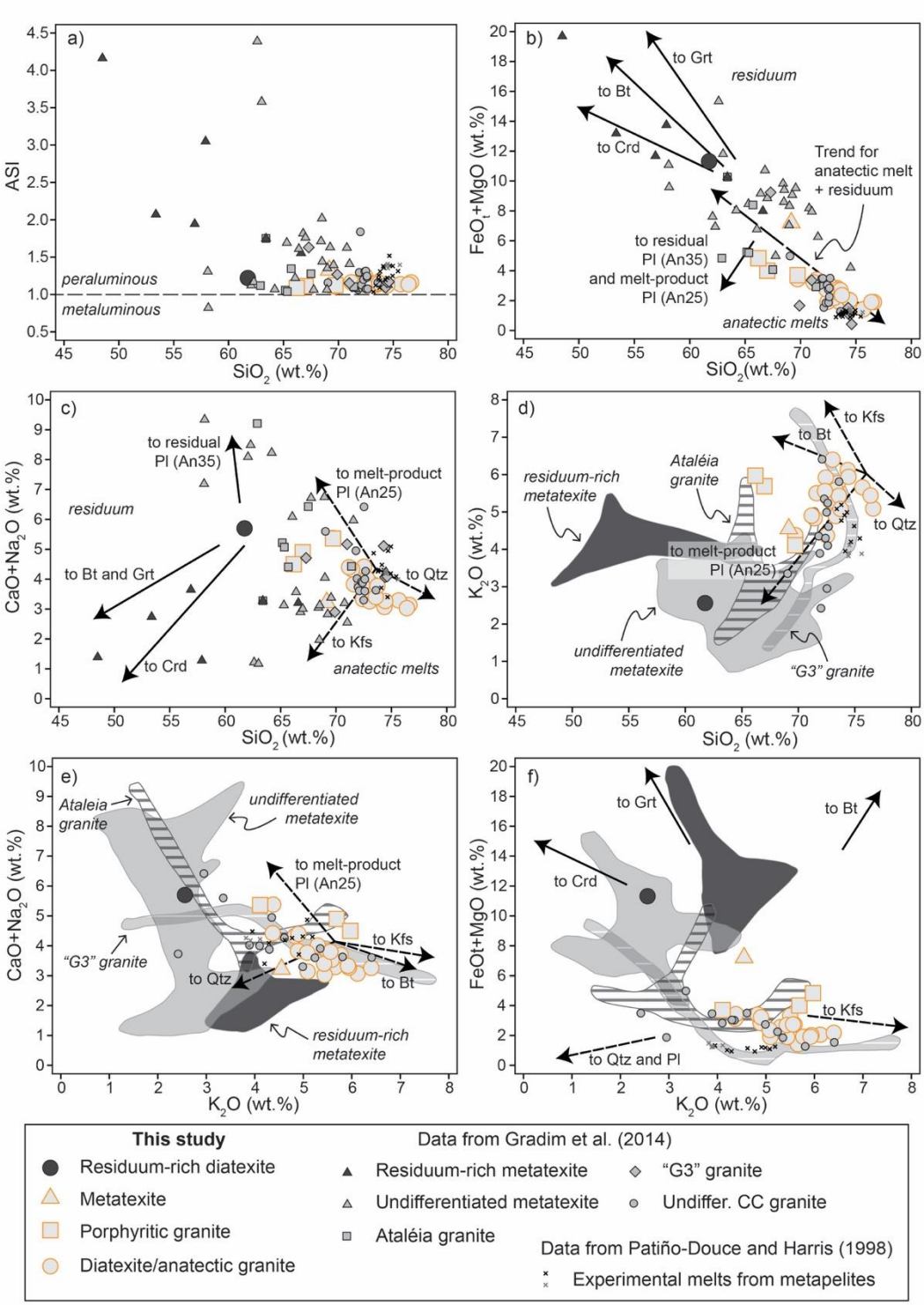

Figure 11: Bivariate major elements plots (all oxides in wt. %) for migmatitic rocks from the Anatectic domain, Araçuaí belt, including data compiled from Gradim et al. (2014) and this study. (a) Aluminium saturation index (ASI) vs. SiO_2, where ASI = Al/(Ca-1.67*P+Na+K), Frost et al. (2001); (b) FeOt+MgO vs. SiO_2; (c) $CaO+Na_2O$ vs. SiO_2; (d) K_2O vs. SiO_2; (e)

CaO+Na_2O vs. K_2O; (f) FeOt+MgO vs. K_2O. Data from this study are represented by larger symbols. Experimental melts from metapelites (Patiño Douce and Harris, 1998) are also plotted for comparison. Arrows represent mineral fractionation trends. Dark and light gray fields in (d), (e) and (f) represent residuum-rich metatexite and undifferentiated metatexite; fields with black and gray stripes represent Ataléia and "G3" granites (Gradim et al., 2014).

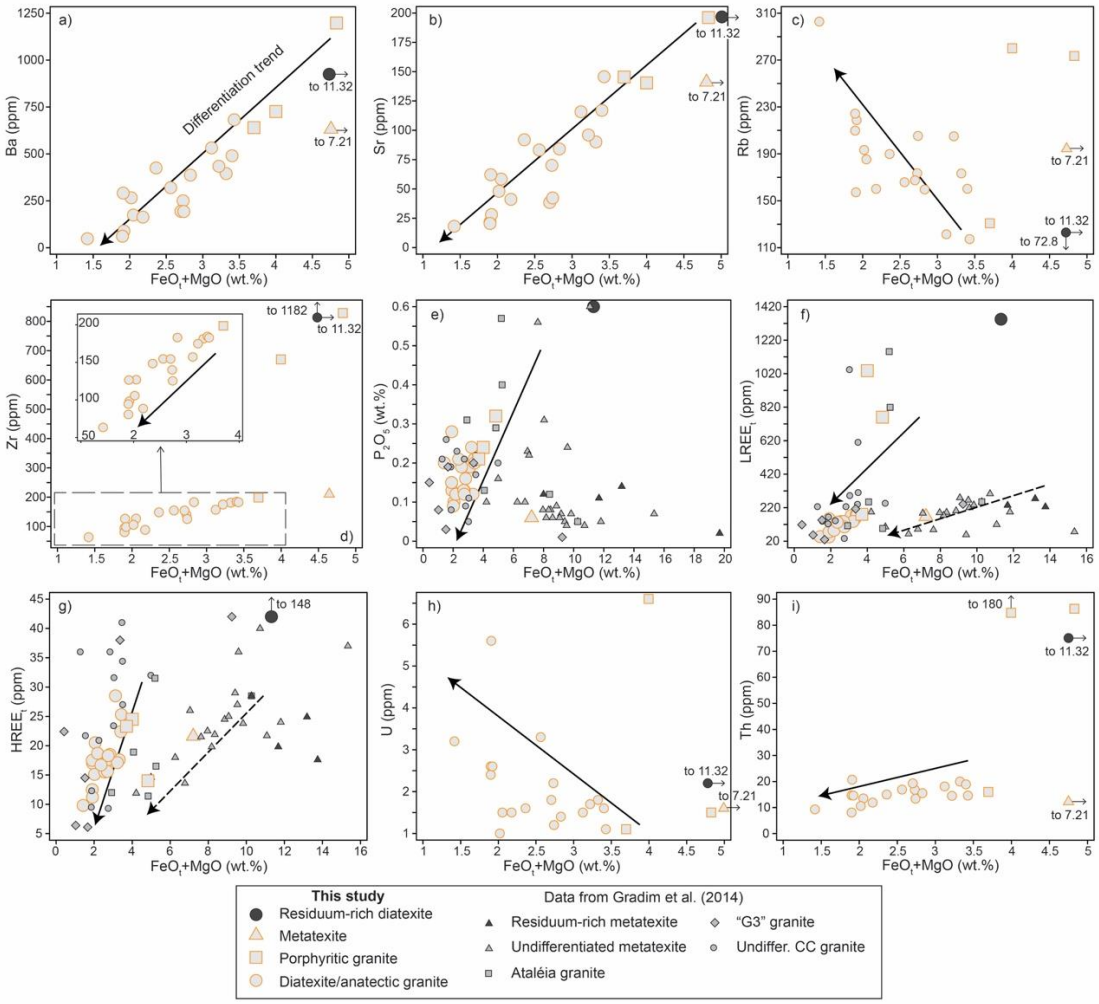

Figure 12: Bivariate trace elements plots (trace elements in ppm, except P_2O_5 in wt. %) vs. FeOt+MgO (wt. %), used as a differentiation index, for migmatitic rocks and granitoids from the Anatectic domain, Araçuaí belt. a) Ba; b) Sr; c) Rb; d) Zr; e) P_2O_5; f) LREEt; g) HREEt; h) U; i) Th. Arrows represent magmatic differentiation trends. Compilation data from Gradim et

al. (2014) provide only P_2O_5 and REE values. Two differentiation trends are observed in total REE values, a flatter trend comprising the metatexitic samples (dashed arrow) and a steeper one including porphyritic granite and diatexite/anatectic granites from CCD, and Ataleia and "G3"granites.

The concentration of Zr, P_2O_5, $LREE_t$, $HREE_t$, U and Th in bulk rock composition can trace the behavior of accessory minerals, such as monazite and zircon, in melt mobilization and fractionation (Bea, 1996). The residuum-rich diatexite (1,182 ppm) and porphyritic granites (199-828 ppm) have high Zr contents (Fig. 12d), suggesting higher proportions of zircon. The diatexites/anatectic granites define a well-constrained positive correlation between Zr and FeO_t+MgO (Fig. 12d), with Zr contents varying from 63 to 185 ppm in the most and least differentiated samples, respectively (#1223 and #1178) (Table 2). P_2O_5 and $LREE_t$ contents show high values (>0.25 wt.% P_2O_5 and >420 ppm $LREE_t$) for the residuum-rich diatexite, porphyritic granites and Ataléia granites (Figs. 12e, f), suggesting higher proportions of monazite and/or apatite in these rocks. The diatexites/anatectic granites display a well-defined positive correlation of $LREE_t$ with FeO_t+MgO, showing lower values for the most differentiated samples (Fig. 12f). The metatexites display a general low value of $LREE_t$ (58-303 ppm), in the same range of the diatexites/anatectic granites but show a flatter positive trend connecting the residuum-rich metatexites and the samples with lower FeOt+MgO values (Fig. 12f).

Concentrations of $HREE_t$ also show two trends of positive correlations with FeOt+MgO, one least defined trend for metatexites and another steeper trend including porphyritic granites and diatexites/anatectic granites (Fig. 12g). An ill-defined negative correlation is displayed between U and FeO_t+MgO with most samples yielding < 2.5 ppm of U (Fig. 12h). Higher Th contents are observed in two samples of porphyritic granites and in the residuum-rich diatexite

(>70 ppm), as well as a well-defined positive correlation from porphyritic granites with lowest FeOt+MgO values to diatexites/anatectic granites (Fig. 12i).

Normalized multi-element diagrams were plotted for samples analyzed in this study and the compiled data (Fig. 13). The chondrite-normalized spidergram for metatexites shows a flat to weakly depleted HREE pattern (La/Yb_N=1.6-13.8) and negative to weakly positive Eu anomalies (Eu/Eu*=0.3-1.2) (Fig. 13a; Table 2). The residuum-rich diatexite is the most enriched sample in REE (SumREE=1496 ppm) (Table 2) and displays a weakly depleted HREE pattern (La/Yb_N=9.8) and a strongly negative Eu anomaly (Eu/Eu*=0.2) (Fig. 13a; Table 2). The porphyritic granites are enriched in LREE in comparison with the metatexites and show strongly depleted HREE pattern (La/Yb_N=167.6-185.2), however one sample (#1184) has similar REE pattern than the metatexite sample (NVC, #950) analyzed in this study (Fig. 13a). The porphyritic granites display strongly to moderately negative Eu anomaly (Eu/Eu*=0.2-0.6) (Fig. 13a; Table 2). The compiled data from Ataléia and "G3" granites show a broad variability in REE contents (Fig. 13a), but Ataléia granites display more pronounced depleted HREE patterns (La/Yb_N=9.8-128.4) than the "G3" granites (La/Yb_N=2.7-22.4). Marked differences in Eu anomaly were found between the Ataléia and "G3" granites (Eu/Eu*=0.2-2.0 and 0.3-2.1, respectively). The diatexites/anatectic granites show a general weakly depleted HREE pattern (La/Yb_N=2.9-10.3), with three samples displaying more depleted values (La/Yb_N>14 - #455A, #952 and #1172), and strongly to moderately negative Eu anomalies (Eu/Eu*=0.1-0.7) (Fig. 13b; Table 2). Except for Eu values, HREE and LREE values from the diatexites/anatectic granites are similar to the data from metatexites (Fig. 13b). The compiled data for undifferentiated Carlos Chagas granites show a broader REE pattern variability, with some samples yielding highly fractionated magmas (La/Yb_N up to 184.8) but the values of Eu anomaly are consistently negative (Eu/Eu*=0.3-0.8) and agree with the data obtained in this study.

The silicate Earth-normalized spidergram for trace elements also shows a general tendency of trace elements enrichment for residuum-rich diatexite and porphyritic granites in comparison with metatexite and diatexites/anatectic granites (Fig. 13c).

5.2. Bulk-rock geochemical data from the charnockites and associated granites

Twelve (12) charnockite samples and three (3) associated granites (#697A, #697B, and #1231A) were selected and analyzed for major and trace elements in this study (Table 3 in the supplementary material). These analyses were combined with a vast and complete database for the early Cambrian magmatism in the Araçuaí belt, available in Araujo et al. (2020). The data from the compiled database comprise charnockitic rocks, including charnockites, charnoenderbites, and mangerites; and granitoids, including granites, granodiorites, and tonalites. Mafic and intermediate rocks also available in this compilation were not included in our evaluation.

The charnockites and associated granites analyzed in this study have SiO_2 contents ranging from 60.55 to 67.92 wt.% and plot in the monzonite, syenite, and granite fields of the alkaline series (shoshonitic series) in the TAS diagram (Fig. 14a). The compiled data display an expanded alkaline shoshonitic series that include the analyzed samples, and also an expanded subalkaline series (Fig. 14a).

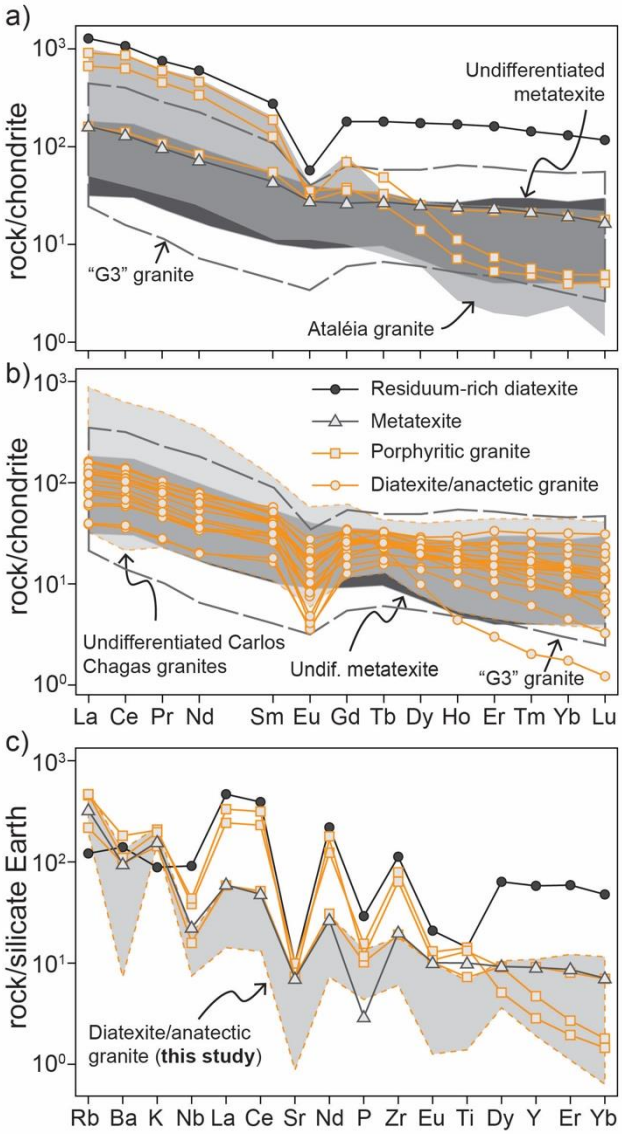

Figure 13: Chondrite-normalized REE (a, b) and silicate Earth-normalized trace elements spidergrams (c) of migmatitic rocks and related granitoids from CCD. Normalization values of McDonough and Sun (1995). Residuum-rich diatexite and two samples of porphyritic granite are enriched in LREE, but the porphyritic granites show depletion in HREE (a). The third porphyritic granite sample shows similar REE pattern to the metatexite analyzed in this study (a). The variations in HREE patterns in (b) must be related to the different proportions of garnet in these samples.

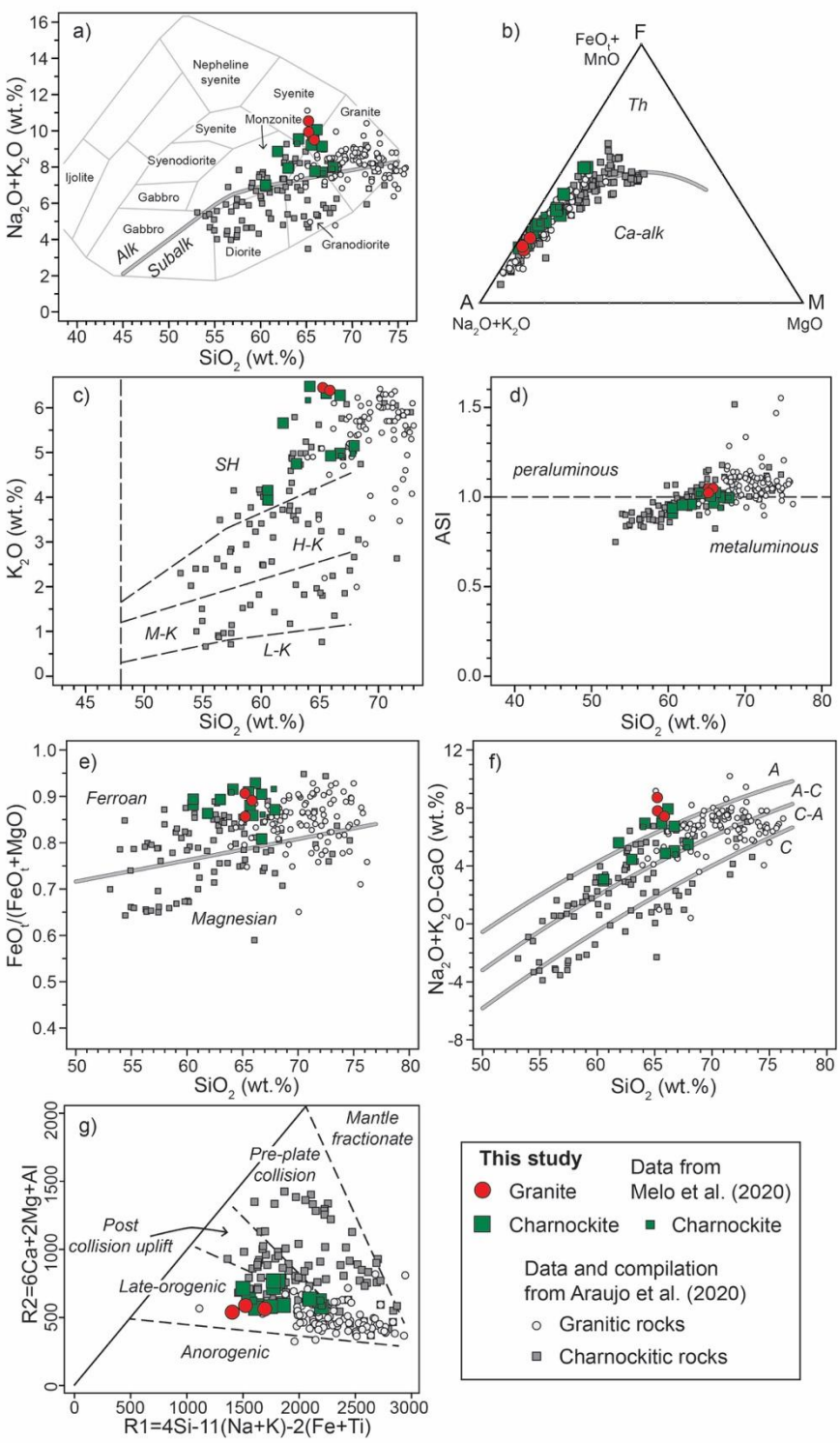

Figure 14: Whole rock composition of late orogenic charnockitic rocks and associated granites from the Araçuaí belt, including samples analyzed in this study and data compilation from Melo et al. (2020) and Araujo et al. (2020). (a) Total alkalis vs. SiO_2 (TAS) diagram, Cox et al. (1979) modified by Wilson (1989); (b) AFM diagram, showing the fields of tholeiitic (Th) and calc-

alkaline (Ca-alk) magmatic series, Irvine and Baragar (1971); (c) K_2O vs. SiO_2 diagram, Peccerillo and Taylor (1976). L-K: tholeiitic series; M-K: calc-alkaline series; H-K: high-K clac alkaline series; SH: shoshonite series; (d) Aluminum saturation index (ASI) vs. SiO_2 (wt. %) diagram, Frost et al. (2001); (e) Fe-number vs. SiO_2 diagram, Frost et al. (2001) (Fe-number=FeOt/(FeOt+MgO)); (f) MALI vs. SiO_2 diagram, Frost et al. (2001) (MALI=Na2O+K2O-CaO). A: alkalic; A-C: alkali-calcic; C-A: calc-alkalic; C: calcic; and (g) R1-R2 tectonic discriminant diagram, Batchelor and Bowden (1985). R1=4*Si-11*(Na+K)-2*(Fe+Ti); R2=6*Ca+2*Mg+Al.

In the AFM diagram, most samples show a non-tholeiitic series trend, although a few samples show Fe enrichment in less differentiated rocks pointing to tholeiitic series magmas (Fig. 14b). In terms of potassium contents, most samples display a shoshonitic trend, including the charnockites and granites analyzed in this study, but high-K and medium-K calk-alkaline series and/or medium to low-K tholeiitic series also occur (Fig. 14c). A generally positive correlation between ASI (aluminum saturation index) and SiO_2 contents shows a metaluminous to slightly peraluminous signature for these acid rocks (Fig. 14d), similar to the signatures found in the samples from this study. The analyzed samples show metaluminous to slightly peraluminous compositions (ASI=0.91-1.05) (Fig. 14d; Table 3). In the classification scheme by Frost et al. (2001), most samples plot in the ferroan alkali-calcic field, but magnesian rocks and alkalic, calc-alkalic and calcic rocks also occur within the Araçuaí belt (Figs. 14e, f). The charnockites and associated granites presented in this study plot in the ferroan alkalic and alkali-calcic fields and do not show as much variability as the samples from the literature (Figs. 14e, f). The R1-R2 tectonic discriminant diagram of Batchelor and Bowden (1985) also highlights the diversity of magma composition of the early Cambrian magmatism in the Araçuaí belt (Fig. 14g). These rocks define granitoid associations in the pre-plate collision, post collision uplift,

and late-orogenic fields, but most samples plot in the post-collision uplift and late-orogenic fields (Fig. 14g).

Based on trace element contents, most samples can be classified as A-type granitoids (high contents of HFSE), but numerous samples show chemical characteristics of I- and S-type granitoids (Whalen et al., 1987) (Figs. 15a, b). In the diagram proposed by Eby (1992), the A-type granitoids plot around the boundary between the A1 and A2 fields, but most samples tend to plot within the A2 field (Fig. 15c). Trace element ratios associated with Nb-anomaly signatures (Th/Nb, La/Nb and Th/La) show low values for most samples (Th/Nb<0.5 and Th/La<0.2) (Figs. 15d, e), suggesting sources with mantle to lower crust chemical affinities (Plank, 2005). However, higher Th/Nb and Th/La values (more than 1.5 and 0.5, respectively) in the charnockitic and granitic rocks, including those from this study (#696, #697B, #1227, #1231A, 1231B, 1249; Figs. 15d, e), point to a crustal contribution to these rocks (Plank, 2005). Source discriminant diagrams for A-type granitoids using silicate Earth-normalized Th/Nb, Th/Ta, Ce/Pb and Y/Nb ratios (Moreno et al., 2014) show ocean island magmatic affinities for most charnockitic rocks, but the more differentiated samples tend to plot in the continental crust and arc-related fields (Figs. 15f-h).

Chondrite-normalized REE spidergram for all samples shows a consistent enriched LREE pattern in comparison with HREE and negative to slightly positive Eu anomaly (Fig. 15i). The granitic rocks show higher LREE-HREE fractionation (La/Yb_N mostly >200 and up to 1417) and mostly negative Eu anomaly. The charnockites analyzed in this study show moderately enriched LREE pattern (La/YbN=10-39) and negative to positive Eu anomaly (Eu/Eu*=0.31-1.66), comparable with the patterns seen in the associated granites (La/YbN=29-32 and Eu/Eu*=1.06-1.25) and in the data from the literature (Fig. 15i; Table 3). The Silicate Earth-normalized trace element spidergram shows LILE and LREE enrichment and positive anomaly

of Zr (Fig. 15j). Overall, the charnockites and granites are enriched in trace elements in comparison to the diatexites and anatectic granites (Fig. 15j).

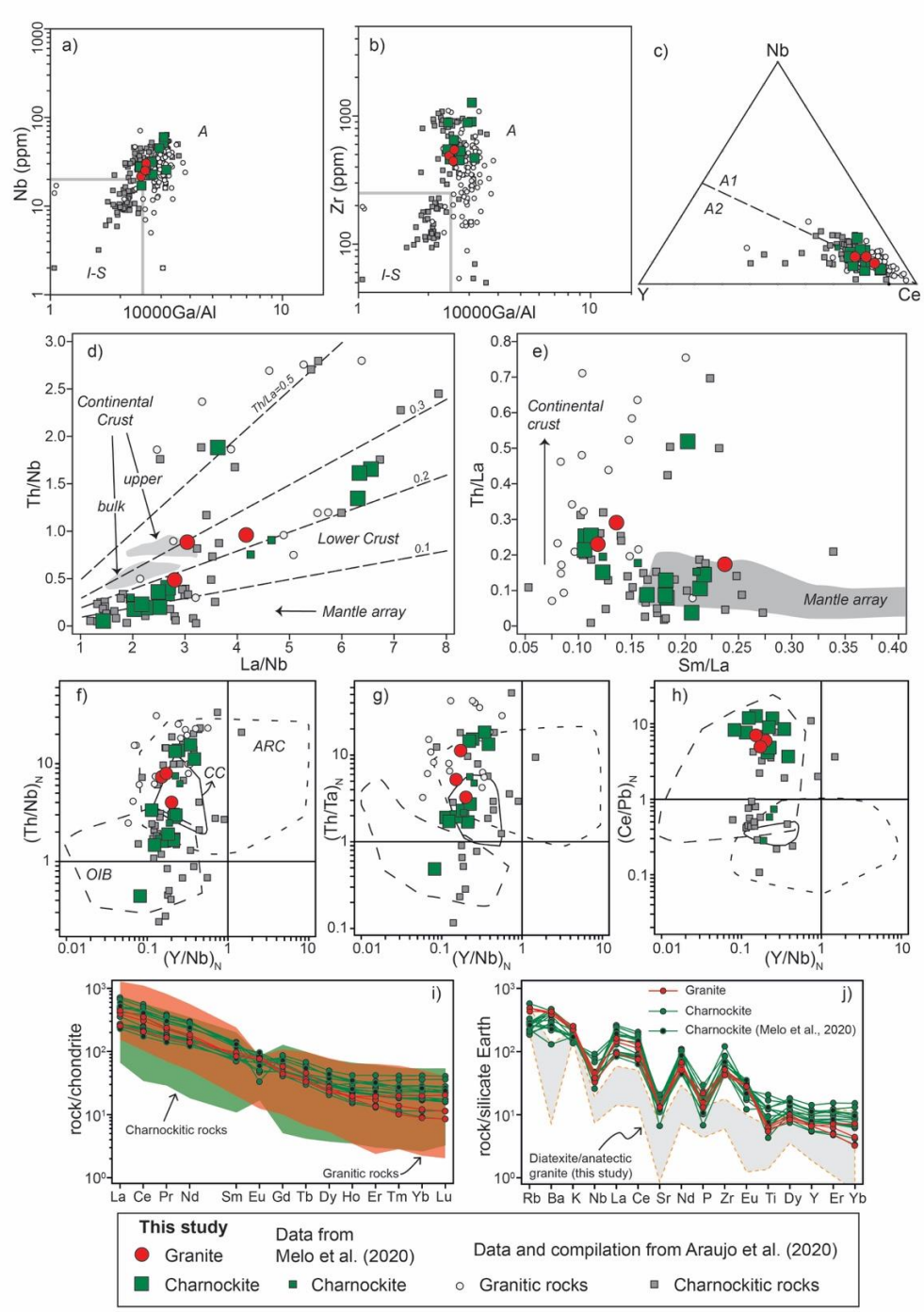

Figure 15: Trace element-based discriminant diagrams of late orogenic charnockitic rocks and associated granites from the Araçuaí belt, including samples analyzed in this study and data

compilation from Melo et al. (2020) and Araujo et al. (2020). Nb (a) and Zr (b) vs. 10000 Ga/Al diagrams for I-, S-, and A-type granitoids, Whalen et al. (1987); (c) Triangular diagram (Nb-Y-Ce) for A1 and A2-type granitoids discrimination, Eby (1992); (d–e) Th/La ratio source discriminant diagrams, Plank (2005); (f–h) Magmatic source discriminant diagrams, Moreno et al. (2014). OIB: ocean island rocks; CC: continental crust estimates; ARC: convergent margin rocks. Values normalized to the silicate Earth of McDonough and Sun (1995); Chondrite-normalized REE (i) and silicate Earth-normalized trace elements (j) spidergrams (values from McDonough and Sun, 1995). Compiled data from Araujo et al. (2020) is shown in (i) as green (charnockitic rocks) and red (granites) fields. In (j) a gray field represents diatexite/anatectic granite samples (this study).

6. Discussion

6.1. Migmatite evolution and the generation of the Carlos Chagas anatexites

Migmatitic rocks are widespread in the Eastern domain of the Araçuaí belt, including metatexites and transitional metatexite-diatexite from the NVC, metatexites and diatexites/anatectic granites from the CCD, and related peraluminous granites (the so-called Ataléia Suite and "G3" leucogranites by, for example, Pedrosa-Soares et al., 2011 and Gradim et al., 2014). Gradim et al. (2014) highlight the genetic link between the crustal source rocks (NVC) and the peraluminous magmatism, based essentially on field relationships and bulk rock geochemistry, including major element and REE patterns. This geochemical database shows close compositional links between the paragneisses from NVC and the so-called Ataléia Suite, but more differentiated rocks from Ataléia Suite display similar compositions to the most fractionated Carlos Chagas anatexites (Gradim et al., 2014). The so-called "G3" leucogranites are described as K-feldspar-rich leucosomes and show highly fractionated magmas, similar to Carlos Chagas rocks, but less evolved magmas are also observed (Gradim et al., 2014).

In this study we have added bulk rock composition of 23 samples to the database of Gradim et al. (2014), mostly from diatexites and anatectic granites outcropping in the CCD. The diatexite/anatectic granite association (or anatexites) displays diffuse contacts and close spatial relationship with metatexites (Fig. 4), suggesting an in-source derivation for these rocks (i.e., they formed within the migmatitic area). Anatectic granites associated with migmatites often exhibit schlieren and residuum-like features, unlike granites that form alochthonous intrusions (e.g., Didier, 1973). Therefore, we interpret the anatexites as parautochthonous rocks (e.g., Sawyer, 1998), i.e., rocks of local derivation.

The residuum-rich diatexite (#535A) and the porphyritic granites (#1167, #1179 and #1184) represent the chemically least evolved samples in our database, based essentially on geochemical differentiation indexes, such as SiO_2 and FeO_t+MgO (Figs. 11 and 12), and are likely associated, respectively, with the metatexitic samples and the Ataléia Suite (Gradim et al., 2014; Figs. 11, 12 and 13). As pointed out by Gradim et al. (2014), the Ataléia Suite, and therefore the porphyritic granites of this study, likely represent residuum-rich magmas indicating non-efficient melt migration from their source that were capable of forming isolated granitic intrusions. Such inefficient melt migration is also supported by microscopic evidence of residual material in the porphyritic granites (supplementary material). Fractionation of melt-product plagioclase might be another important petrogenetic process that could account for the chemical variability of the Ataléia Suite/Porphyritic granites (Figs. 11b-f).

The observation of widespread partial melting features in the NVC (e.g., Gradim et al., 2014, Richter et al., 2016; Figs. 4 and 6a-d) suggests pervasive partial melting of a large portion (>150 km long and >100 km wide) of the Araçuaí orogenic middle crust (Fig. 16a). The chemical variability of the migmatitic rocks from NVC and CCD (Figs. 11 and 12) indicates processes of filtering of residuum (Wolfram et al., 2017) that results in residuum-rich metatexites and residuum-poor diatexites/anatectic granites, with the latter representing the

most efficient melt extraction from the source. However, field and AMS mapping suggest non-efficient vertical melt migration of these extracted magmas upwards from the CCD crustal level (Cavalcante et al., 2013 and this study). Differently from what was observed in the Famatinian migmatites from NW Argentina (Wolfram et al. (2017), the compositional variability of migmatites and anatectic granites in the CCD does not show a simple trend of filtering of residuum from residual migmatites to leucogranites (compare Fig. 11f from this study with Fig. 11 from Wolfram et al., 2017). Instead, the metatexites and less differentiated granites (Ataléia Suite and porphyritic granites) gradually evolve to the diatexites/anatectic granites (Figs. 11a, f). This might be associated with an overall less efficient melt migration in the Eastern domain of the Araçuaí belt. The melt extraction from metatexites (NVC) to form the porphyritic granites (Ataléia Suite) might be compared to the restite unmixing model of White and Chapell (1977), corresponding to inefficient separation of melt from residuum due to *en masse* flow (Brown, 1973; Sawyer, 1994) that evolved to become the Carlos Chagas anatexites.

Melt fractionation within the Carlos Chagas anatexites is suggested by the differentiation trends shown in major element, such as K_2O (Fig. 11f), and trace element binary diagrams (Fig. 12). These differentiation trends are well defined by Ba, Sr, Zr, P_2O_5 and LREE (Figs. 12a, b, d-f) and suggest crystal fractionation controlled by early crystallization and accumulation of biotite, plagioclase, zircon and monazite/apatite. The differentiation trend within the Carlos Chagas anatexites can tentatively be correlated with the subhorizontal crustal flow towards N-NW (Fig. 16b), as proposed by Cavalcante et al. (2013), but further specific sampling must be performed to test this hypothesis.

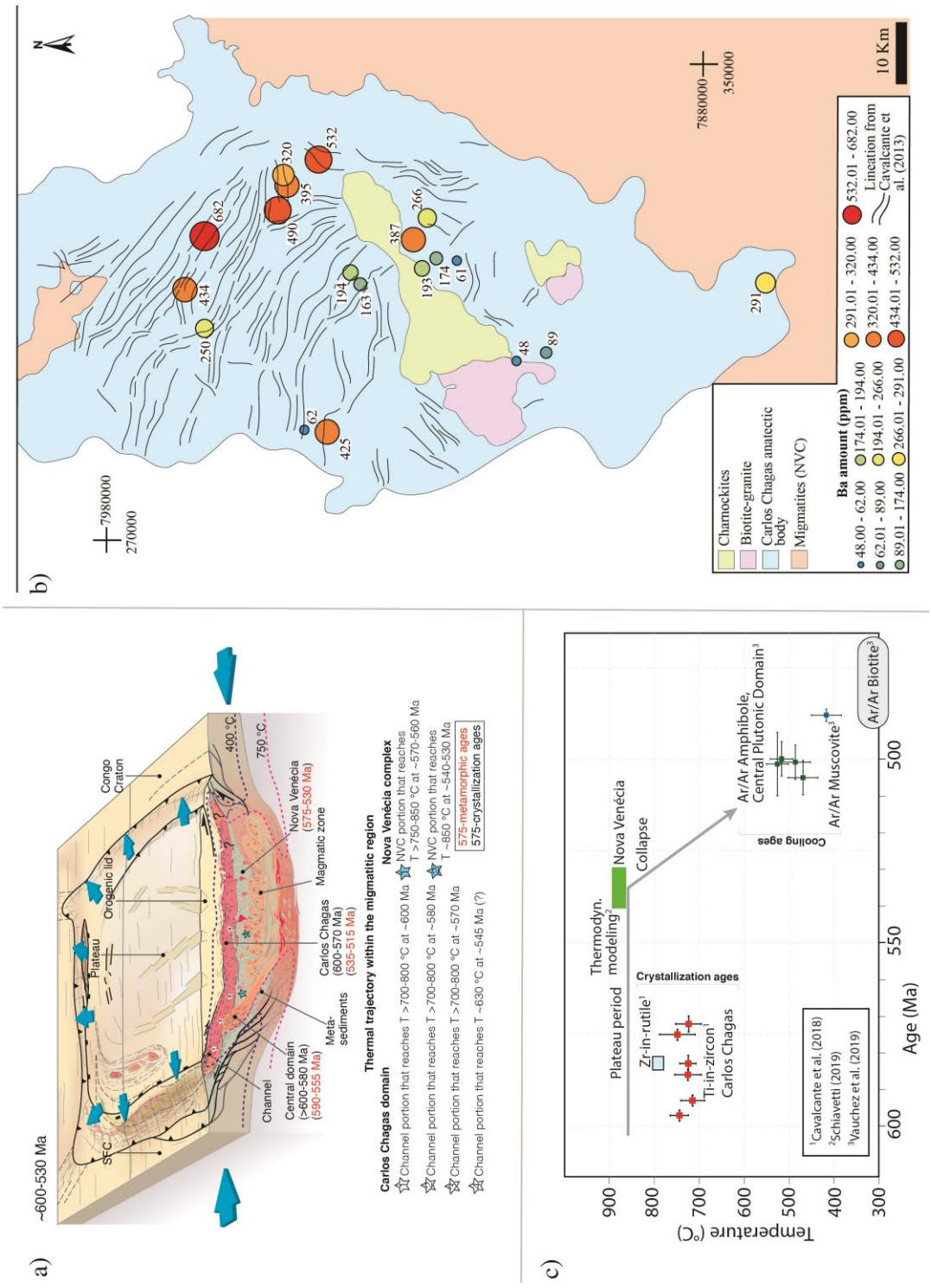

Figure 16: (a) Block diagram illustrating the pervasive partial melting in the Araçuaí middle crust and the plateau development during the orogeny. (b) Geological map of the Eastern

domain displaying the distribution of Ba (barium) concentrations. (c) Temperature - age diagram showing the thermal evolution of the Eastern domain as constrained by thermochronological data.

6.2. Geological meaning of the late-orogenic charnockites

Charnockitic rocks have a widespread occurrence within the Araçuaí belt and have been typically classified within the G5 suite of Pedrosa-Soares et al. (2011) alongside with other granitic intrusions (e.g., the Caladão granite). In this study, we analyzed one of the most important bodies that crops out near the city of Barra de São Francisco (BSF; Fig. 4), and a smaller associated body nearby, both located within the central portion of the CCD.

Based on their age and their geochemical characteristics, charnockites have been interpreted as part of the post-collisional (520-480 Ma; Pedrosa-Soares et al., 2011) magmatism of the Araçuaí orogen. The emplacement ages for the BSF rocks range between 508-498 Ma (Gradim et al., 2014; Melo et al., 2020). The geochemistry of the BSF body shows a ferroan, metaluminous signature (Figs. 14e, f); samples that are slightly peraluminous (e.g., #394, #1231, #696, #697) have garnet as part of the mineral assemblage and are mostly located in the eastern part of the intrusion. While there is no significant difference in the emplacement ages obtained by Melo et al. (2020) for the charnockites in the eastern and western part of the BSF body, the mineral assemblage (presence of either garnet or amphibole) changes spatially, which puts into question whether the BSF is one single connected body or if there are two adjacent individual bodies.

The geochemistry of these BSF rocks supports a late-orogenic origin for the charnockites with composition akin to A-type granites (Figs. 14g, 15a, 15b), although the Nb-Y-Ce does not allow us to discriminate whether this is a mantle-crust mix or an enriched mantle-derived melt (Fig. 15c). From the diagrams of Plank (2005), the mantle seems to be the primary source of

the magmas (Figs. 15d and 15e), with the garnet-bearing charnockites showing a clear influence of the continental crust (Figs. 15d-e) and a contribution of the lower crust also as source of crustal contamination for many of the samples. This same pattern is similar to what is observed in the charnockites of the entire belt based on the compilation by Araujo et al. (2020), although some samples do display different characteristics, particularly samples that fall within the pre-plate collision field, which implies that 1) local processes, i.e., different crustal contribution or different amounts of contamination, can slightly impact the geochemistry of the rocks but still preserve major geochemical features, 2) there is more than one episode of charnockite generation, possibly during different stages of the orogen evolution.

For the late-orogenic charnockites studied here, crustal contamination is thought to have occurred both during magma ascension (e.g., heating and melting of the lower crust) and emplacement in the middle crust, which is supported not only by the geochemistry of the charnockitic rocks here presented, but also by the presence of xenoliths of gneisses on the outcrop scale (Fig. 6h), and the Hf isotopes obtained by Melo et al. (2020), which have indicated mixed magma compositions, i.e., more than one source contribution. Different degrees and sources of crustal contamination would also help explain the diversity of the mineralogical assemblage; while the rocks with garnet are more peraluminous and possibly have assimilated a sedimentary-derived material, enriched in Al (given the chemistry of the observed xenoliths), the metaluminous charnockites contain amphibole instead of garnet, indicating an enrichment in H_2O in the late stages of crystallization but without direct evidence for local melt contamination.

The granites in contact with the charnockites (samples #697A, #697B, # 1231A) have a geochemical signature very similar to the charnockites (Fig.15j), despite their different outcrop color and lack of orthopyroxene in the mineral assemblage. The texture of these granites is also remarkably similar to those described for the charnockites, and along with a similar major and

trace element pattern, strongly suggest that these granites are genetically related to the charnockites and not to any other granitic intrusion in this area. Given that charnockitic magmas are thought to contain Opx due to specific magma characteristics, including T, fO_2, and water content (Frost and Frost, 2008), it is possible that upon emplacement, the magma has interacted with the host rock enough to change the magma characteristics, so that Opx would not be further a stable phase. However, assimilation would not contribute enough material to significantly change the whole rock geochemical composition (e.g., Thompson et al., 2002; Glazner, 2007).

6.3. Geodynamic of a hot orogenic core in the context of an intracontinental orogen

The anatectic core of the Araçuaí belt represented by the CCD and NVC displays multiple evidence of regional-scale high temperature metamorphism associated with widespread partial melting over an area >30,000 km^2. Magmatic planar fabric in the CCD is dominantly subhorizontal, while the NVC exhibits moderate to steep gneissic banding (Schiavetti, 2019; Fig. 4) and microstructures suggestive of deformation in the presence of magma (Figs. 9a-c; e, f). Pressure and current crustal thickness (Assumpção et al., 2013) estimates suggest that the Araçuaí crust was thickened to ca. 60-70 km in the CCD during the orogenesis and that minimum temperature at peak metamorphism was >800 °C in this domain (see Cavalcante et al., 2014 for details) and 750-850 °C in the NVC (e.g., Richter et al. 2016; Schiavetti, 2019). In the NVC, peak metamorphism is suggested to occur at ca. 540-530 Ma (Schiavetti, 2019; Fig. 16c), while in the CCD, high temperature conditions related to partial melting are maintained from ~600 Ma to at least ~570 Ma (Cavalcante et al., 2018; Fig. 16c). The crustal thickening of ~60 km implies shortening of ~500 km (Cavalcante et al., 2019), which is somewhat difficult to accomplish in the confined setting of the Araçuaí belt. The confined nature consequently imposes an insurmountable space problem to install an ocean of any size, suggesting that the Araçuaí belt is an example of intracontinental orogeny (e.g., Cavalcante et al., 2019; Fossen et

al., 2020a; Konopásek et al., 2020). In such an intracontinental setting, the pre-orogenic history could be associated with multi-stage rifting and crustal hyperextension during the late Rodinia break-up, without the development of large amounts of oceanic lithosphere (Fossen et al., 2017, 2020a; Cavalcante et al., 2019).

A supposed hyperextended pre-orogenic continental crust, filled with pelite-rich sedimentary rocks (for example the Macaubás basin), would promote an overall HPE-rich crust that after orogenic thickening may drive high temperature metamorphism (~850 °C) due to radiogenic heating (e.g., England and Thompson, 1986; Vanderhaeghe et al., 2003; Brown, 2007; Clark et al., 2015). Such metamorphic conditions might be sustained in the middle crust for several tens of millions of years provided enough incubation time (>50 My), which generally occurs if plateau-like thickened crust forms and erosion rates are low (e.g., McKenzie and Priestley, 2008; Clark et al. 2011, 2015).

The dominant subhorizontal magmatic fabric recorded in CCD (Cavalcante et al., 2013) and the occurrence of metatexites associated with diatexites and leucogranites in short distances between outcrops (Fig. 4) suggest in-source partial melting of the middle crust and limited vertical magma transport, precluding the formation of isolated magmatic plutons/batholiths in the upper crust. The formation and trapping of such large volumes of magma in the middle crust implies a drastic rheological weakening of the continental crust, making it unable to support the topographic load and consequently susceptible to gravitational deformation. Such a rheological modification results in the formation of an orogenic plateau (e.g., Vanderhaeghe, 2012), which may develop after a critical crustal thickness of ca. 50 km is reached due to orogenic thickening (e.g., Rey et al. 2010). Taking into account the structural pattern of the CCD as well as its morphological migmatitic aspects and its slow cooling character, we suggest that the CCD is the record of an ancient orogenic plateau. The development of such a plateau in the Araçuaí belt might have contributed to the maintenance of high temperature conditions

for long time periods. In such a plateau setting peak metamorphism would be reached tens of millions of years after the plateau formation and would be most likely recorded in migmatitic rocks with fabric geometry that facilitates melt extraction, such as the NVC. Indeed, the steeply dipping planar fabrics recorded in the NVC (Fig. 4) allows for more vertical magma extraction, making it prone to preserve G-UHT (Granulite-Ultra High Temperature) assemblages (e.g., Burg and Vanderhaeghe, 1993; Chardon et al., 2009).

The high concentration of HPE (U, K, and Th; Table 2) in middle-lower crustal rocks (CCD and NVC) are enough to produce high amounts of heat (e.g., Horton et al., 2016). Such amounts of heat production could well be a long-lived heat source for metamorphism and associated partial melting during the Araçuaí orogeny, assuming orogenic plateau development. Therefore, we suggest that radiogenic heat production derived from thickening of a pre-orogenic hyperextended crust (e.g., Cavalcante et al., 2019) is a reasonable long-lived and continuous heat source for metamorphism and associated partial melting in the Araçuaí belt.

Orogenic plateaus may exist for long periods of time (at least >10 My for the Tibet-Himalayas system; Rey et al., 2010) as long as several key factors are kept more or less stable (for example, continuous heat production and convergence, boundary conditions, extension associated with lateral gravitational spreading balanced by convergence-driven thickening, low erosion rates, etc.) (e.g., Clark et al. 2015). Assuming that the CCD represents a long-lived (from ~600 to ~570) partially molten weak layer trapped in the middle crust levels of the Araçuaí orogenic plateau, it is reasonable to think that the Araçuaí thickened crust lasted for several tens of millions of years. The migmatitic region evolved as a deeper G-UHT terrane (NVC) with peak temperature at 540-530 Ma, while the overlain CCD sustained suprasolidus temperatures (>700 °C) until at least 570 Ma, but likely up to ~540 Ma, when the NVC reaches HT conditions (Fig. 16a). In fact, a rough estimate based on cooling rates calculations suggests

that magmatic rocks in the Araçuaí belt, including the CCD, reached the solidus temperature (~630 °C) only at ~545-555 Ma (Vauchez et al., 2019).

60 My is thought to be a minimum time for the radiogenic heat source to provide the thermal energy needed to overcome the thermal buffering caused by the formation of a partially molten layer, as this layer acts as a heat sink with lower capacity to transfer heat upward due to its lower conductivity (e.g., Clark et al. 2011). Such a minimum time for the Araçuaí orogenesis is supported by the several ages of peak metamorphism recorded in the NVC (571-560 Ma for peak at 750-850 °C, Munhá et al., 2005 and Richter et al., 2016; 540-530 Ma for peak at ~850 °C, Schiavetti, 2019), by the crystallization ages recorded in deformed rocks of the CCD (~600 to ~570 Ma, Cavalcante et al., 2018), in the Central domain (~610 to 570 Ma; Mondou et al., 2012; Gonçalves et al., 2016), and in the Western domain (530-535 Ma; Petitgirad et al., 2009). If the development of this G-UHT terrane occurs in the final stage of the Gondwana amalgamation, as it occurs in other hot orogens in Gondwana (e.g., Clark et al., 2015), from 540-530 Ma, one would expect a destabilization of the orogenic plateau, decompression, and consequently, collapse. Plateau collapse after attaining G-UHT conditions would result in asthenospheric upwelling, a late heat source likely responsible for the generation of charnockite and associated granites at ~520-480 Ma.

7. **Regional implications**

The Araçuaí hot orogen is characterized by the presence of a large volume of magmatic rocks that has previously been classified as three groups based on the evolution of the orogeny (Pedrosa-Soares et al., 2001; Gradim et al., 2014 and references therein): (1) pre-collisional (ca. 630-580 Ma), (2) syn-collisional (ca. 590-545 Ma) and (3) post-collisional (ca. 535-480 Ma). The origin of the magmatic rocks over these three stages has been attributed to four different heat sources (Gradim et al. 2014; Tedeschi et al., 2016 and references therein) associated with:

(1) subduction of oceanic crust, which is suggested to generate hot pre-collisional magmas; (2) "heat release from thrust stacking of the hot arc onto the back-arc region, together with radiogenic heat release from the collisional thickened crust" (Gradim et al., 2014), which is suggested to be the heat source for the syn-collisional magmas; (3) "late heat release from the thickened granite-rich crust" (Gradim et al., 2014), which is suggested to be the heat source for the late- to post-collisional magmatism (ca. 545-530 Ma) and; (4) "asthenosphere ascent related to slab breakoff, followed by delamination of lithospheric mantle" (Gradim et al., 2014) associated with late orogenic collapse, which is suggested to be the heat source for the post-collisional magmas. In such an episodic heat setting, rocks would be cooled and heated, almost at the same time, implying an orogenic setting where magma crystallization and metamorphism occur simultaneously in the same rock. For example, sample LG28 (Table 2 in Gonçalves et al., 2016) from the pre-collisional group, close to the town of Águas Formosas (Fig. 2), displays crystallization ages (595 ± 13 Ma) that in terms of analytical uncertainties overlap in time with its metamorphism/migmatization (576 ± 7 Ma). Likewise, samples from the CCD produced crystallization (577 ± 6 Ma and 576 ± 3 Ma) and metamorphic (562 ± 11 Ma and 569 ± 14 Ma) ages in monazite and zircon, respectively, that overlap in time (Fig. 3 and Table 1, samples CC31 and CC37 from Melo et al., 2017b).

Given the confined nature of the Araçuaí belt that precludes the formation of an ocean of any size (Cavalcante et al., 2019), and considering the structural evidence for plateau development during orogeny (Cavalcante et al., 2013; 2018), the slow cooling rates (3-5 °C/My) estimated for the Araçuaí belt (Petitgirard et al., 2009; Vauchez et al., 2019), and the high amounts of HPEs concentrated in middle crustal rocks (Table 2), we suggest that radiogenic decay in a thickened crust is the main heat source for the long-lived magmatism in the Araçuaí belt, assuming a pre-orogenic hyper-extended crust enriched in HPEs. However,

numerical modeling studies are required to accurately quantify the amount of heat that can be produced from the CCD and NVC rocks during the orogeny.

If we consider that the onset of orogenesis, i.e., onset of crustal thickening in the Araçuaí belt, occurred at ~650 Ma, around the same time period that the Dom Feliciano-Gariep (Konopásek et al., 2020 and references therein), and that a minimum time of ~20 Ma is required for a thickened crust to reach a temperature high enough to trigger widespread partial melting at deep crustal levels (>800 °C; Horton et al., 2016), at ~630 Ma the orogenic crust would have been significantly thickened, and radiogenic decay could well be the main heat source, for magma generation and metamorphism up to 540-530 Ma. In such a long-lived hot setting, magmas of different compositions could be generated synchronously; some of them could accumulate at middle crustal level, while others could efficiently migrate from their source areas. We suggest that the synchronous magmatism in the Central (tonalites and granodiorites) and Eastern (migmatites and anatectic granites of the CCD, and migmatites of the NVC) domains of the Araçuaí belt, from ~600 to ~570 Ma, occurred due to: (1) metamorphism and melting of the lower crust and underlying mantle, as pointed by Vauchez et al. (2019 and references therein), efficiently migrated from its source, for the Central domain rocks; (2) partial melting of the middle/lower crust, combined with magmatic accumulation forming a rheologically sub-horizontal weak layer (CCD) and efficient magma loss from the underlaying NVC.

The fabric geometry observed in the Central domain rocks, where steeply-dipping/plunging planar and linear fabrics occur (e.g., Mondou et al., 2012; Angelo et al., 2020), strongly supports magma emplacement, i.e., efficient magma migration from its source, likely from the deep root of the orogenic belt. Such a magma emplacement would be, at least in part, synchronous with the anatexis of the middle/lower crust represented by the CCD and Nova Venécia complex (Fig. 16a). However, even though Sr and Nd isotopes point to a dominant contribution of continental

crust in the genesis of rocks from the Central domain (Nalini et al., 2000), as the proportion of crustal and mantle components are unknown (e.g., Gonçalves et al., 2014), the process involved in the formation of these rocks still requires further investigation.

The late magmatism in the Araçuaí belt occurred between 520-480 Ma (Pedrosa-Soares et al., 2011), and includes charnockitic rocks with a magmatic age between 508-498 Ma (Gradim et al., 2014; Melo et al., 2020). The geochemistry of these rocks, which are clearly distinct from the CCD, evidence a mantle origin for the melts with a contribution of crustal material, as supported by field evidence (Fig. 6h) and isotopic data (Melo et al., 2020). We interpret these charnockites to have formed as a result of an orogenic collapse during the late stages of the Araçuaí orogeny, as an extensional event can produce asthenospheric upwelling. This also resulted in melting of the mantle and ascension of hot and dry magmas, which also promoted some melting of the lower crust, and assimilated material during its magmatic history. The associated granites (i.e., in direct contact with the charnockites) described in this work likely represent an interaction between the charnockitic magma and the country rock.

8. Conclusions

In this contribution we have added new geochemical data of rocks from the hinterland (Eastern domain) of the Araçuaí belt to the geochemical dataset available in the literature, revisited morphological aspects of migmatitic rocks from the CCD, and presented the macro- and micro-scale aspects of charnockites and its associated granites. We have discussed these data in line with relevant geochronological and geochemical information, to contribute to the understanding of the orogenic evolution of this belt during the Gondwana amalgamation.

Macro and micro-scale morphological aspects of the CCD suggest occurrence of partial melting reactions together with melt crystallization structures, typical of migmatitic rocks. Considering the overlaps between dates of what has been interpreted as crystallization and what

has been interpreted as metamorphism of the CCD, the Th/U ratios that do not allow for differentiation between inherited, metamorphic and magmatic zircons, and the dominant subhorizontal magmatic fabric suggestive of limited vertically magma movements, we reinforce that the CCD is the record of a long-lived (at least 30 My) in-source crustal anatexis during orogenic thickening. Hence, the CCD rocks are witnesses of in-source melting processes at deep crustal levels with limited melt loss through the crust. It also represents a rheologically weak layer trapped in mid crustal levels that might have triggered the development of an orogenic plateau.

Geochemical data suggest that the CCD and NVC rocks are the record of a single pervasive anatectic event in the Araçuaí continental middle crust. The dominant peraluminous signature of the CCD and NVC melts suggests that these magmas are the result of partial melting of continental crust. The chemical variabilities of these rocks are likely due to processes of filtering of residuum and also the contribution of fractional crystallization processes.

The charnockitic rocks are chemically different from the CCD and NVC, therefore they did not originate from the same source. We postulate that these rocks originated from an enriched mantle reservoir and that crustal contamination occurred during the ascension and emplacement of these bodies in the crust.

Radiogenic decay of a thickened crust enriched in HPEs (U, Th and K) is suggested to be the main heat source for metamorphism and associated partial melting for most part of the orogenic evolution of the Araçuaí belt, i.e., from ~630 to ~530 Ma, rather than multiple episodic heat sources associated with subduction process in the early stages of the orogeny, as previously suggested. Asthenospheric upwelling and mantle delamination driven by orogenic thermal maturation and plateau destabilization are suggested to be the heat source for the generation of hot charnockitic magmas in the late stages of the Araçuaí orogeny.

Acknowledgments

We appreciate the Brazilian funding through the agencies FAPESP – Fundação de Amparo a Pesquisa do Estado de São Paulo –, CAPES – Coordenação de Aperfeiçoamento de Pessoal de Nivel Superior –, and CNPq – Conselho Nacional de Desenvolvimento Científico e Tecnológico – (project numbers 2010/03537-7 and BEX 4190/11-4 to CC, 404767/2016-8 to VTM and 8303201/19-3 to MHBMH). We are particularly grateful to Haakon Fossen for constructive suggestions, and all our Brazilian and international colleagues for the several pleasant discussions that motivated the writing of this paper. We thank Christopher Yakymchuk and Olivier Vanderharghe for their insightful suggestions, which helped to improve this work significantly. We thank Marcos Egydio for his help in the field, Mathias Schannor for careful editorial handling, and Ravi Franzini Meira for joining our team.

References

Alkmim, F.F., Marshak, S., Pedrosa-Soares, A.C., Peres, G.G., Cruz, S.C.P. Whittington, A., 2006. Kinematic evolution of the Araçuaí-West Congo orogen in Brazil and Africa: Nutcracker tectonics during the Neoproterozoic assembly of Gondwana. Precambrian Res. 149, 43–64.

Almeida, F.F.M., Brito Neves, B.B., Carneiro, C.D.R., 2000. The origin and evolution of the South American Platform. Earth Sci. Rev. 50, 77–111.

Angelo, T. V., Egydio-Silva, M., Temporim, F. A., Seraine, M., 2020. Midcrust deformation regime variations across the Neoproterozoic Araçuaí hot orogen (SE Brazil): Insights from structural and magneticfabric analyses. Journal of Structural Geology, 134, 104007.

Araujo, C., Pedrosa-Soares, A., Lana, C., Dussin, I., Queiroga, G., Serrano, P., Medeiros-Junior, E., 2020. Zircon in emplacement borders of post-collisional plutons compared to country rocks: A study on morphology, internal texture, U-Th-Pb geochronology and Hf isotopes (Araçuaí orogen, SE Brazil). Lithos, 352-353, 105252.

Ashworth J.R., McLellan, E.L.,1985., Texture, in: Migmatites. Ashworth, J.R., Glasgow, pp. 180-203.

Assumpção, M., Bianchi, M., Julià, J., Dias, F. L., França, G. S., Nascimento, R., Drouet, S., Pavão, C. G., and Albuquerque, D. F., 2013. Crustal thickness map of Brazil: data compilation and main feautures, J. S. Am. Earth Sci., 43, 74–85.

Barbey, P., Brouand, M., Le Fort, P., Pêcher, A., 1996. Granite-migmatite genetic link: the example of the Manaslu granite and Tibetan Slab migmatites in central Nepal. Lithos, 38, 63-79.

Batchelor, R.A., Bowden, P., 1985. Petrogenetic interpretation of granitoid rock series using multicationic parameters. Chemical Geology 48, 43–55.

Bayer, P., Horn, H.A., Lammerer, R., Schmidt-Thome, K., Weber-Diefenbach, M., and Wiedemann, C., 1986. The Brasiliano Mobile Belt in Southern Esplrito Santo (Brazil) and its Igneous Intrusions. - Zbl. Geol. Paläontol. Teil I, 1985 (9/10): 1429-1439; Stuttgart. https://doi.org/10.1127/zbl_geol_pal_1/1985/1986/1429

Bea, F., 1996. Residence of REE, Y, Th and U in granites and crustal protoliths; implications for the chemistry of crustal melts. Journal of Petrology, 37, 521-552.

Beaumont, C., Jamieson, R. A., Nguyen, M. H., and Medvedev, S., 2004. Crustal channel flows: 1. Numerical models with applications to the tectonics of the Himalayan – Tibet orogen. HIMALAYAN-TIBETAN CRUSTAL CHANNEL FLOWS. J. Geophys. Res. Solid Earth 109. https://doi.org/10.1029/2003JB002809

Beaumont, C., Nguyen, M.H., Jamieson, R.A., and Ellis, S. 2006. Crustal flow modes in large hot orogens. In Channel flow, ductile extrusion and exhumation in continental collision zones. Geological Society, London, Special Publication 268, pp. 91– 145.

Brown, M., 1973. The Definition of Metatexis, Diatexis and Migmatite. Proc. Geol. Ass., 84 (4), 371-382.

Brown, M., Averkin, Y. A., McLellan, E.L., and Sawyer, E., 1995. Melt segregation in migmatites. Journal of Geophysical Research, 100, NO. B8, 655-679.

Brown, M., 2001. Orogeny, migmatites and leucogranites: A review. J. Earth Syst. Sci. 110, 313–336.

Brown, M., 2002, Prograde and retrograde processes in migmatites revisited: Journal of Metamorphic Geology, v. 20, p. 25–40.

Brown, M., 2007. Metamorphic conditions in orogenic belts: a record of secular change. International Geology Review 49, 193–234.

Brueckner, H.K., Cunningham, D., Alkmin, F.F., Marshak, S., 2000. Tectonic implications of Precambrian Sm–Nd dates from the southern São Francisco craton and adjacent Araçuaí and Ribeira belts, Brazil. Precambrian Research, 99, 255-269.

Burg, J. P., and Vanderhaeghe, O., 1993. Structures and way-up criteria in migmatites, with application to the Velay dome (French Massif Central). Journal of Structural Geology, 15, No.11, 1293-1301.

Cavalcante, G.C.G., Egydio-Silva, M., Vauchez, A., Camps, P., Oliveira, E., 2013. Strain distribution across a partially molten middle crust: insights from the AMS mapping of the Carlos Chagas Anatexite, Araçuaí belt (East Brazil). J. Struct. Geol. 55, 79–100.

Cavalcante, G.C.G., Vauchez, A., Merlet, C., Egydio-Silva, M., Holanda, M.H.B., Boyer, B., 2014. Thermal conditions during deformation of partially molten crust from TitaniQ thermometry: rheological implications for the anatectic domain of the Araçuaí belt eastern Brazil. Solid Earth 5, 1223–1242. https://doi.org/10.5194/se-5-1223-2014

Cavalcante, G.C.G., Viegas, L. G. F., Archanjo, C.J, Egydio-Silva, M., 2016. The influence of partial melting and melt migration on the rheology of the continental crust. Journal of Geodynamics, 101, 186–189. https://doi.org/10.1016/j.jog.2016.06.002

Cavalcante, C., Hollanda, M.H, Vauchez, A., Kawata, M., 2018. How long can the middle crust remain partially molten during orogeny? Geology, 46, 839–842. https://doi.org/10.1130/G45126.1

Cavalcante, C., Fossen, H., Almeida, R.P., Hollanda, M.H.B.M., Egydio-Silva, M., 2019. Reviewing the puzzling intracontinental termination of the Araçuaí–West Congo orogenic belt and its implications for orogenic development. Precambrian Res. 322, 85–98. https://doi.org/10.1016/j.precamres.2018.12.025

Chappell, B.W., 1984. Source rocks of I- and S-type granites in the Lachlan Fold Belt, southeastern Australia. Phil. Trans. R. Soc. Land. A 310, 693-707.

Chardon, D., Gapais, D., Cagnard, F., 2009. Flow of ultra-hot orogens: A view from the Precambrian, clues for the Phanerozoic. Tectonophysics, 477, 105-118.

Clark, M. K., and Royden, L. H., 2000. Topographic ooze: Building the eastern margin of Tibet by lower crustal flow, Geology, 28, 703–706.

Clark, C., Fitzsimons, I.C.W., Healy, D., Harley, S.L., 2011. How does the continental crust get really hot? Elements, Vol. 7, 235-240. DOI: 10.2113/gselements.7.4.235.

Clark, C., Healy, D., Johnson, T., Collins, A.S., Taylor, R. J., Santosh, M., Timms, N.E., 2015. Hot orogens and supercontinent amalgamation: A Gondwanan example from southern India. Gondwana Research, 28, 1310-1328.

Corrie, S. L., Kohn, M. J., 2008. Trace-element distributions in silicates during prograde metamorphic reactions: implications for monazite formation. Journal of Metamorphic Geology, vol. 26, p. 451-464.

Cox, K.G., Bell, J.D., Pankhurst, R.J., 1979. The Interpretation of Igneous Rocks. George Allen & Unwin, 450p.

Davis, G. H., Reynolds, S.J., Kluth, C.F., 2012. Structural Geology of Rocks and Regions 3rd edition. 839p. ISBN 978-0-471-15231-6.

De Campos, C. M., Mendes, J. C., Ludka, I. P., Medeiros, S. R., Moura, J. C. and Wallfass, C., 2004. A review of the Brasiliano magmatism in southern Espirito Santo, Brazil, with emphasis on post-collisional magmatism. Journal of the Virtual Explorer, 17, 1-36. https://doi.org/10.3809/jvirtex.2004.00106

De Saint Blanquat, M., Horsman, E., Habert, G., Morgan, S., Vanderhaeghe, O., Law, R., Tikoff, B., 2011. Multiscale magmatic cyclicity, duration of pluton construction, and the paradoxical relationship between tectonism and plutonism in continental arcs. Tectonophysics 500, 20–33. https://doi.org/10.1016/j.tecto.2009.12.009

Didier, J., 1973. Granites and Their Enclaves: The Bearing of Enclaves on the Origin of Granites. Developments in Petrology, 3. Elsevier, Amsterdam.

Douce, A.E.P. and Johnston, A.D., 1991. Phase equilibria and melt productivity in the pelitic system - implications for the origin of peralunimous granitoids and aluminous granulites. Contributions to Mineralogy and Petrology 107:202–218.

Eby G.N., 1992. Chemical subdivision of A-type granitoids: petrogenetic and tectonic implications. Geology 20, 641–644.

Egydio-Silva, M., Vauchez, A., Raposo, M.I.B., Bascou, J. and Uhlein, A., 2005. Deformation regime variations in an arcuate transpressional orogen (Ribeira belt, SE Brazil) imaged by anisotropy of magnetic susceptibility in granulites. Journal of Structural Geology, 27, 1750.

Egydio-Silva, M., Vauchez, A., Fossen, H., Cavalcante, G.C.G., Xavier, B.C., 2018. Connecting the Araçuaí and Ribeira belts (SE – Brazil): Progressive transition from contractional to transpressive strain regime during the Brasiliano orogeny. J. S. Am. Earth Sci. 86, 127–139. https://doi.org/10.1016/j.jsames.2018.06.005

England, P.C., Thompson, A., 1986. Some thermal and tectonic models for crustal melting in continental collision zones. In: Coward, M.P., Ries, A.C. (Eds.), Collision Tectonics. Geol. Soc. Spec. Pub, pp. 83–94.

Fossen, H., Cavalcante, G. C., Almeida, R. P., 2017. Hot Versus Cold Orogenic Behavior: Comparing the Araçuaí-West Congo and the Caledonian Orogens. Tectonics, 36, 2159-2178. https://doi.org/10.1002/2017TC004743

Fossen, H., Cavalcante, C., Konopásek, J., Meira, V.T., Almeida, R. P., Hollanda, M.H.M.B., Trompette, R., 2020 (a). A critical discussion of the subduction-collision model for the Neoproterozoic Araçuaí-West Congo orogen. Prec. Res, 343, 105715. https://doi.org/10.1016/j.precamres.2020.10571

Fossen, H., Meira, V.T., Cavalcante, C., Konopásek, J., Janoušek, V., 2020 (b). Comment to "Neoproterozoic magmatic arc systems of the central Ribeira belt, SE-Brazil, in the context of the West-Gondwana pre-collisional history: A review". Journal of South American Earth Sciences. https://doi.org/10.1016/j.jsames.2020.103052

François, C., Baludikay, B.K, Storme, J.Y., Baudet, D., Paquette, J.L., Fialin, M., Javaux. E.J., 2017. Contributions of U-Th-Pb dating on the diagenesis and sediment sources of the lower group (BI) of the Mbuji-Mayi Supergroup (Democratic Republic of Congo). Prec. Res. 298, 202-219.

Frost, R.B., Barnes, C.G., Collins, W.J., Arculus, R.J., Ellis, D.J., Frost, C.D., 2001. A geochemical classification for granitic rocks. Journal of Petrology 42, 2033–2048.

Frost, B.R. and Frost, C.D., 2008. On charnockites. Gondwana Research 13, 30-44.

Glazner, A. F. 2007. Thermal limitations on incorporation of wall rock into magma. Geology 35, 319-322.

Gébelin, A., Roger, F., Brunel, M., 2009. Syntectonic crustal melting and high-grade metamorphism in a transpressional regime, Variscan Massif Central, France. Tectonophysics, 477, 229-243.

Gonçalves, L., Farina, F., Lana, C., Pedrosa-Soares, A.C., Alkmim, F. and Nalini Jr, H.A., 2014. New U–Pb ages and lithochemical attributes of the Ediacaran Rio Doce magmatic arc, Araçuaí confined orogen, southeastern Brazil. J. S. Am. Earth Sci. 52, 129–148.
Gonçalves, L., Alkmim, F., Pedrosa-Soares, A.C., Dussin, I.A., Valeriano, C.M., Lana, C., Tedeschi, M.F., 2016. Granites of the intracontinental termination of a magmatic arc: an example from the Ediacaran Araçuaí Orogen, Southeastern Brazil. Gondwana Res. http://dx.doi.org/10.1016/J.GR.2015.07.015.
Gorczyk, W., Hobbs, B., Gessner, K., Gerya, T., 2013. Gondwana Research, 24, 838-848.
Gorczyk, W., Vogt, K., 2015. Tectonics and melting in intra-continental settings. Gondwana Research 27, 196-208.

Gradim, C., Roncato, J., Pedrosa-Soares, A.C., Cordani, U., Dussin, I., Alkmim, F.F., Queiroga, G., Jacobssohn, T., Silva, L.C., Babinski, M., 2014. The hot back-arc zone of the Araçuaí orogen, Eastern Brazil: from sedimentation to granite generation. Brazilian Journal of Geology 44, 155–180.

Guernina, S., and Sawyer, E., 2003. Large-scale melt-depletion in granulite terranes: an example from the Archean Ashuanipi Subprovince of Quebec. J. metamorphic Geol., 21, 181–201.

Harris, N.B.W., Caddick, M., Kosler, J., Goswami, S., Vance, D., Tindle, A.G., 2004. The pressure–temperature–time path of migmatites from the Sikkim Himalaya. J. metamorphic Geol., 2004, 22, 249–264. doi:10.1111/j.1525-1314.2004.00511. x.

Heilbron, M., Tupinambá, M., Valeriano, C.M., Armstrong, R., Silva, L.G.E., Melo, R.S., Simonetti, A., Pedrosa-Soares, A.C., Machado, N., 2013. The Serra da Bolívia complex: The record of a new Neoproterozoic arc-related unit at Ribeira belt. Precambrian Res. 238, 158–175. https://doi.org/10.1016/j.precamres.2013.09.014.

Holness, M.B., Cesare, B., and Sawyer, E.W., 2011. Melted rocks under the microscope: microstructures and their interpretation. Elements, 7, 247-252.
DOI: 10.2113/gselements.7.4.247

Horton, F., Hacker, B., Kylander-Clark, A., Holder, R., and Jöns, N., 2016, Focused radiogenic heating of middle crust caused ultrahigh temperatures in southern Madagascar: Tectonics, v. 35, p. 293– 314, https://doi.org/10.1002/2015TC004040.

Irvine, T.N., Baragar, W.R.A., 1971. A guide to the chemical classification of the common volcanic rocks. Can. J. Earth Sci. 8, https://doi.org/10.1139/e71-055

Jamieson, R.A., Beaumont, C., Warren, C.J., Nguyen, M.H., 2010. The Grenville Orogen explained? Applications and limitations of integrating numerical models with geological and geophysical data. Can. J. Earth Sci. 47: 517–539. doi:10.1139/E09-070.

Jung, S., Hoffer, E., Masberg, P., Hoernes, S., 1995. Geochemistry of granitic in-situ low-melt fractions - an example from the Central Damara Orogen. Communs geol. Surv. Namibia, 10, 21-32.

Jung, S., Hoernes, S., Masberg, P., Hoffer, E., 1999. The Petrogenesis of Some Migmatites and Granites (Central Damara Orogen, Namibia): Evidence for Disequilibrium Melting, Wall-Rock Contamination and Crystal Fractionation. Journal of Petrology, Vol. 40. Number 8.1241-1269.

Kelsey, D. E., Clark, C., Hand, M., 2008. Thermobarometric modelling of zircon and monazite growth in melt-bearing systems: examples using model metapelitic and metapsammitic granulites. Journal of Metamorphic Geology, vol. 26, p. 199-212

Kohn, M. J., and Malloy, M. A., 2004. Formation of monazite via prograde metamorphic reactions among common silicates: Implications for age determinations. Geochimica et Cosmochimica Acta, vol. 68, p. 101-113.

Konopásek, J., Hoffmann, K.H., Sláma, J., Košler, J., 2017. The onset of flysch sedimentation in the Kaoko Belt (NW Namibia) – Implications for the pre-collisional evolution of the Kaoko–Dom Feliciano–Gariep Orogen. Precambrian Res. 298, 220–234. https://doi.org/10.1016/j.precamres.2017.06.017.

Konopásek, J., Janoušek, V., Oyhantçabal, P., Sláma, J., Ulrich, S., 2018. Did the circum-Rodinia subduction trigger the Neoproterozoic rifting along the Congo–Kalahari Craton margin? Int. J. Earth Sci. 107, 1859–1894. https://doi.org/10.1007/s00531-017-1576-4.

Konopásek, J., Cavalcante, C., Fossen, H., Janoušek, V., 2020. Adamastor – an ocean that never existed?. Earth Science Reviews, 205, 103201.
https://doi.org/10.1016/j.earscirev.2020.103201

Kriegsman, L. M., and Álvarez-Valero, A. M., 2010. Melt-producing versus melt-consuming reactions in pelitic xenoliths and migmatites. Lithos, 116, 310-320.

Kruckenberg, S.C., Whitney, D.L., Teyssier, C., Fanning, C.M., Dunlap, W.J., 2008. Paleocene-Eocene migmatite crystallization, extension, and exhumation in the hinterland of the northern Cordillera: Okanogan dome, Washington, USA. Geol. Soc. Am. Bull. 120, 912–929. https://doi.org/10.1130/B26153.1

Maharani, K., Chidambaram, S., Rajendran, S., 2016. The study of major element geochemistry of migmatites in and around Melur region, Madurai district, Tamil Nadu, India. Bulletin of Pure and Applied Sciences, Vol. 35F-Geology (No. 1-2), 71-80. Doi 10.5958/2320-3234.20.16-00003.2.

Martins, V.T.S., Teixeira, W., Noce, C.M., Pedrosa-Soares, A.C., 2004. Sr and Nd Characteristics of Brasiliano/Pan-African Granitoid Plutons of the Araquai Orogen, Southeastern Brazil: Tectonic Implications Gondwana Research, 7, No.1, 75-89.

McDonough, W.F., Sun, S.S., 1995. The composition of the Earth. Chemical Geology 120, 223–253.

McKenzie, D., and Priestley, K., 2008. The influence of lithospheric thickness variations on continental evolution. Lithos, 102, 1-11.

Meira, V.T., Garcia-Casco, A., Juliani, C., Almeida, R.P., Schorscher, J.H.D., 2015. The role of intracontinental deformation in supercontinent assembly: insights from the Ribeira Belt, Southeastern Brazil (Neoproterozoic Western Gondwana). Terra Nova 27, 206–217.

Meira, V.T., Garcia-Casco, A., Hyppolito, T., Juliani, C., Schorscher, J.H.D., 2019a. Tectono-metamorphic evolution of the Central Ribeira Belt, Brazil: a case of late Neoproterozoic intracontinental orogeny and flow of partially molten deep crust during the assembly of West Gondwana. Tectonics 38. https://doi.org/10.1029/ 2018TC004959.

Meira, V.T., Garcia-Casco, A., Juliani, C., Schorscher, J.H.D., 2019b. Late Tonian within-plate mafic magmatism and Ediacaran partial melting and magmatism in the Costeiro Domain, Central Ribeira Belt, Brazil. Precambrian Res., 334, 105440. https://doi.org/10.1016/j.precamres.2019.105440

Melo, M. G., Lana, C., Stevens, G., Pedrosa-Soares, A. C., Gerdes, A., Alkmin, L. A., Nalini Jr. H. A., Alkmim F. F., 2017a. Assessing the isotopic evolution of S-type granites of the Carlos Chagas Batholith, SE Brazil: Clues from U–Pb, Hf isotopes, Ti geothermometry and trace element composition of zircon. Lithos 284–285, 730–750. https://doi.org/10.1016/j.lithos.2017.05.025

Melo, M.G., Stevens, G., Lana, C., Pedrosa-Soares, A.C., Frei, D., Alkmim, F.F., Alkmin, L.A., 2017b. Two cryptic anatectic events within a syn-collisional granitoid from the Araçuaí orogen (Southeastern Brazil): evidence from the polymetamorphic Carlos Chagas batholith. Lithos 277, 51–71. https://doi.org/10.1016/j.lithos.2016.10.012

Melo, M. G., Lana, C., Stevens, G., Hartwig, M. E., Pimenta, M. S., Nalini Jr., H. A., 2020. Deciphering the source of multiple U–Pb ages and complex Hf isotope composition in zircon from post-collisional charnockite-granite associations from the Araçuaí orogen (southeastern Brazil). Journal of South American Earth Sciences, 103, 102792.

Mondou, M., Egydio-Silva, M., Vauchez, A., Raposo, M.I.B., Bruguier, O., Oliveira, F., 2012. Complex, 3-D strain patterns in a synkinematic tonalite batholith from the Araçuaí Neoproterozoic orogen (Eastern Brazil): evidence from combined magnetic and isotopic chronology studies. J. Struct. Geol. 39, 158–179.

Moreno, J.A., Molina, J.F., Montero, P., Abu Anbar, M., Scarrow, J.H., Cambeses, A., Bea, F., 2014. Unraveling sources of A-type magmas in juvenile continental crust: Constraints from compositionally diverse Ediacaran post-collisional granitoids in the Katerina Ring Complex, southern Sinai, Egypt. Lithos 192–195, 56–85.

Munhá, J.M.U., Cordani, U.G., Tassinari, C.C.G., Palácios, T., 2005. Petrologia e termocronologia de gnaisses migmatíticos da Faixa de Dobramentos Arac¸uaí (Espírito Santo, Brasil). Rev. Bras. Geociênc. 35 (1), 123–134.

Nalini, H.A., Bilal, E., Paquette, J.-L., Pin, C., Machado, R., 2000. Géochronologie U–Pb et géochimie isotopique Sr–Nd des granitoïdes néoprotérozoïques des suites Galiléia et Urucum, vallée du Rio Doce, Sud-Est du Brésil. C. R. Acad. Sci. Ser. IIA Earth Planet. Sci. 331, 459–466.

Nelson, K.D., Wenjin, Z., Brown, L.D., Kuo, J., Jinkai, C., Xianwen, L., Klemperer, S.L., Makovsky, Y., Meissner, R., Mechie, J., Kind, R., Wenzel, F., Ni, J., Nabelek, J., Leshou, C., Handong, T., Wenbo, W., Jones, A.G., Booker, J., Unsworth, M., Kidd, W.S.F., Hauck, M., Alsdorf, D., Ross, A., Cogan, M., Wu, C., Sandvol, E.A., and Edwards, M., 1996. Partially molten middle crust beneath southern Tibet; synthesis of Project INDEPTH results: Science, v. 274, p. 1684- 1688.

Noce, C. M., Pedrosa-Soares, A. C., Piuzana, D., Armstrong, R., Laux, J. H., Campos, C. M., Medeiros, S. R., 2004. Revista Brasileira de Geociências, 34 (4), 587-592.

Oliveira, M.-J.R., Pinto, C.P., Féboli, W.L., and Alves dos Santos, R. 2000. Projeto Leste - Relatório mapa integrado 1:500.000 - Geologia Estrutural e Tectônica. CPRM - COMIG, Belo Horizonte.

Patiño Douce, A. E. & Harris, N., 1998. Experimental constraints on Himalayan anatexis. Journal of Petrology 39, 689–710.

Pawley, M.J, Reid A.J, Dutch R.A, and Preiss W.V., 2013. A user's guide to migmatites, Report Book 2013/00016. Department for Manufacturing, Innovation, Trade, Resources and Energy, South Australia, Adelaide.

Pawley, M., Reid, A., Dutch, R., Preiss, W., 2015. Demystifying migmatites: an introduction for the field-based geologist. Applied Earth Science, 124:3, 147-174, DOI: 10.1179/1743275815Y.0000000014

Peccerillo, A. and Taylor, S.R., 1976. Geochemistry of eocene calc-alkaline volcanic rocks from the Kastamonu area, Northern Turkey. Contributions to Mineralogy and Petrology, 58, 63-81.

Pedrosa-Soares, A.C., Noce, C.M., Wiedemann, C., Pinto, C.P., 2001. The Araçuaí-West-Congo Orogen in Brazil: an overview of a confined orogen formed during Gondwana- land assembly. Precambrian Research 110, 307–323.

Pedrosa-Soares, A.C., De Campos, C.P., Noce, C., Silva, L.C., Novo, T., Roncato, J., Medeiros, S., Castañeda, C., Queiroga, G., Dantas, E., Dussin, I., Alkmim, F., 2011. Late Neoproterozoic–Cambrian granitic magmatism in the Araçuaí orogen (Brazil), the Eastern Brazilian Pegmatite Province and related mineral resources. Geological Society of London, Special Publication 350, 25–51.

Peixoto, C.D., Heilbron, M., Ragatky, D., Armstrong, R., Dantas, E., Valeriano, C.D., Simonetti, A., 2017. Tectonic evolution of the Juvenile Tonian Serra da Prata magmatic arc in

the Ribeira belt, SE Brazil: Implications for early west Gondwana amalgamation. Precambrian Res. 302, 221–254. https://doi.org/10.1016/j.precamres.2017.09.017.

Percival, J. J., Konopásek, J., Eiesland, R., Sláma, J., Campos, R.S., Battisti, M.A., Bitencourt, M.F., 2021. Pre-orogenic connection of the foreland domains of the Kaoko–Dom Feliciano–Gariep orogenic system. Prec. Res., 354, 106060.

Petitgirard, S., Vauchez, A., Egydio-Silva, M., Bruguier, O., Camps, P., Monié, P., Babinski, M., Mondou, M., 2009. Conflicting structural and geochronological data from the Ibituruna quartz-syenite (SE Brazil): effect of protracted orogeny and slow cooling rate? In: Chardon, D., Rey, P. (Eds.), Hot Orogens Special Issue Tectonophysics, 477, 174–196 (3).

Plank, T., 2005. Constraints from Thorium/Lanthanum on sediment recycling at subduction zones and the evolution of the continents. Journal of Petrology, 46, 921-944.

Prakash, A., Piazolo, S., Saha, L., Battacharya, A., Pal, D. K., Sarkar, S., 2018. Deformation behavior of migmatites: insights from microstructural analysis of a garnet–sillimanite–mullite–quartz–feldspar-bearing anatectic migmatite at Rampura–Agucha, Aravalli–Delhi Fold Belt, NW India. International Journal of Earth Sciences, 107, 2265-2292. https://doi.org/10.1007/s00531-018-1598-6.

Rey, P. F., Teyssier, C., Whitney, D., 2010. Limit of channel flow in orogenic plateau. Lithosphere, v2. No.5, 328-332. DOI: 10.1130/L114.1

Richard, A., Montel, Jean-Marc, Leborgne, R., Peiffert, C., Cuney, M., Cathelineau, M., 2015. Monazite Alteration in H2O +/- HCl +/- NaCl +/- CaCl2 Fluids at 150 degrees C and p(sat): Implications for Uranium Deposits. Minerals, MDPI, 2015, 5 (4), pp. 693-706. 10.3390/min5040518

Richter, F., Lana, C., Stevens, G., Buick, I., Pedrosa-Soares, A.C., Alkmim, F.F., Cutts, K., 2016. Sedimentation, metamorphism and granite generation in a back-arc region: records from the Ediacaran Nova Venécia Complex (Araçuaí Orogen, Southeastern Brazil). Precambrian Research 272, 78–100.

Rivers, T., 2009. The Grenville Province as a large hot long-duration collisional orogen – insights from the spatial and thermal evolution of its orogenic fronts. In: MURPHY, J. B., KEPPIE, J. D. & HYNES, A. J. (eds) Ancient Orogens and Modern Analogues. Geological Society, London, Special Publications, 327, 405–444. https://doi.org/10.1144/SP327.17

Rosenberg, C. L. and Handy, M. R., 2005. Experimental deformation of partially melted granite revisited: implications for the continental crust, J. Metamorph. Geol., 23, 19–28.

Royden, L. H., B. C. Burchfiel, R. W., King, Z. Chen, F. Shen, and Liu, Y., 1997. Surface deformation and lower crustal flow in eastern Tibet, Science, 276, 788–790.

Rubatto, D., Williams, I. S., Buick, I. S., 2001. Zircon and monazite response to prograde metamorphism in the Reynolds Range, central Australia. Contributions to Mineral Petrology, vol. 140, p. 458-468

Sawyer, E.W. 1994. Melt segregation in the continental crust. Geology, 22, 1019-1022.

Sawyer, E., 1998. Formation and Evolution of Granite Magmas During Crustal Reworking: the Significance of Diatexites. Journal of Petrology, 39, N6, 1147-1167.
Sawyer, E., 1999. Criteria for the Recognition of Partial Melting. Phys. Chem. Earth (A), Vol. 24, No. 3, 269-279. https://doi.org/10.1016/S1464-1895(99)00029-0

Sawyer, E.W., 2008. Atlas of Migmatites. The Canadian Mineralogist, Special Publication 9. NRC Research Press, Ottawa, Ontario, Canada. 371 p.

Sawyer, E.W., Cesare, B., Brown, M., 2011. When the continental crust melts. Elements, 7 (4), 229-234. https://doi.org/10.2113/gselements.7.4.229

Schiavetti, L.R., 2019. Metamorfismo e geocronologia em orógenos quentes: o caso do Complexo Nova Venécia, Orógeno Araçuaí. Dissertação de mestrado, Universidade de Campinas, 137 pg.

Searle, M.P., Cottle, J.M., Streule, M.J., Waters, D.J., 2010. Crustal melt granites and migmatites along the Himalaya: melt source, segregation, transport and granite emplacement mechanisms. Earth and Environmental Science Transactions of the Royal Society of Edinburgh, 100, 219–233.

Sibson, R.H., 1977. Fault rocks and fault mechanisms. Journal of the Geological Society, 133, 191-213.

Silva, L.C., McNaughton, N.J., Armstrong, R., Hartmann, L., and Fletcher, I., 2005. The Neoproterozoic Mantiqueira Province and its African connections. Precambrian Research, 136: 203-240.

Smith, H. A., and Barreiro, B., 1990. Monazite U-Pb dating of staurolite grade metamorphism in politic schists. Contributions to Mineral Petrology, vol. 105, p. 602-615

Solar, G.S., Pressley, R.A., Brown, M., Tucker, R.D., 1998. Granite ascent in convergent orogenic belts: testing a model. Geology 26, 711–714.

Spear, F.S., Kohn, M.J. and Cheney, J.T., 1999. P-T paths from anatectic pelites. Contributions to Mineralogy and Petrology 134:17–32.

Sun, S., Dong, Y., He, D., Cheng, C., Liu, X., 2019. Thickening and partial melting of the Northern Qinling Orogen, China: insights from zircon U–Pb geochronology and Hf isotopic composition of migmatites. Journal of the Geological Society, Vol. 176, 1218-1231. https://doi.org/10.1144/jgs2019-030

Tedeschi, M., Novo, T., Pedrosa-Soares, A., Dussin, I., Tassinari, C., Silva, L.C., Gonçalves, L., Alkmim, F., Lana, C., Figueiredo, C., Dantas, E., Medeiros, S., De Campos, C., Corrales, F., Heilbron, M., 2016. The Ediacaran Rio Doce magmatic arc revisited (Araçuaí-Ribeira orogenic system, SE Brazil). J. South Am. Earth Sci. 68, 167–186.

Thompson, A.B., Matile, L., Ulmer, P. 2002. Some Thermal Constraints on Crustal Assimilation during Fractionation of Hydrous, Mantle-derived Magmas with Examples from Central Alpine Batholiths. Journal of Petrology 43, 403-422.

Trompette, R., Egydio-Silva, M., Tommasi, A., Vauchez, A., Uhlein, A., 1993. Amalgamação do gondwana ocidental no panafricano-brasiliano e o papel da geometria do cráton do São Francisco na arquitetura da Faixa Ribeira. Revista Brasileira de Geociências, 23 (3), 187-193.

Trompette, R.R., 1994. Geology of Western Gondwana (2000–500 Ma), Balkena, Rotterdam.

Trompette., R., 1997. Neoproterozoic (~600 Ma) aggregation of Western Gondwana: a tentative scenario. Precambrian Res. 82, 101–112.

Tupinambá, M., Heilbron, M., Valeriano, C., Porto, R., de Dios, F.B., Machado, N., Silva, L.G.D., de Almeida, J.C.H., 2012. Juvenile contribution of the Neoproterozoic Rio Negro Magmatic Arc (Ribeira Belt, Brazil): Implications for Western Gondwana amalgamation. Gondwana Res. 21, 422–438. https://doi.org/10.1016/j.gr.2011.05.012.

Vanderhaeghe, O., and Teyssier, C. (2001) Crustal-scale rheological transitions during late-orogenic collapse. Tectonophysics, 335, 211-228. https://doi.org/10.1016/S0040-1951(01)00053-1

Vanderhaeghe, O., Medvedev, S., Fullsack, P., Beaumont, C., Jamieson, R.A., 2003. Evolution of orogenic wedges and continental plateaux: Insights from crustal thermal–mechanical models overlying subducting mantle lithosphere. Geophys. J. Int. 153, 27–51.

Vanderhaeghe, O., 2009. Migmatites, granites and orogeny: Flow modes of partially-molten rocks and magmas associated with melt/solid segregation in orogenic belts. Tectonophysics, 477, 119-134. https://doi.org/10.1016/j.tecto.2009.06.021

Vanderhaeghe, O. 2012. The thermal–mechanical evolution of crustal orogenic belts at convergent plate boundaries: A reappraisal of the orogenic cycle. Journal of Geodynamics, 56-57, 124-145.

Vauchez, A., Tommasi, A. and Egydio-Silva, M., 1994. Self-indentation of continental lithosphere. Geology, 22, 967–970.

Vauchez, A., Egydio-Silva, M., Babinski, M., Tommasi, A., Uhlein, A., Liu, D., 2007. Deformation of a pervasively molten middle crust: insights from the neoproterozoic Ribeira-Araçuaí orogen (SE Brazil). Terra Nova 19, 278–286.

Vauchez, A., Hollanda, M.H.B.M., Monié, P., Mondou, M., Egydio-Silva, M., 2019. Slow cooling and crystallization of the roots of the Neoproterozoic Araçuaí hot orogen (SE Brazil): Implications for rheology, strain distribution, and deformation analysis. Tectonophysics, 766, 500-518. https://doi.org/10.1016/j.tecto.2019.05.013

Vernon, R.H, and Collins, W.J., 1988. Igneous microstructures in migmatites. Geology, 16, 1126-1129.

Vernon, R.H., 2004. A practical guide to Rock Microstructure. Cambridge University Press, New York. 579 p. ISBN 0 521 81443 X – ISBN 0 521 89133 7

Vernon, R.H., 2011, Microstructures of melt-bearing regional metamorphic rocks, in van Reenen, D.D., Kramers, J.D., McCourt, S., and Perchuk, L.L., eds., Origin and Evolution of Precambrian High-Grade Gneiss Terranes, with Special Emphasis on the Limpopo Complex of Southern Africa: Geological Society of America Memoir 207, p. 1–11, doi:10.1130/2011.1207(01).

Waters, D. J. 2001. The significance of prograde and retrograde quartz-bearing intergrowth microstructures in partially melted granulite-facies rocks. Lithos, 56, 97-110.

Whalen, J.B., Currie, K.L., Chappel, B.W., 1987. A-type granites: geochemical characteristics, discrimination and petrogenesis. Contributions to Mineralogy and Petrology, 95, 407-419.

White, A., J., R. and Chapell, B.W., 1977. Ultrametamorphism and granitoid genesis. Tectonophysics, 43, 7-22.

Whitney, D. L. And Evans, B. W., 2010. Abbreviations for names of rock-forming minerals. American Mineralogist, 95, 185-187.

Wilson, M., 1989. Igneous Petrogenesis. London: Unwin Hyman, 466p.

Wing, B. A., Ferry, J. M., Harrison, T. M., 2003. Prograde destruction and formation of monazite and allanite during contact and regional metamorphism of pelites: petrology and geochronology. Contributions to Mineral Petrology, vol. 145, p. 228-250.

Wolfram, L.C., Weinberg, R.F., Hasalová, P., and Becchio, R., 2017. How Melt Segregation Affects Granite Chemistry: Migmatites from the Sierra de Quilmes, NW Argentina. Journal of Petrology, 58, No.12, 2339-2364.

Yakymchuk, C., Kirkland, C. L., Clark, C., 2018. Th/U ratios in metamorphic zircon. Journal of Metamorphic Geology, 36, 715-737. DOI: 10.1111/jmg.12307

Yakymchuk, C., 2021. Migmatites. In: Alderton, David; Elias, Scott A. (eds.) Encyclopedia of Geology, 2nd edition. vol. 2, pp. 492-501. United Kingdom: Academic Press. dx.doi.org/10.1016/B978-0-08-102908-4.00021-7

Zhao, K.; Xu, X.; Erdmann, S. 2017. Crystallization conditions of peraluminous charnockites: constraints from mineral thermometry and thermodynamic modelling. Contrib. Mineral. Petrol. 172, 26.

Figure 1

Click here to access/download;Figure;Figure 1-Geological map Mantiqueira Province.jpg

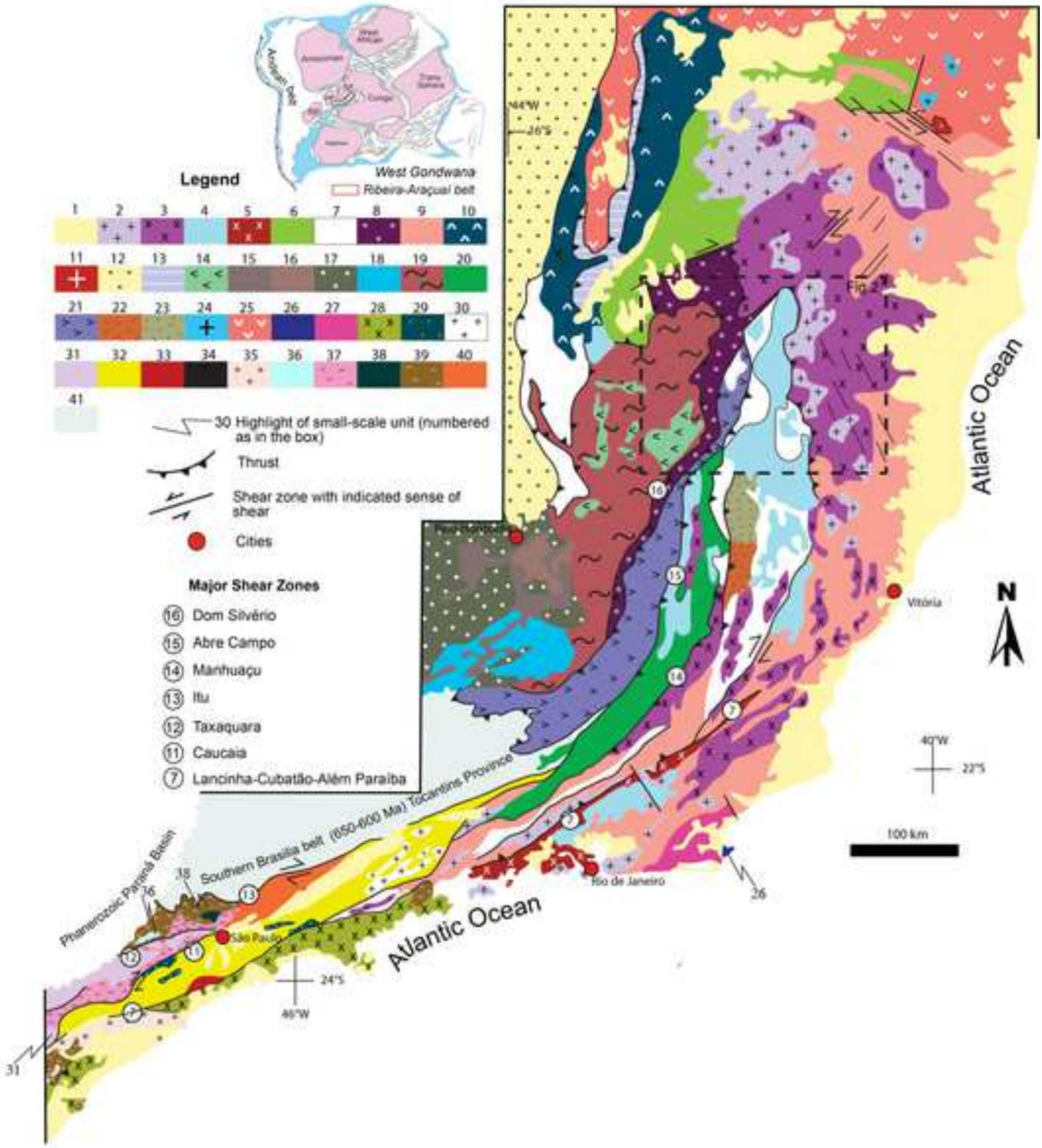

Figure 2

Click here to access/download;Figure;Figure 2 - Geological setting .jpg

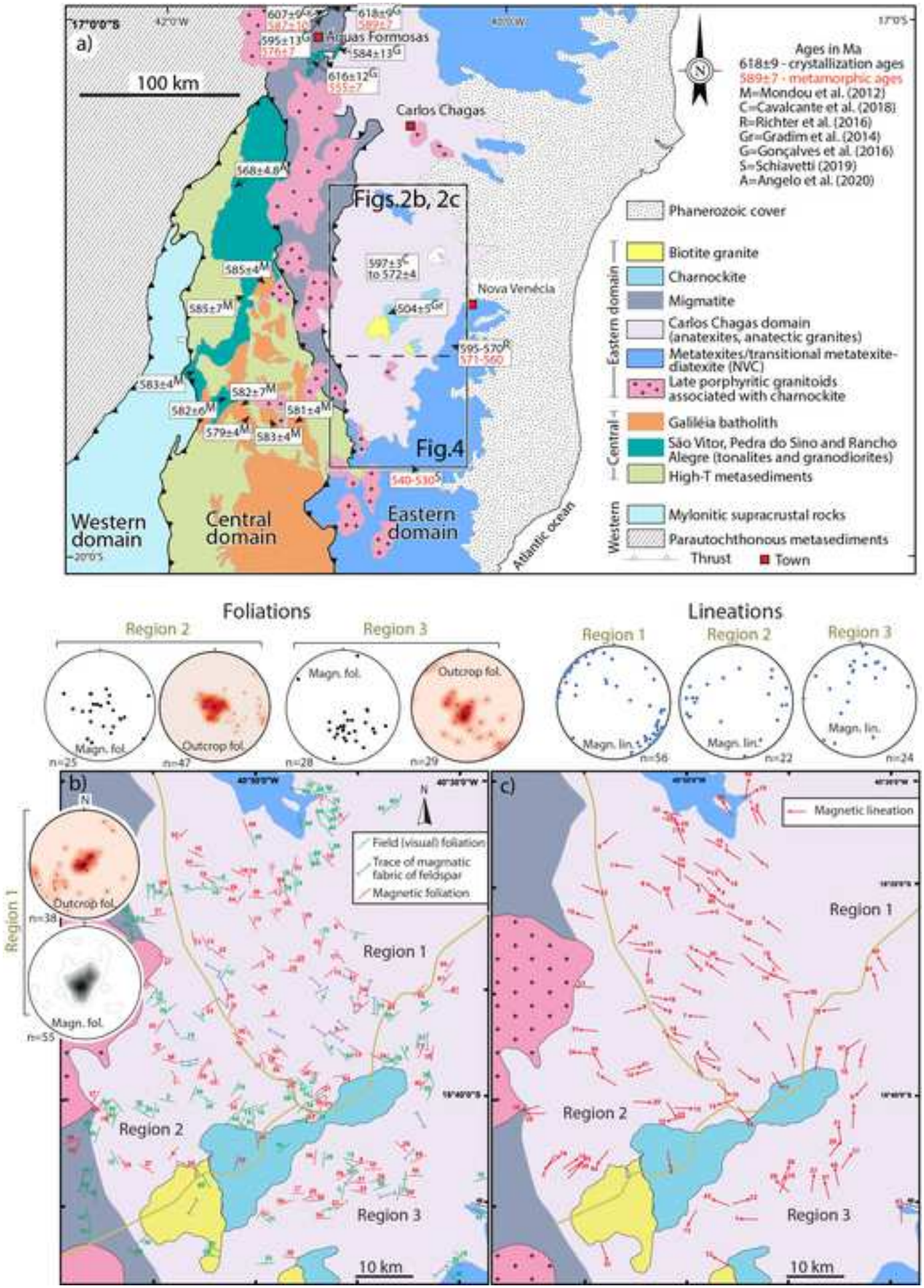

Figure 3

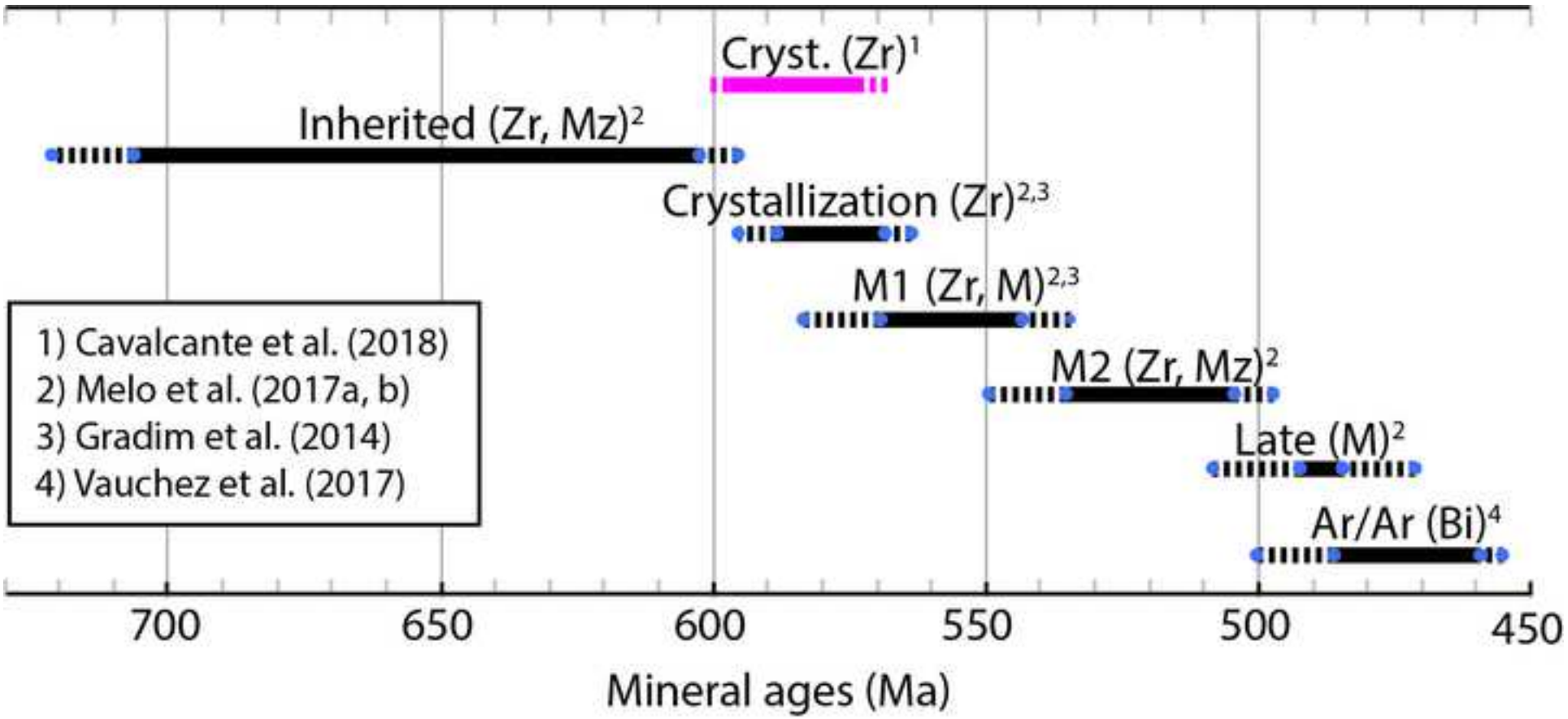

Figure 4

Click here to access/download;Figure;Figure 4-Carlos chagas classification migmatite.jpg

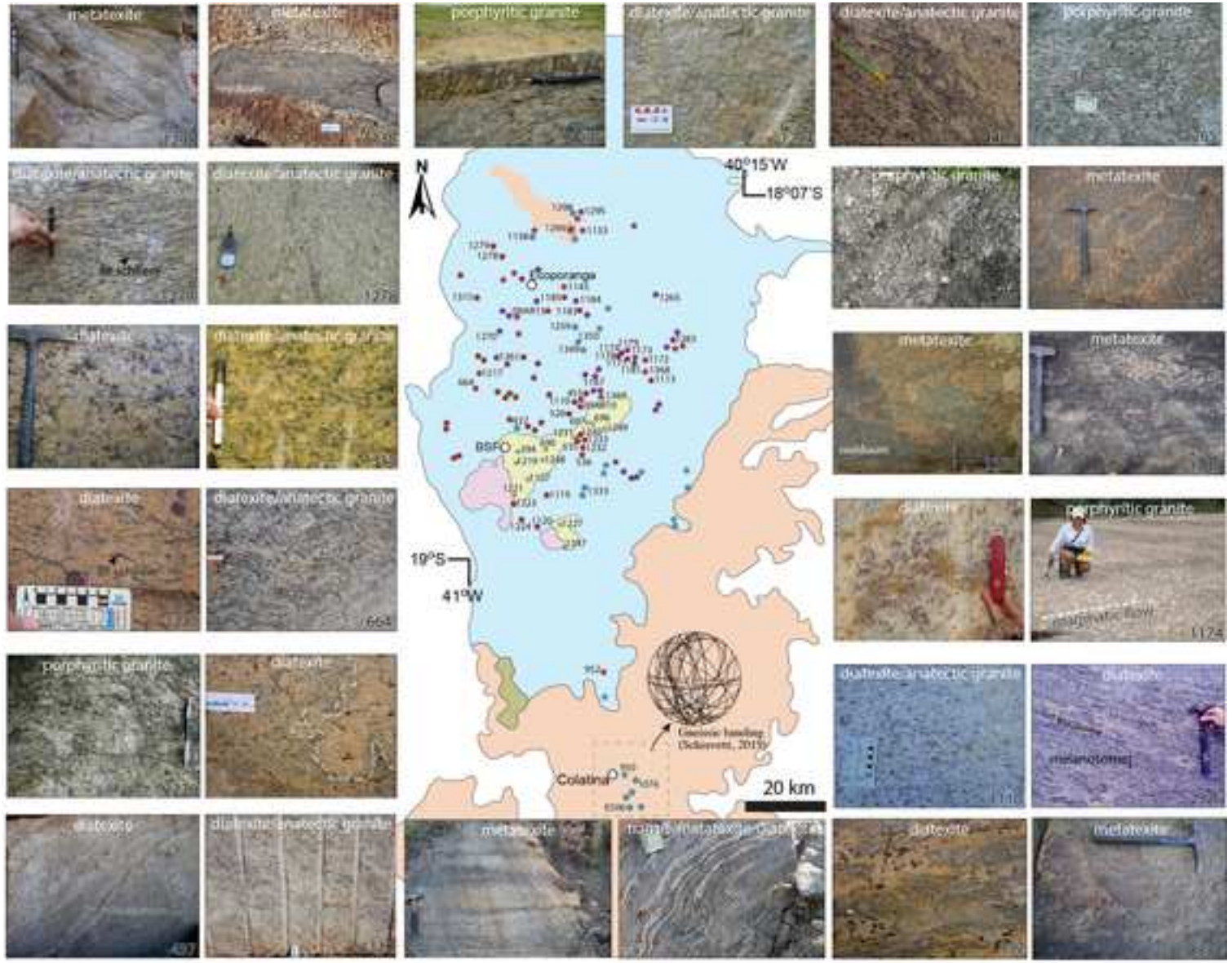

Figure 5

Click here to access/download;Figure;Figure 5-Figure field aspects.jpg

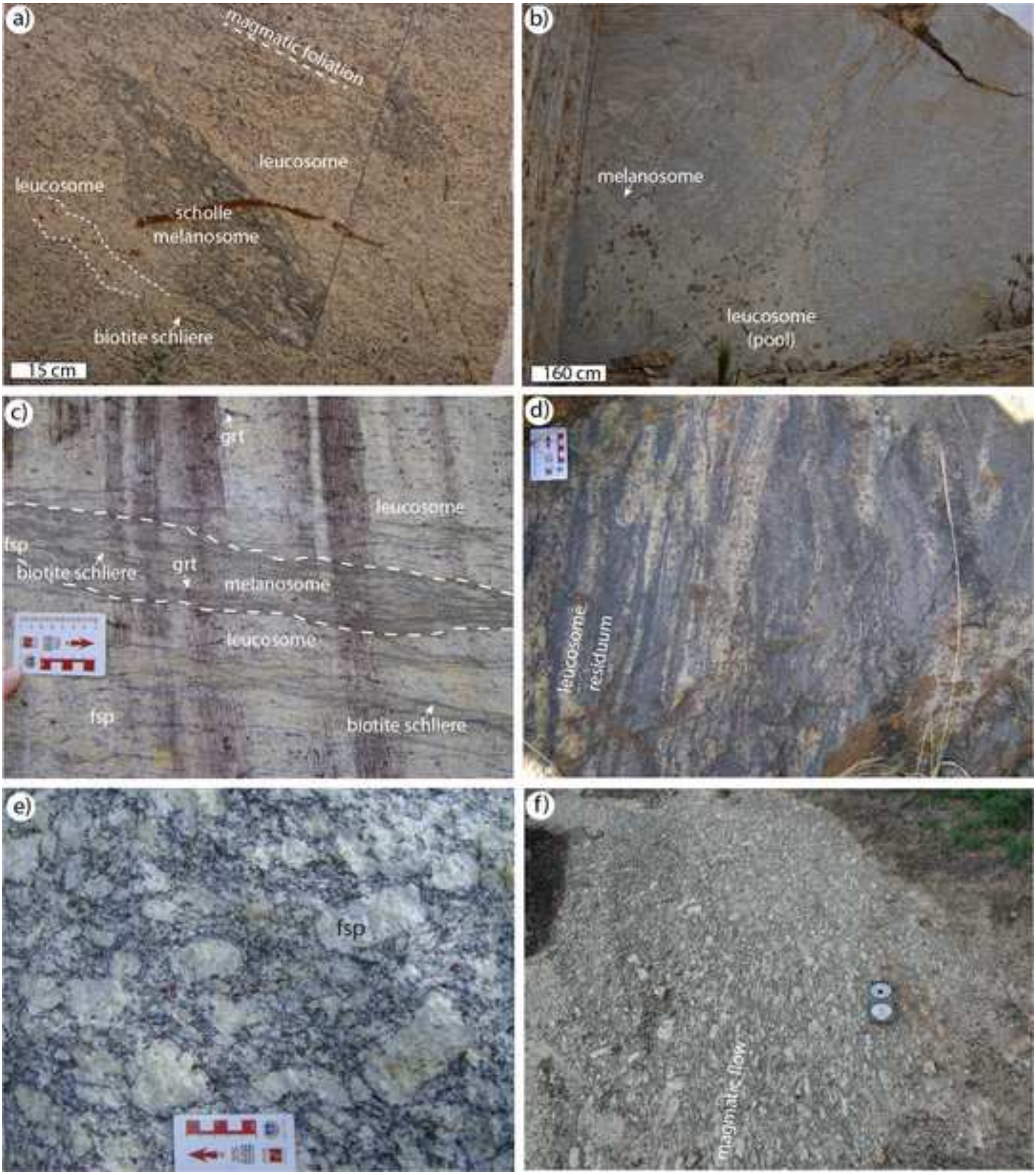

Figure 6

Click here to access/download;Figure;Figure 6-Field aspects kinzigite, granulites, charno.jpg

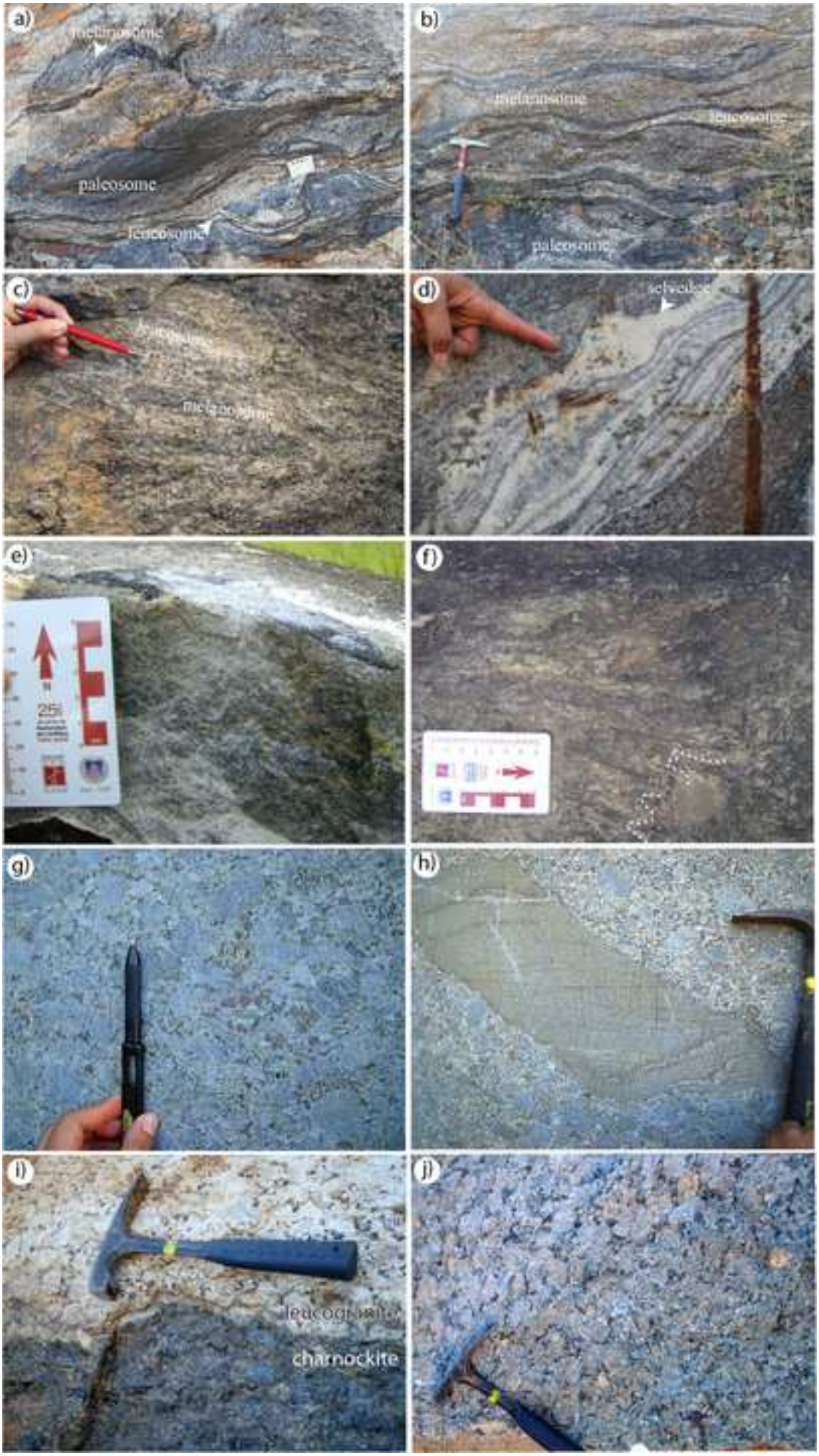

Figure 7

Click here to access/download;Figure;Figure 7-Mapa micro CC.jpg

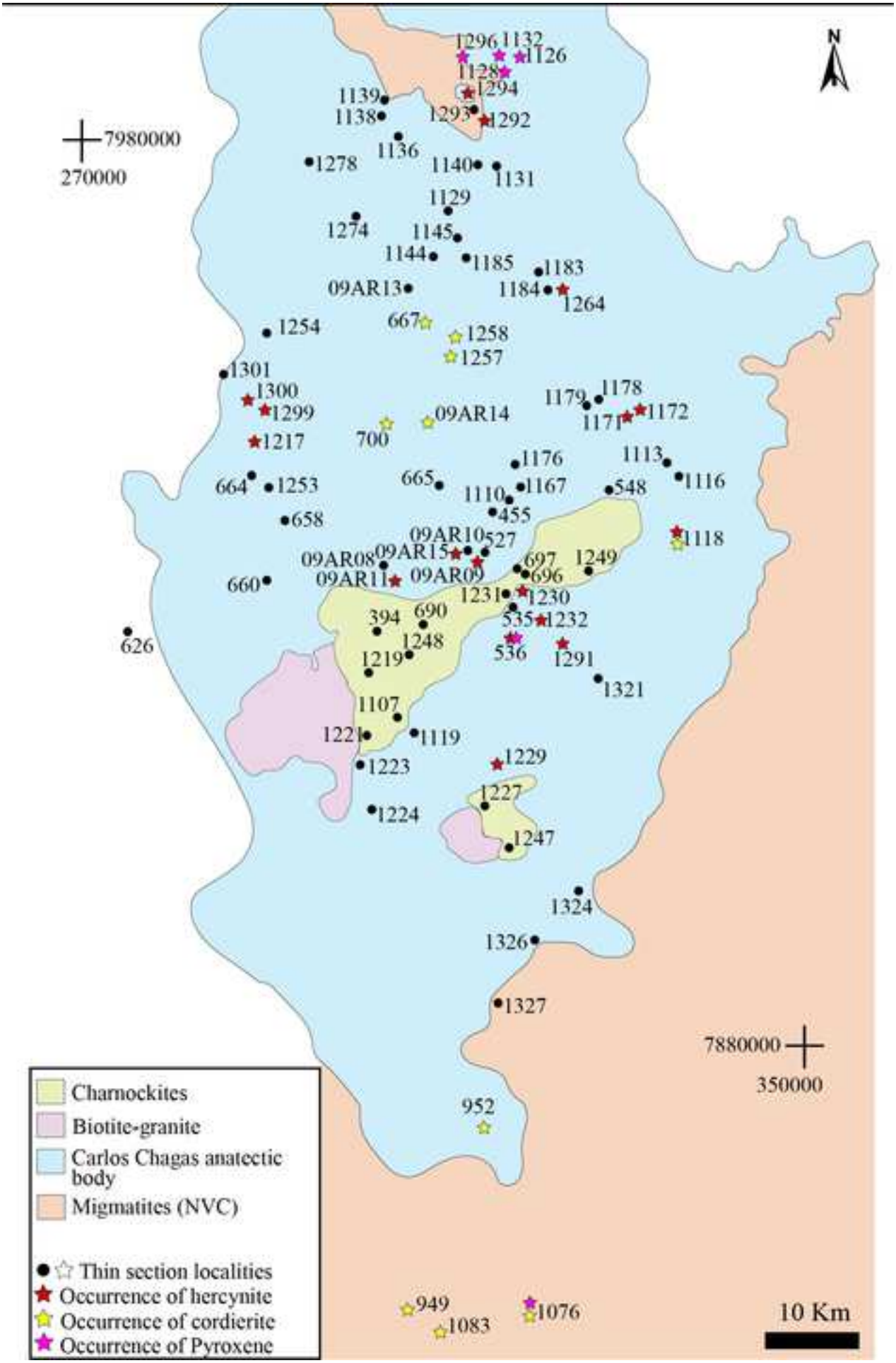

Figure 8

Click here to access/download;Figure;Figure 8- microscale aspects CC.jpg

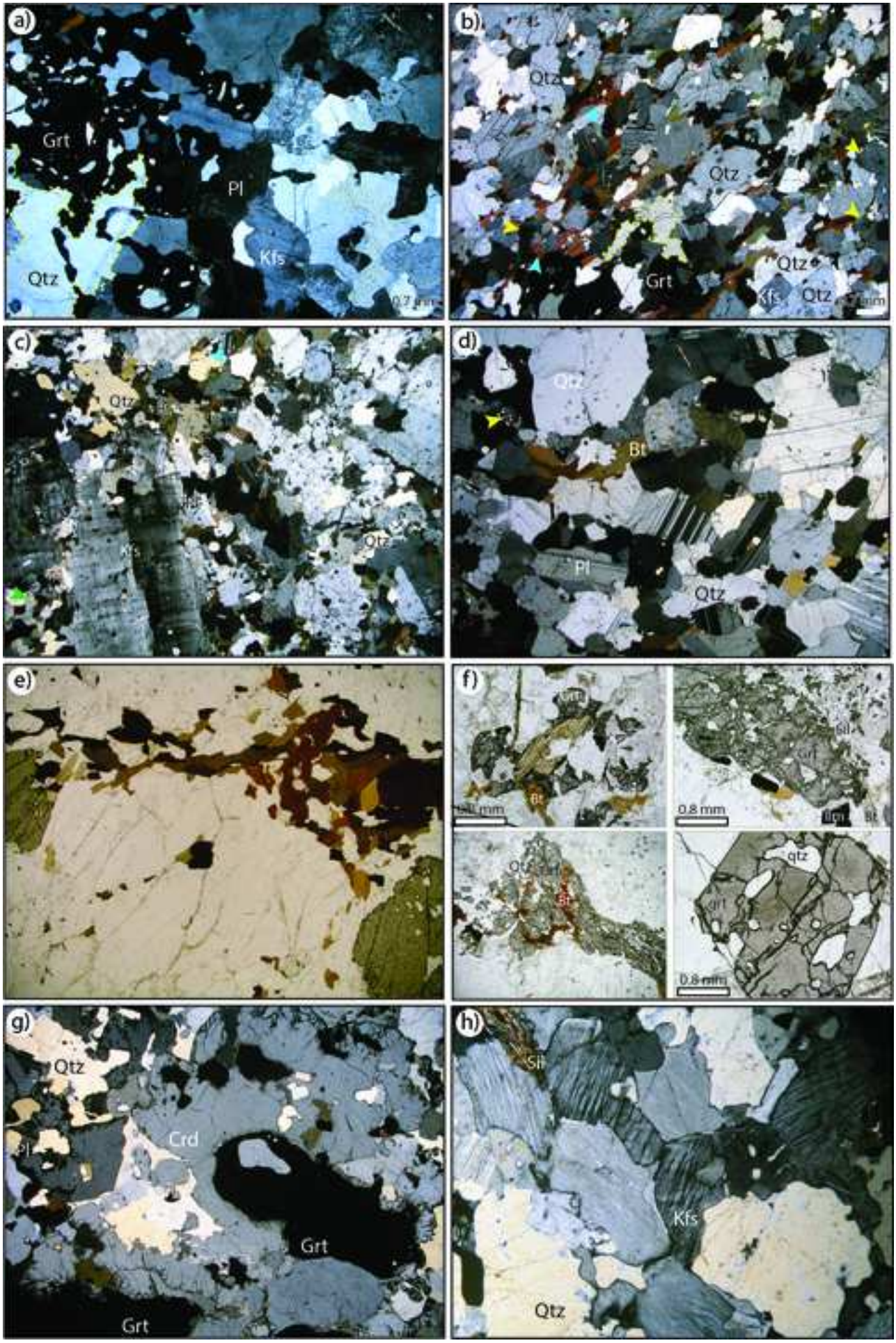

Figure 9

Click here to access/download;Figure;Figure 9-micro aspects migmatitic granulites and kinzigites.jpg

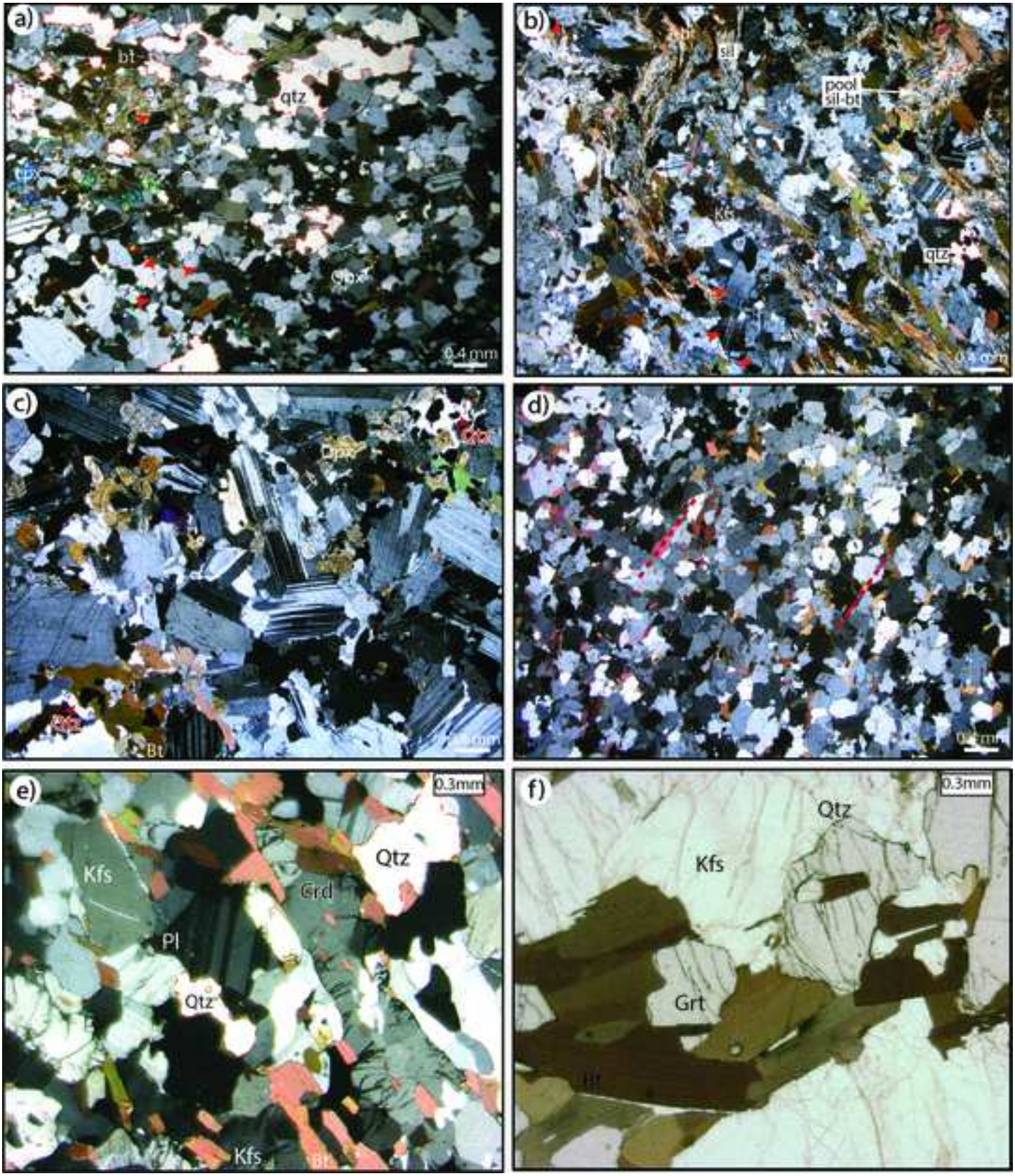

Figure 10

Click here to access/download;Figure;Figure 10 - microscopic aspects charnockite.jpg

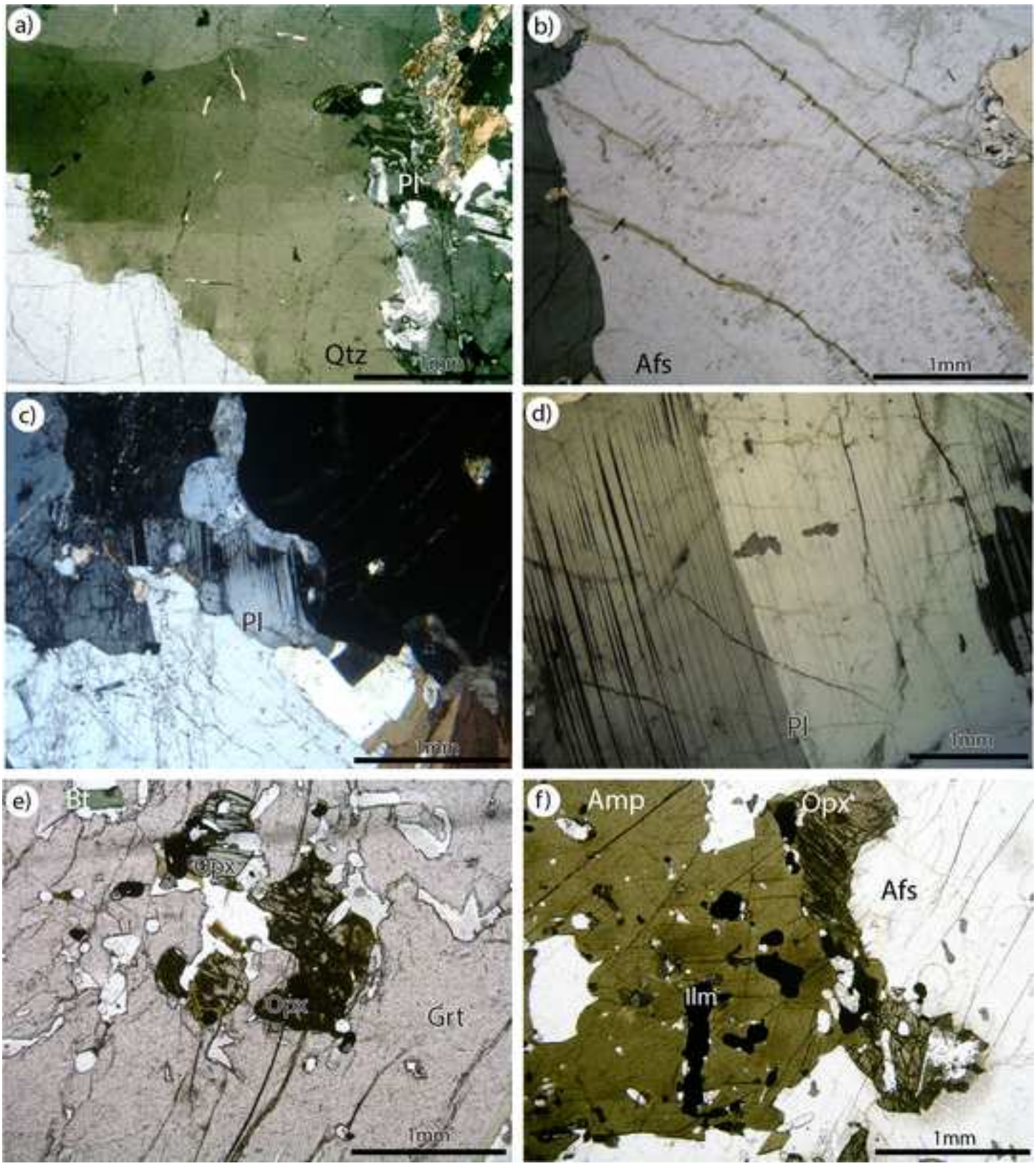

Figure 11

Click here to access/download;Figure;Figure 11.jpg

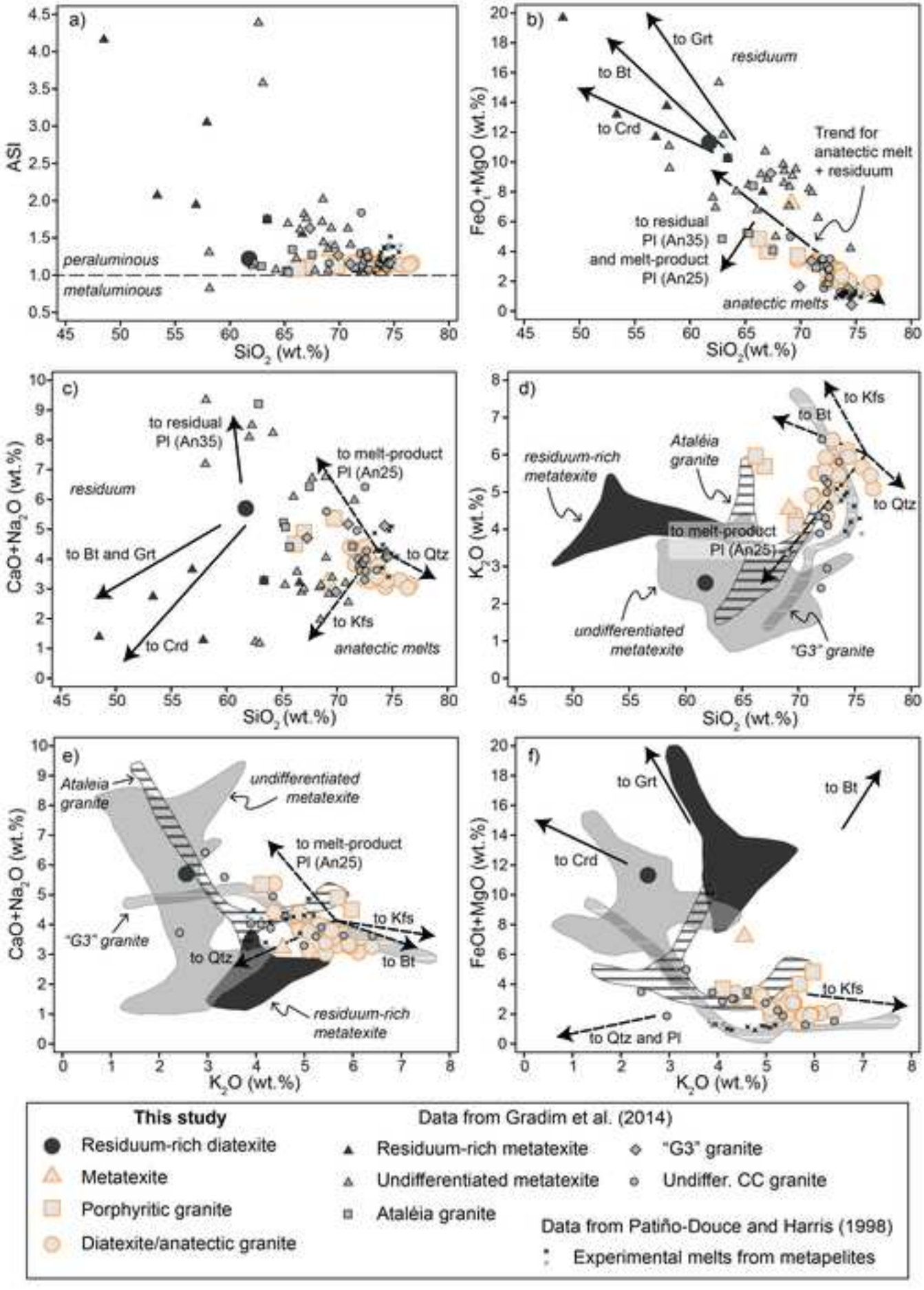

Figure 12

Click here to access/download;Figure;Figure 12.jpg

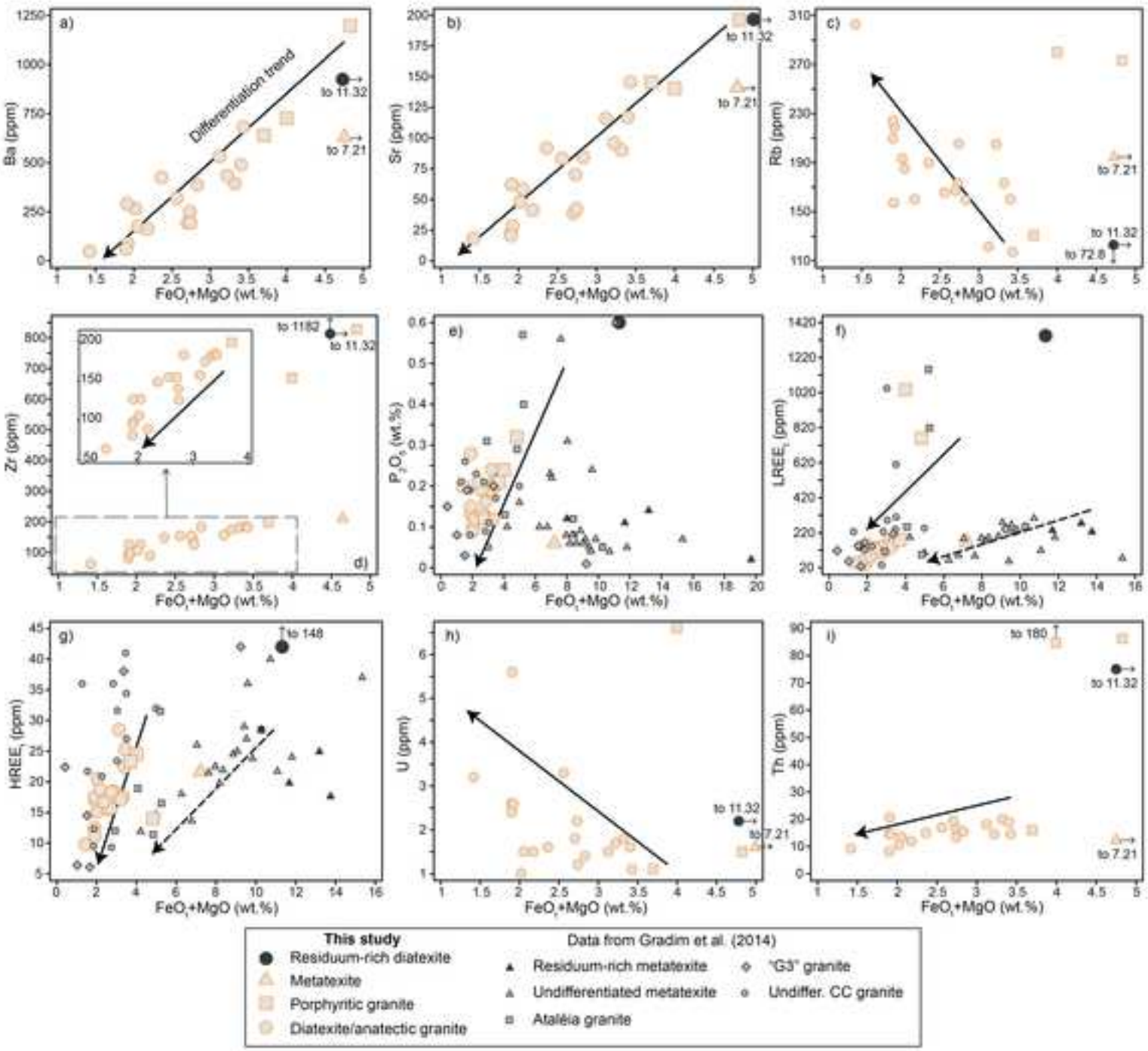

Figure 13

Click here to access/download;Figure;Figure 13.jpg

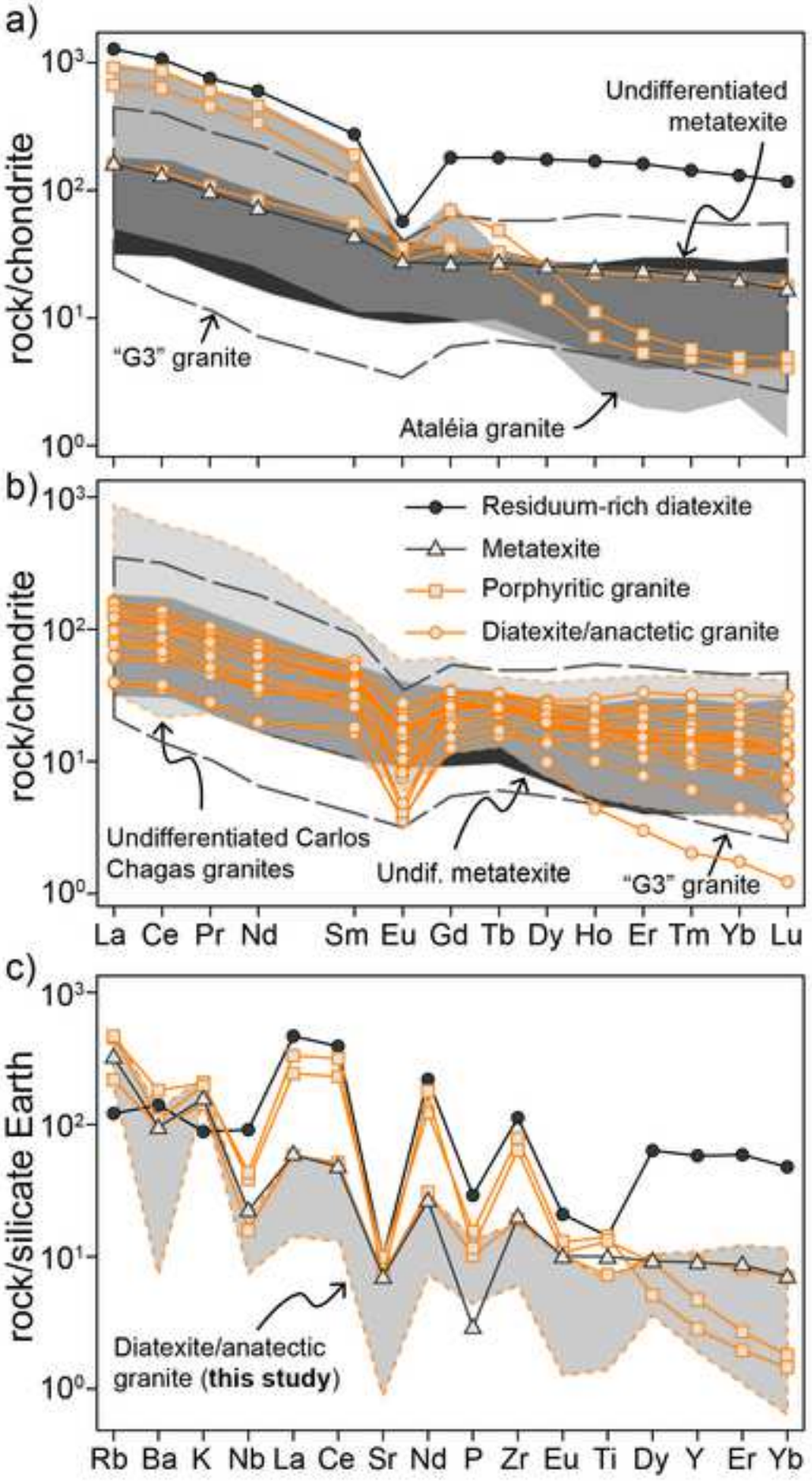

Figure 14

Click here to access/download;Figure;Figure 14.jpg

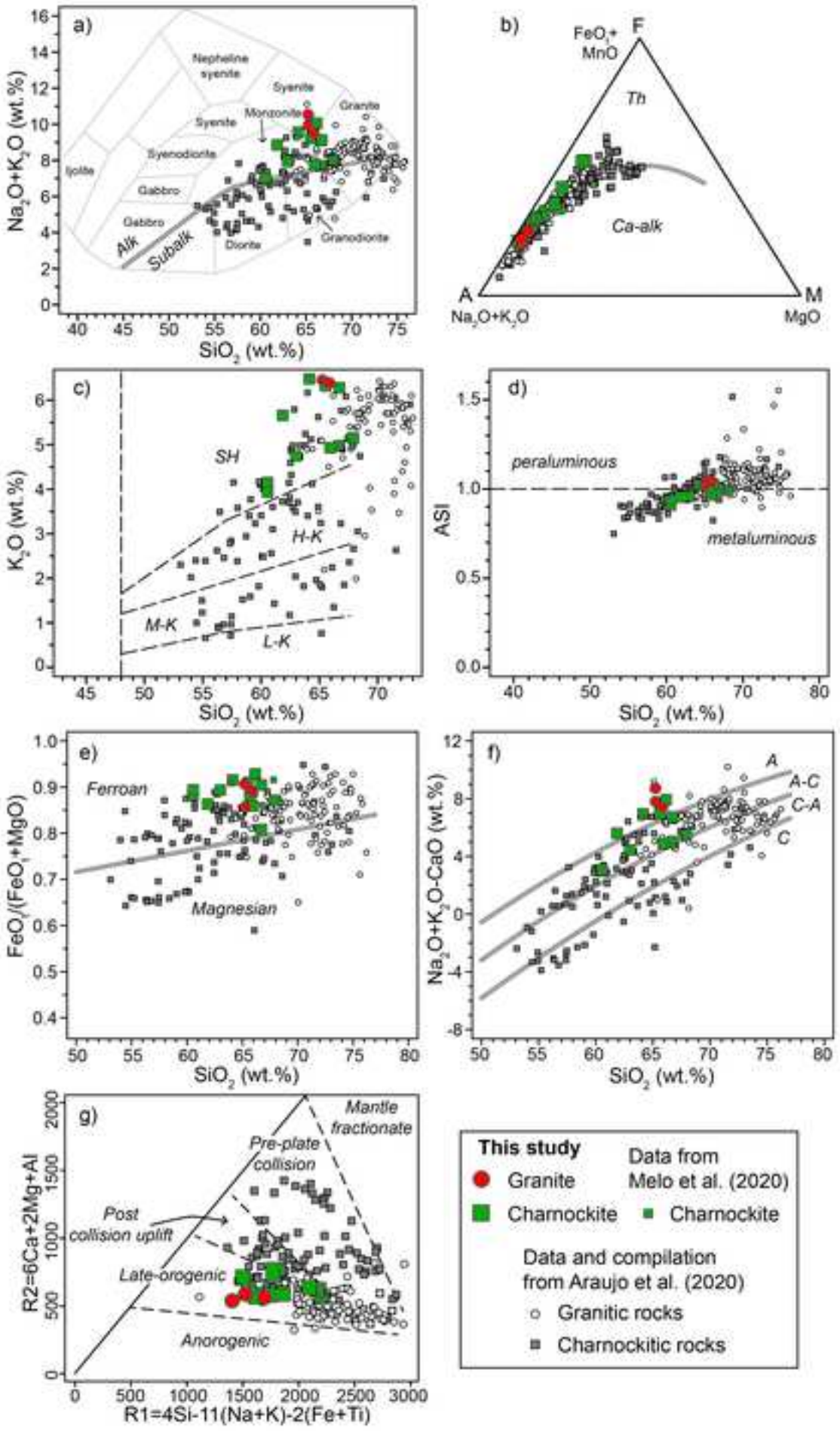

Figure 15

Click here to access/download;Figure;Figure 15.jpg

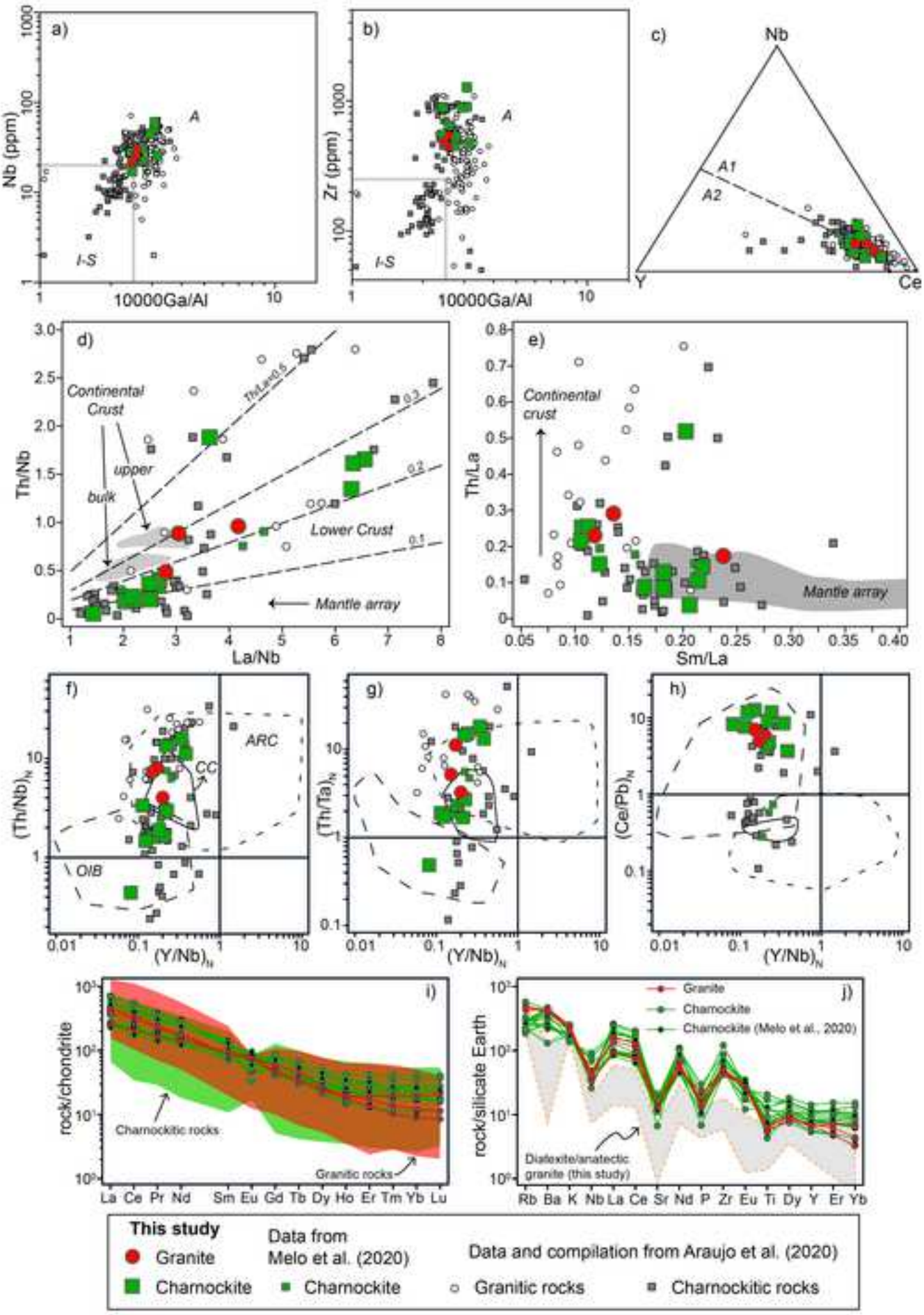

Figure 16

Click here to access/download;Figure;Figure 16, a, b, c.jpg